Title

Measurements of the fast ion distribution in the Large Helical Device

ISBN

9798265471437

Author

Hayashi, Wataru

Publication Date

2025-12-06

Peer reviewed|Thesis/dissertation

UNIVERSITY OF CALIFORNIA,
IRVINE

Measurements of the fast ion distribution in the Large Helical Device

DISSERTATION

submitted in partial satisfaction of the requirements
for the degree of

DOCTOR OF PHILOSOPHY

in Physics

by

Wataru H. J. Hayashi

Dissertation Committee:
Professor Bill Heidbrink, Chair
Professor Zhihong Lin
Assistant Professor Laszlo Bardoczi

2025

DEDICATION

To my mother Dr. Saeko Suzuki Hayashi, my father Dr. Masahiko Hayashi, and my brother Takeru Hayashi, as well as to all those who helped raise me in rainy Hilo town.

Every generation has the obligation to free men's minds for a look at new worlds...to look out from a higher plateau than the last generation. Your vision is not limited by what your eye can see, but by what your mind can imagine. Many things that you take for granted were considered unrealistic dreams by previous generations. If you accept these past accomplishments as commonplace then think of the new horizons that you can explore. From your vantage point, your education and imagination will carry you to places which we won't believe possible. Make your life count and the world will be a better place because you tried.

- Ellison S. Onizuka

TABLE OF CONTENTS

Page

LIST OF FIGURES **v**

LIST OF TABLES **vii**

ACKNOWLEDGMENTS **viii**

VITA **x**

ABSTRACT OF THE DISSERTATION **xiii**

1 Introduction **1**
- 1.1 Fusion plasmas . . . 1
- 1.2 Stellarator . . . 3
- 1.3 Large Helical Device . . . 5
- 1.4 Fast ions . . . 7
- 1.5 Fast ion diagnostics . . . 8
- 1.6 Alfvén eigenmodes . . . 9
- 1.7 Thesis overview . . . 11

2 Fast-ion charge-exchange spectroscopy **12**
- 2.1 Diagnostic concept . . . 12
- 2.2 Cold Dα filter methods . . . 15
- 2.3 LHD hardware . . . 18
- 2.4 Data processing . . . 19

3 Forward modeling with FIDASIM **21**
- 3.1 Simulation method . . . 21
- 3.2 Feature implementation . . . 22
  - 3.2.1 Adaptive grid cells . . . 22
  - 3.2.2 COCOS coordinate system . . . 23
  - 3.2.3 VMEC input support . . . 25
- 3.3 Full 5-D neoclassical distribution . . . 28
- 3.4 Reduced model distribution . . . 29

4 Measurements near the injected neutral energy **34**
4.1 New sightline concept . . . 35
4.2 Measured data and simulation results . . . 37

5 Quiet LHD plasmas **41**
5.1 Selection process . . . 42
5.1.1 Plasma profiles and heating beam configurations . . . 43
5.1.2 Quantitative selection of MHD-quiescent discharges . . . 44
5.1.3 Shared radial coordinate for FICXS and VNC . . . 46
5.1.4 Considerations for 7-O LOS collecting volume . . . 49
5.1.5 Normalization of Goldston distribution . . . 51
5.1.6 Variation in Doppler broadening of beam emission feature . . . 53
5.2 Experimental results . . . 58
5.2.1 Parametric study of FICXS measurements . . . 58
5.2.2 Measurements compared to reduced model FIDASIM . . . 63
5.3 Extended simulation results . . . 68
5.3.1 Pressure-induced axis shift . . . 68
5.3.2 Orbit simulations . . . 71

6 LHD plasmas with instabilities **73**
6.1 High-field cases . . . 74
6.2 Low-field case . . . 87

7 Conclusion and future work **98**
7.1 Summary . . . 98
7.2 Future work . . . 101

Bibliography **103**

Appendix A Adaptive grid cells **112**

Appendix B COCOS coordinate system **117**

Appendix C VMEC input support **124**

Appendix D Goldston distribution **131**

Appendix E Data for MHD-quiescent study **145**

LIST OF FIGURES

Page

1.1 Fusion cross sections 2
1.2 Cyclotron orbit of an ion following a field line 3
1.3 Top-down midplane view of LHD and boundary surface 6

2.1 Diagram of fast ion charge exchange process 13
2.2 Background-subtracted FICXS spectrum 14
2.3 Diagram of prototype spectrometer in Zemax 15
2.4 Image of prototype spectrometer on optical bench 16
2.5 Wavelength calibration for the prototype spectrometer 16
2.6 Measured spectrum of labsphere, Dα lamp, and neon lamp for both channels 17
2.7 Full-width half-maximum calculated for the notch produced by the ultra-narrow bandpass filter. 17

3.1 Interpolation of VMEC onto R-Z plane 26
3.2 Flowchart for FIDASIM using a GNET distribution 28
3.3 Flowchart for FIDASIM using a Goldston distribution 32
3.4 GNET and Goldston distributions and fast ion densities 33

4.1 Time traces for discharge 172359 35
4.2 GNET distribution function and weight functions for discharge 172359 . . . 36
4.3 Comparison of measured FIDA density between old LOS and new LOS. . . . 38
4.4 Parametric dependency of new LOS 39

5.1 Typical profiles for three configurations vs normalized minor radius 43
5.2 Rotational transform and effective helical ripple vs R_{ax} 44
5.3 Selection process for MHD-quiescent samples 45
5.4 Flux surfaces for $\rho = 0.5$ and $\rho = 1.0$ calculated by VMEC 47
5.5 Radial and vertical displacement of the magnetic axis vs toroidal angle over one field period calculated by VMEC 48
5.6 Parameters along FICXS sightlines 49
5.7 Variation in parameters along FICXS sightlines 51
5.8 Measured vs simulated global neutron emission rates for three configurations 52
5.9 Weight functions calculated by FIDASIM for three configurations 52
5.10 Weight function for global neutron emission 53
5.11 Mid plane view of NB3 injection geometries 54

5.12 FIDA density vs NB3 ports . . . 55
5.13 Mid plane view of NB3 ports and 7-O LOS . . . 56
5.14 FIDA profile and BES broadening vs NB3 ports . . . 57
5.15 Low-energy FIDA density vs fitted parameters . . . 59
5.16 High-energy FIDA density vs fitted parameters . . . 60
5.17 FIDA density measurements vs FIDASIM for three configurations . . . 64
5.18 Relative comparison of measured VNC vs FIDASIM for three configurations 65
5.19 Experiment/theory ratio vs R_{ax} . . . 66
5.20 Experiment/theory ratio for VNC vs R_{ax} . . . 67
5.21 Field contours at the $\sqrt{\psi/\psi_{edge}} = 0.5$ surface for three configurations . . . 68
5.22 Normalized field strength along field lines . . . 69
5.23 Fourier components of magnetic field strength for three R_{ax} configurations . 70
5.24 Field-period-averaged R_{ax} calculated by VMEC compared to the vacuum configuration . . . 70
5.25 Orbits calculated by DELTA5D for three configurations and three initial pitch values . . . 71
5.26 Loss fraction vs time of passing fast ions with initial energy 50 keV for three configurations calculated by SIMSOPT . . . 72

6.1 Power spectral densities for high-field cases . . . 74
6.2 Time traces for high-field cases . . . 75
6.3 Calculation of toroidal mode numbers from measured fluctuations . . . 75
6.4 Calculated mode numbers and Alfvén continuum calculations for high-field cases . . . 77
6.5 Alfvén continuum calculations by STELLGAP and AE3D for high-field cases 78
6.6 Radial eigenfunctions calculated by AE3D for high-field cases . . . 79
6.7 Plasma profiles for high-field cases . . . 80
6.8 Thermal ion profiles for high-field cases . . . 80
6.9 Rotational transform and effective helicity for the high-field cases . . . 81
6.10 Fast ion measurements for high-field cases . . . 82
6.11 Experiment/theory ratios for high-field cases . . . 83
6.12 High-field case measurements compared to quiescent cases . . . 85
6.13 High-field case plasma profiles compared to quiescent profiles . . . 86
6.14 Power spectral density for the low-field case . . . 87
6.15 Time traces for the low-field case . . . 88
6.16 Calculated mode numbers and Alfvén continuum calculations for the low-field case . . . 89
6.17 Alfvén continuum calculations by STELLGAP and AE3D for the low-field case 89
6.18 Radial eigenfunctions calculated by AE3D for the low-field case . . . 90
6.19 Plasma profiles for the low-field case . . . 91
6.20 Thermal ion profiles for the low-field case . . . 91
6.21 Rotational transform and effective helicity for the low-field case . . . 92
6.22 Measured and calculated fast ion profiles for the low-field case . . . 93
6.23 Low-field case measurements compared to quiescent cases . . . 95
6.24 Low-field case plasma profiles compared to quiescent profiles . . . 96

LIST OF TABLES

Page

1.1 Device specifications for LHD 5

2.1 FICXS sightline configurations used on LHD 18

3.1 All COCOS values with identifiers 25

5.1 Comparison of flux coordinates for TSMAP and VMEC 48
5.2 Log-linear fitting coefficients for low-energy FIDA density 60
5.3 Log-linear fitting coefficients for high-energy FIDA density 61
5.4 Number of data points used in calculating values for figures 66

ACKNOWLEDGMENTS

I would like to thank my thesis advisor Bill Heidbrink first and foremost for fruitful discussions in all manner of physics and beyond. The quality of his advisement is reflected in his former students and post docs who did not hesitate to answer my questions and offer guidance.

I would like to thank my peers in grad school. Garrett who shared in the struggles of being a graduate student and experimental physicist. Our discussions often provided the assurance I needed to move forward. Cannon for our discussions on physics, coffee, and books that I promise I'll eventually read.

I would like to thank all my collaborators who, through all their years of experience, made me a better scientist. The team at the Large Helical Device for providing their expertise on running experiments as well as their expertise on local restaurants in Toki. Elizabeth Paul and members of the Paul group for their advice and expertise on stellarator theory.

I would like to thank the first cohort of the Fusion Student Delegation. The work we accomplished continues to give me hope in the face of uncertainty as well as the motivation to encourage future cohorts to continue in our foot steps.

I could never have done this without the support of my family as well as the support of my partner Shan and all our close friends. I am forever grateful to all those that I have met and shared meals, coffees, and conversations with in my time as a graduate student.

The text of Chapter 4 and a portion of Chapter 7 of this dissertation is a reprint of the material as it appears in Hayashi, W.H.J., Heidbrink, W.W., Muscatello, C.M., Lin, D.J., Osakabe, M., Ogawa, K., Kawamoto, Y., Yamaguchi, H., Seki, R., Nuga, H., Isobe, M., Fujiwara, Y., & Kamio, S. (2024). Charge-exchange measurements of high-energy fast ions in LHD using negative-ion neutral beam injection. *Journal of Instrumentation, 19*(12),

P12006, used with permission from IOP Publishing Ltd and Sissa Medialab. The coauthors listed in this publication are William W. Heidbrink, Chris M. Muscatello, Daniel J. Lin, Masaki Osakabe, Kunihiro Ogawa, Yasuko Kawamoto, Hiroyuki Yamaguchi, Ryohsuke Seki, Hideo Nuga, Mitsutaka Isobe, Yutaka Fujiwara, and Shuji Kamio.

The work presented in this thesis was supported by U.S. DOE Grants DE-SC0018255 and DE-SC0022131, NINS program of Promoting Research by Networking among Institutions Grant No. 01411702, NIFS International Collaboration Research Programs Grant Nos. NIFS18/KLPR047, NIFS07/KLPH004, and UFEX105, and the LHD project budget Nos. ULRR006, ULRR035, ULRR036, and ULRR702.

VITA

Wataru H. J. Hayashi

EDUCATION

Doctor of Philosophy in Physics **2025**
University of California, Irvine *Irvine, California*

Master of Science in Physics **2025**
University of California, Irvine *Irvine, California*

Bachelor of Science in Physics **2020**
University of Nevada, Reno *Reno, Nevada*

RESEARCH EXPERIENCE

Graduate Student Researcher **2020–2025**
University of California, Irvine *Irvine, California*

Undergraduate Student Researcher **2019–2020**
University of Nevada, Reno *Reno, Nevada*

TEACHING EXPERIENCE

Graduate Teaching Assistant **2020–2020**
University of California, Irvine *Irvine, California*

PUBLICATIONS

Alfvèn eigenmode interactions with energetic particles measured with fast ion charge exchange spectroscopy in the Large Helical Device **2026**
W.H.J. Hayashi
(Planned)

Active measurements of fast-ion confinement in quiescent plasmas in the Large Helical Device **2026**
W.H.J. Hayashi, W.W. Heidbrink, G. Prechel, M. Osakabe, Y. Kawamoto, K. Ogawa, M. Isobe, H. Yamaguchi, H. Nuga, R. Seki, S. Kamio, Y. Fujiwara, E.J. Paul, and A. Chambliss
Nuclear Fusion (Planned)

Energetic particle transport under the effects of the radial electric field in LHD **2025**

E. Green, W.H.J. Hayashi, W.W. Heidbrink, Z. Lin, H. Yamaguchi

Nuclear Fusion (Submitted)

Charge-exchange measurements of high-energy fast ions in LHD using negative-ion neutral beam injection **2024**

W.H.J. Hayashi, W.W. Heidbrink, C.M. Muscatello, D.J. Lin, M. Osakabe, K. Ogawa, Y. Kawamoto, H. Yamaguchi, R. Seki, H. Nuga, M. Isobe, Y. Fujiwara, S. Kamio

Journal of Instrumentation

Influence of sawtooth oscillations on fast ions in a stellarator **2024**

D. Moseev, M. Zanini, H. Kasahara, H.P. Laqua, H. Funaba, W.H.J. Hayashi, W.W. Heidbrink, K. Ida, H. Igami, Y. Kawamoto, N. Kenmochi, S.A. Lazerson, M. Nishiura, R. Ochoukov, K. Ogawa, M. Rud, M. Salewski, T. Seki, N. Tamura, K. Tanaka, T. Tokuzawa, M. Yoshinuma

Nuclear Fusion

PRESENTATIONS

Charge-exchange measurements of fast ions in quiescent and MHD-active plasmas in the Large Helical Device **2025**

W.H.J. Hayashi, W.W. Heidbrink, G. Prechel, M. Osakabe, Y. Kawamoto, K. Ogawa, M. Isobe, H. Yamaguchi, H. Nuga, R. Seki, S. Kamio, Y. Fujiwara, E.J. Paul, and A. Chambliss

67th Annual Meeting of the APS Division of Plasma Physics – poster

Empirical study of Alfven eigenmodes and fast ions on the Large Helical Device **2025**

W.H.J. Hayashi, W.W. Heidbrink, M. Osakabe, K. Ogawa, H. Yamaguchi, R. Seki, H. Nuga, M. Isobe, Y. Kawamoto, Y. Fujiwara, S. Kamio

18th Technical Meeting on Energetic Particles in Magnetic Confinement Systems – poster

Study of magnetic axis effect on fast-ion confinement using FICXS and neutron camera profile measurements in the Large Helical Device **2024**

W.H.J. Hayashi, W.W. Heidbrink, M. Osakabe, Y. Kawamoto, K. Ogawa, M. Isobe, H. Nuga, R. Seki, H. Yamaguchi

66th Annual Meeting of the APS Division of Plasma Physics – poster

Measurements of shifted magnetic axis effect on fast-ion confinement in the Large Helical Device **2024**
W.H.J. Hayashi, W.W. Heidbrink, M. Osakabe, Y. Kawamoto, K. Ogawa, M. Isobe, H. Nuga, R. Seki, H. Yamaguchi
24th International Stellarator Heliotron Workshop – poster

FIDA and other observations of improved fast-ion confinement in the Large Helical Device using shifted magnetic configurations **2023**
W.H.J. Hayashi, W.W. Heidbrink, M. Osakabe, Y. Kawamoto, K. Ogawa, M. Isobe, H. Nuga, R. Seki, H. Yamaguchi, T. Oishi
65th Annual Meeting of the APS Division of Plasma Physics – poster

Detection of high-energy fast ions in LHD and prospects for quantitative validation of neoclassical fast-ion transport calculations **2023**
W.H.J. Hayashi, W.W. Heidbrink, C.M. Muscatello, Z. Lin, M. Osakabe, K. Ogawa, Y. Kawamoto, M. Isobe, Y. Fujiwara, H. Yamaguchi, M. Nishiura, J.H. Nicolau, E.M. Green
29th IAEA Fusion Energy Conference – poster

Comparison of synthetic diagnostic code FIDASIM with fast-ion D-alpha emissions on the Large Helical Device using notched beam modulation **2022**
W.H.J. Hayashi, W.W. Heidbrink, Z. Lin, J.H. Nicolau, C.M. Muscatello, M. Nishiura, Y. Kawamoto, K. Ogawa, T. Oishi, R. Seki, H. Nuga, H. Yamaguchi, M. Osakabe
64th Annual Meeting of the APS Division of Plasma Physics – poster

Successful FIDA diagnosis of fast ions from negative-ion neutral beams near their injection energy **2021**
W.H.J. Hayashi, W.W. Heidbrink, D.J. Lin, C.M. Muscatello, Y. Fujiwara, H. Yamaguchi
63rd Annual Meeting of the APS Division of Plasma Physics – poster

ABSTRACT OF THE DISSERTATION

Measurements of the fast ion distribution in the Large Helical Device

By

Wataru H. J. Hayashi

Doctor of Philosophy in Physics

University of California, Irvine, 2025

Professor Bill Heidbrink, Chair

Fast-ion charge-exchange spectroscopy is used in experiments to measure the phase-space distribution of fast ions populated by neutral beam injection. The intense cold Dα emission is blocked by a neutral density filter but a novel filter method is demonstrated on a prototype fast ion Dα spectrometer for the JT60-SA tokamak. With the appropriate wavelength calibration, an ultra-narrow bandpass filter creates a 1 nm wide notch centered at the cold Dα wavelength. Experiments are conducted on the Large Helical Device to measure fast ions using fast-ion charge-exchange spectroscopy and neutron emission. Neutral beam modulation is used to acquire background-subtracted fast-ion charge-exchange measurements. The fast ion distribution is inferred from measurements using artificial signals calculated by the synthetic diagnostic code FIDASIM. For select cases, a full 5D distribution model is employed with neoclassical transport effects. For analysis of multiple samples, a reduced model is employed that includes classic slowing-down of fast ions but lacks neoclassical transport effects. The performance of a new spectroscopic sightline that is weighted to fast ions near the 160 keV neutral beam injection energy is evaluated in deuterium experiments. The new sightline is compared to the original sightline that is weighted to fast ions around 50 keV. Samples are selected from a larger dataset of deuterium and hydrogen experiments using a quantitative measure of magnetohydrodynamic instabilities. Quiescent cases with little to no instabilities observed in the measured magnetic fluctuations are selected for a parametric

study of fast ion measurements. Measured dependencies of the original low-energy sightline on neutral beam heating power, electron density, and electron temperature are found to be weaker than expected for a local approximation. Additionally, the new high-energy sightline is found to have poor spatial resolution causing more disagreement with the local model. Experiment/theory ratios are evaluated for neoclassical effects due to a shifted magnetic axis since neoclassical transport is not included in the theoretical model. The inward-shifted axis configuration in the Large Helical Device improves confinement of the bulk plasma and trapped fast ions. The fast-ion charge-exchange diagnostic is only able to see passing orbit fast ions and any improved confinement is not measured. Neutron emission measurements show an increase in experiment/theory values in the inward-shifted configuration that would indicate improvement in neoclassical confinement. This is due to the diagnostic sensitivity of neutron diagnostics which includes trapped fast ion orbits. In addition to analysis of quiescent cases, samples with measured instabilities are analyzed for any measured fast ion interaction with Alfvén eigenmodes. While mode activity is observed in high-field discharges with toroidal field of 2.75 T, there is no significant deviation of experiment/theory values compared to quiescent cases. Fast ion measurements in low-field discharges with toroidal field of 1.0 T appear to show some fast ion transport due to Alfvén eigenmodes.

Chapter 1

Introduction

1.1 Fusion plasmas

With an increasing global demand for clean and reliable energy sources, fusion energy stands at the forefront with a promise of steady and efficient energy production. Nuclear fusion is the process in which light nuclei fuse to create heavier nuclei. Considerable energy is required to induce these reactions. However, the energy released by these reactions can be much higher [1]. Sustaining fusion reactions in order to produce net positive energy presents a variety of scientific and engineering challenges.

Fusion reactions in laboratory experiments, as well as future reactors, rely on the hydrogenic isotopes: deuterium (^{2}H or D) and tritium (^{3}H or T). The preferred D-T fusion reaction produces a 3.5 MeV α particle (^{4}He) and a 14 MeV neutron, see eq. 1.1. In a well confined system, the fusion-born α can deposit its energy back into the system and create a chain

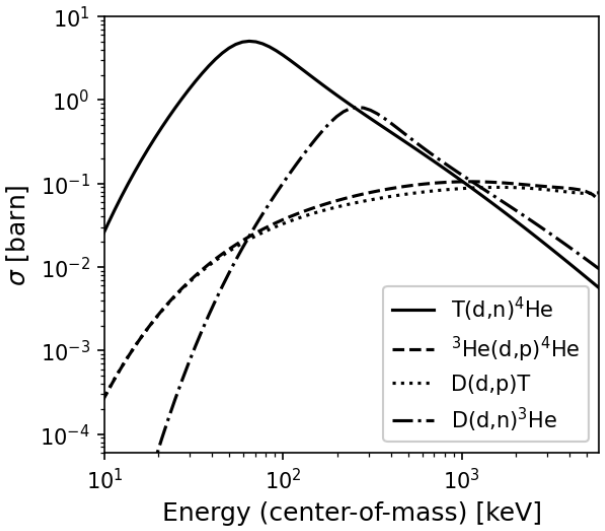

Figure 1.1: Fusion cross sections in the center of mass frame for the deuterium fuel cycle reactions.

reaction, a necessary condition for a steady state reactor.

$$\mathrm{D} + \mathrm{T} \rightarrow \alpha\ (3.52\ \mathrm{MeV}) + n\,(14.06\,\mathrm{MeV}) \tag{1.1}$$

$$\mathrm{D} + \mathrm{D} \rightarrow \mathrm{T}\,(1.01\,\mathrm{MeV}) + p\,(3.02\,\mathrm{MeV}) \tag{1.2}$$

$$\rightarrow {}^3\mathrm{He}\,(0.82\,\mathrm{MeV}) + n\,(2.45\,\mathrm{MeV}) \tag{1.3}$$

$$\mathrm{D} + {}^3\mathrm{He} \rightarrow \alpha\ (3.6\ \mathrm{MeV}) + p\,(14.7\,\mathrm{MeV}) \tag{1.4}$$

While multiple branches exist in the deuterium fuel cycle (eq. 1.1-1.4), a fuel mixture of equal parts deuterium and tritium is preferred due to the peak in the fusion cross section [2] shown in Fig. 1.1. In addition to maintaining the energy necessary for D-T fusion, the density of reactants and the energy confinement time must be sufficient to sustain reactions. Under the right conditions, the fuel can form a plasma composed of the reactants' nuclei as charged particle species as well as the electrons stripped from the atoms as another species. Confinement of fusion plasmas has led to configurations that employ a variety of techniques for producing energy.

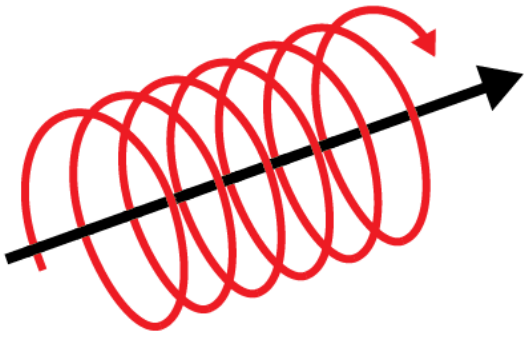

Figure 1.2: Cyclotron orbit of an ion following a field line.

Magnetic confinement fusion (MCF) is a method for confining fusion plasmas using magnetic fields. With careful control of magnetic fields, the charged particles in the plasma can be confined and compressed to induce fusion reactions [3]. Charged particles follow a helical trajectory around the magnetic fields lines. An example of a helical trajectory is shown in Fig 1.2. In order to maintain confined orbits, toroidal MCF devices bend field lines into closed loops forming a toroidal geometry. The curved geometry presents unique challenges in axisymmetric configurations that can be further complicated when considering nonaxisymmetric geometries.

1.2 Stellarator

Toroidal magnetic confinement devices, namely the tokamak and stellarator, are leading candidates for a fusion reactor due to their ability to confine fusion plasmas in a steady state. Tokamaks offer a relatively simple method for confining a fusion plasma in an axisymmetric toroidal geometry. The magnetic field for tokamak confinement relies in part on an induced current in the plasma that can lead to disruptions [4]. On the other hand, stellarators rely on external coils with no requirement for an induced current to generate the necessary magnetic field [5]. This removes the risk of disruption and would allow a stellarator to

operate for extended periods of time. However, producing a magnetic field structure in a stellarator without an internal current requires non-axisymmetric geometries, leading to complex magnetic coils and plasma shapes [6, 7]. The scientific and engineering complexities of stellarators pose unique challenges to producing net fusion energy on Earth.

Plasmas in toroidal devices are defined in coordinate systems that are best suited for describing the plasma and magnetic field structure. Aside from the standard cartesian coordinate system (x, y, z), the general toroidal geometry is described using cylindrical coordinates (R, Z, ϕ), where R is the major radius ($R = 0$ at the toroidal axis of rotation), Z is the vertical position ($Z = 0$ at the midplane), and ϕ is the toroidal angle [4]. Different coordinate conventions may define ϕ as positive or negative in the counter-clockwise (CCW) direction. In this thesis we will refer to CCW as the direction of increasing ϕ. The genus one topology of toroidal plasmas can be defined in greater detail through the use of flux coordinates (ψ, θ, ϕ) due to the existence of nested toroidal flux surfaces [3]. Flux surfaces are surfaces within the plasma or magnetic field structure where a given flux coordinate is constant. These nested surfaces surround the magnetic axis at the core of the plasma. We will refer to the radial flux coordinate ψ as the toroidal flux which goes to 0 at the magnetic axis. Angular coordinates θ and ϕ refer to the poloidal and toroidal angles, respectively. Due to the non-axisymmetric nature of stellarators, we employ a special coordinate system referred to as Boozer coordinates $(\psi, \theta_B, \zeta_B)$ [8]. Again, we chose ψ to refer to toroidal flux as the radial flux coordinate. The poloidal and toroidal coordinates are defined by θ_B and ζ_B, respectively. Boozer coordinates are straight-field-line coordinates, referring to the structure of magnetic field lines in the coordinate system. The magnetic field $\boldsymbol{B}$ is defined in Boozer coordinates with the covariant form

$$\boldsymbol{B} = I(\psi)\nabla\theta_B + G(\psi)\nabla\zeta_B + K(\psi, \theta_B, \zeta_B)\nabla\psi. \tag{1.5}$$

Parameter name	Value
Major radius R_{ax}	3.55 - 3.90 m
Minor radius a	0.6 m
Volume V_p	30 m^3
Field periods N_{fp}	10
Helical coils ℓ	2
Magnetic field B_t	0.50 - 2.75 T

Table 1.1: Device specifications for LHD

The contravariant form is defined in terms of the position vector $\boldsymbol{r}(\psi, \theta_B, \zeta_B)$

$$\boldsymbol{B} = \frac{\iota}{\sqrt{g}} \frac{\partial \boldsymbol{r}(\psi, \theta_B, \zeta_B)}{\theta_B} + \frac{1}{\sqrt{g}} \frac{\partial \boldsymbol{r}(\psi, \theta_B, \zeta_B)}{\zeta_B}, \tag{1.6}$$

where the rotational transform $\iota(\psi) = \boldsymbol{B} \cdot \nabla\theta_B / \boldsymbol{B} \cdot \nabla\zeta_B$ corresponds to the ratio of poloidal turns to toroidal turns. The Jacobian $\sqrt{g}$ is then defined as

$$\sqrt{g}(\psi, \theta_B, \zeta_B) = \frac{G(\psi) + \iota I(\psi)}{B^2(\psi, \theta_B, \zeta_B)}. \tag{1.7}$$

The scalar functions $G(\psi)$ and $I(\psi)$ correspond to the poloidal and toroidal currents. Toroidal coordinates systems will be further discussed in sec. 3.2.2 and sec. 3.2.3.

1.3 Large Helical Device

The Large Helical Device (LHD) is a heliotron-type stellarator that relies on two helical coils wound around the toroidal device. The present work is focused primarily on experiments at LHD with a brief discussion of hardware prototyping for the JT60-SA tokamak in sec. 2.2. Basic LHD parameters are listed in table 1.1 [9]. A top-down midplane view of LHD and a typical plasma boundary surface is shown in Fig. 1.3. LHD is a $\text{N}_{\text{fp}} = 10$ field period device with $\ell = 2$ helical coils that have a pitch of $\ell/\text{N}_{\text{fp}} = 2/10$. Most experiments in LHD rely on neutral beam injection (NBI) to heat the plasma [10]. Electron cyclotron heating

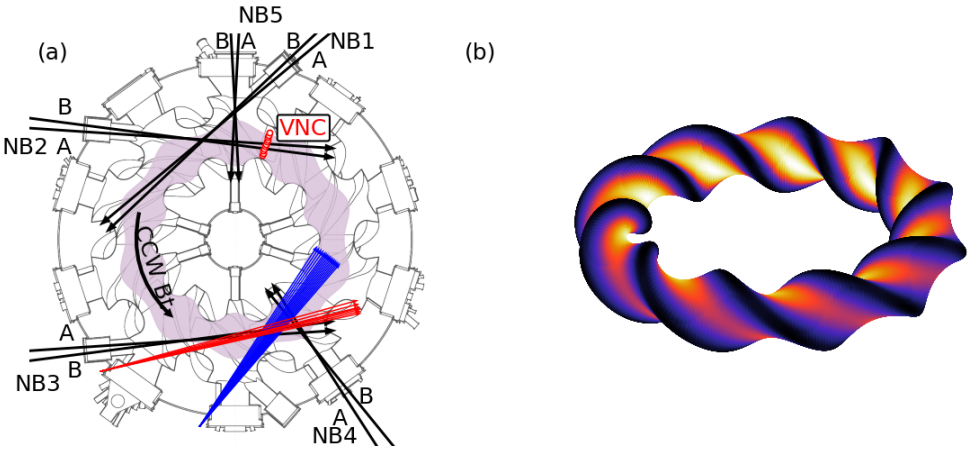

Figure 1.3: (a) Top-down midplane view of LHD. Black arrows indicate beamlines for each NBI source. Only upper-A and upper-B ports are shown for NB4 and NB5. Blue and red arrows indicate fast-ion charge-exchange spectroscopy sightlines for the 6-O port and the 7-O port, respectively. The counter-clockwise (CCW) B_t direction is also shown with a curved arrow. Open red circles indicate channel locations for the vertical neutron camera (VNC). (b) Boundary surface calculated using the 3-D equilibrium code VMEC [13]. Colors represents magnetic field strength with lighter colors corresponding to higher field strength.

(ECH) and ion cyclotron heating (ICH) systems are available as well [11, 12]. ICH will not be considered in the present study. Some discussion of ECH-heated cases will be presented but the majority of cases in the present study are only heated by NBI. Ions are accelerated in the NBI system using an applied voltage and then neutralized and injected into the plasma. Injected neutrals can then become ionized through charge exchange interactions, depositing their energy. Two NBI systems are used on LHD: negative-ion source NBIs (NNBI) and positive-ion source NBIs (PNBI). The NNBIs use two sources per beamline, labeled source A and B in Fig. 1.3(a). The PNBIs use four sources per beamline in a 2x2 grid, labeled upper-A, lower-A, upper-B, and lower-B. In a deuterium plasma, NNBIs operate with an injection energy E_{inj} of 160 keV and an injection power P_{inj} of 1.5 MW per source while PNBIs operate with E_{inj} of 60 keV and P_{inj} of 2 MW.

LHD is equipped with a host of diagnostics for measuring various plasma parameters. Experimental data in this thesis relies on electron density n_e and temperature T_e measured by a Thomson scattering system [14] as well as ion density n_i and temperature measured by a

charge exchange spectroscopy (CXS) system [15]. The CXS system relies on carbon impurity emission due to carbon impurities introduced by the graphite tiles. Additional diagnostics will be discussed further in sec. 1.5 and ch. 2.

1.4 Fast ions

Fast ions are a minority population that is often present in fusion plasmas due to the production of α particles (eq. 1.1) or due to ionization of injected neutrals [16]. The energetic population of fast ions carry energy (3.5 MeV α, 166 keV NBI birth) that is orders of magnitude greater than the thermal ion temperature $\mathrm{T_i}$ ($\sim$ 10 keV). In order to keep the plasma hot, these fast ions must be confined long enough to deposit their energy back into the bulk plasma. The fast ion distribution $f_\mathrm{f} \equiv f_\mathrm{f}(\boldsymbol{v}_i, \boldsymbol{r}_i)$ is a full phase space distribution in velocity $\boldsymbol{v}_i$ and position $\boldsymbol{r}_i$ space. The velocity component is often defined in terms of the total energy E_f of a fast ion and the parallel pitch $v_{||}/v$. Here, $v_{||}$ is the parallel velocity component with respect to the magnetic field B

$$v_{||} = \frac{\boldsymbol{v} \cdot \boldsymbol{B}}{B}. \tag{1.8}$$

Fast ions that maintain a positive $v_{||}$ over a toroidal orbit are considered co-parallel passing fast ions. Similarly, fast ions that maintain a negative $v_{||}$ are considered counter-parallel passing fast ions. In LHD with CCW B_t, NB1 and NB3 populate co-passing fast ions and NB2 populates counter-passing fast ions. If $v_{||}$ passes 0, the fast ion reverses direction and enters a trapped orbit. This is often due to conservation of the adiabatic invariant $\mu = mv_\perp^2/2B$ where $v_\perp$ is the velocity component perpendicular to the magnetic field. In toroidal devices, the toroidal well of the magnetic field is defined by an increase in field strength on the inboard side and a decrease on the outboard side. Assuming low collisionality, as a fast ion moves from a region of low field to high field, $v_\perp$ increases and $v_{||}$ decreases due to conservation

of energy and μ. If the total fast ion velocity $v_f = \sqrt{v_{||}^2 + v_{\perp}^2}$ is low enough, $v_{||}$ goes to 0 resulting in a bounce orbit. In tokamaks this results in a banana orbit. Stellarators have an additional helical ripple well due to the non-axisymmetric field structure. Fast ions that repeatedly bounce within the helical ripple are considered to be in trapped orbits. In LHD, a deeply-trapped orbit occurs when a fast ion remains helically trapped through a complete poloidal orbit. If a fast ion only remains helically trapped for a portion of the poloidal orbit and transitions to a toroidally trapped orbit near B_{min} then the fast ion is considered to be in a weakly-trapped orbit. Many fast ion orbits have been identified due to the complexity of stellarator geometries [17], however only passing, deeply-trapped, and weakly-trapped orbits will be considered in the present work. Fast ion orbits will be further discussed in section 5.3.

Fast ion distributions are often not in equilibrium with the background plasma and cannot be described by a Maxwellian distribution [18]. Fusion born α particle distributions are isotropic slowing-down distributions with a well-defined energy peak around 3.5 MeV. The spatial distribution is peaked at the magnetic axis due to the peak in electron and temperature profiles of the background plasmas. NBI born fast ion distributions are non-isotropic slowing down distributions due to the direction of the neutral beam. The spatial distribution of NBI fast ions may be on- or off-axis depending on the geometry of the beam. Only the NBI fast ion distribution function is considered in the present work.

1.5 Fast ion diagnostics

The fast ion distribution in LHD is diagnosed using fast-ion charge-exchange spectroscopy (FICXS) and neutron emission. Additional fast ion diagnostics are available on LHD, namely a neutral particle analyzer system [19]. Only FICXS and neutron emission are considered in the present work due to the use of multiple channels that produce a radial profile. FICXS is an active neutral beam charge-exchange system that relies on Balmer-alpha spectroscopy

[20, 21] and is the primary diagnostic used in the present work. Additional details on the diagnostic method will be discussed in sec. 2.1. Two neutron emission systems, neutron flux monitor (NFM) and vertical neutron camera (VNC) [22], measure neutrons produced in D-D reactions (eq. 1.3) deuterium beam interactions with the deuterium plasma. NFM measures the calibrated total neutron emission rate and is a standard fast ion diagnostic in LHD [23, 24, 25], as well as other fusion devices [26]. VNC uses multiple vertical channels to produce a line-integrated radial profile of neutron emission. Due to the positive dependence on energy of the D(d,n)^{3}He (Fig. 1.1), the neutron emission diagnostics are more sensitive to fast ions with higher energies. Velocity-space sensitivity of the various fast ion diagnostics will be discussed further in sec. 5.2.2.

1.6 Alfvén eigenmodes

Fast ions in toroidal devices also play a role in the excitation of instabilities. Alfvén eigenmodes (AE) are a class of magnetohydrodynamic (MHD) instabilities that exist as transverse low-frequency electromagnetic waves traveling along field lines [27] in the plasma. Modes in the Alfvén continuum have the dispersion relation $\omega = k_{||} \mathrm{v_A}$ and are dependent on the wave vector $k_{||}$ parallel to the magnetic field and the Alfvén velocity $\mathrm{v_A} = B/\sqrt{\mu_0 \sum_i n_i m_i}$, where $\mathrm{n_i}$, m_i, and subscript i are thermal ion density, mass, and species index i, respectively. Due to the radial dependence of ion density $\mathrm{n_i}$ and magnetic field strength B, the Alfvén velocity and mode frequency are functions of radial position. This results in a shearing effect due to the different velocities of the wave across the plasma volume and the wave can experience continuum damping. Due to toroidal and poloidal periodicity of toroidal devices, gaps can appear in the Alfvén continuum. AEs that reside in these gaps experience weak continuum damping and can be excited due to fast ions. Stellarators have additional helical coupling

that also contributes to gap formation [28]. AEs with finite amplitude can be excited within these gaps due to weak continuum damping.

Gap frequencies in stellarators can be described using the Fourier representation of the magnetic field strength in flux coordinates [29]

$$B(\psi,\theta,\phi)/B_0 = 1 + \sum_{\mu,\nu} \varepsilon^{\mu,\nu}(\psi)\cos(\mu\theta - \nu \mathrm{N_{fp}}\phi), \tag{1.9}$$

where B_0 is the average field strength, $\varepsilon^{\mu,\nu}$ is the Fourier amplitude, and $\mathrm{N_{fp}}$ is the number of toroidal field periods ($\mathrm{N_{fp}^{LHD}} = 10$). The rotational transform at the gap is

$$\iota^* = \frac{2n + \nu \mathrm{N_{fp}}}{2m + \mu} \tag{1.10}$$

where n and m toroidal and poloidal mode numbers, respectively. The gap frequency is

$$f^{\mu,\nu} = |\nu q^* \mathrm{N_{fp}} - \mu| \left(\frac{v_A}{4\pi R q^*}\right) \tag{1.11}$$

$$= \left|\nu \left(\frac{m}{n}\right) \mathrm{N_{fp}} - \mu\right| \left(\frac{2m+1}{2m+\mu}\right) \frac{v_A}{4\pi R[(2m+1)/2n]} \tag{1.12}$$

where the safety factor $q^* = 1/\iota^*$ is the inverse of the rotational transform. The Fourier mode numbers μ and ν describe the various classes of AEs that are produced by coupling of different modes. Of particular interest in LHD are the toroidal (TAE), ellipticity-induced (EAE), and helical Alfvén eigenmodes (HAE) with the following frequencies [30]

$$f_{TAE}(\mu = 1, \nu = 0) = \frac{v_A}{4\pi R[(2m+1)/2n]} \tag{1.13}$$

$$f_{EAE}(\mu = 2, \nu = 0) = 2\left(\frac{2m+1}{2m+2}\right) f_{TAE} \tag{1.14}$$

$$f_{HAE}(\mu = 2, \nu = 1) = \left|\left(\frac{m}{2n}\right) N - 1\right| f_{EAE} \tag{1.15}$$

Interaction between these AEs and fast ions is described by the resonance condition

$$v_{\mathrm{f}||}/v_A = \frac{1}{1 \pm 2/(\nu \mathrm{N_{fp}} q^* - \mu)} \tag{1.16}$$

where $v_{\mathrm{f}||}$ is the fast ion velocity component parallel to the magnetic field. For a TAE, the resonance condition is $v_{\mathrm{f}||}/v_{\mathrm{A}}$ = -1, 1/3, where -1 corresponds to the primary resonance frequency and 1/3 is a sideband resonance frequency. AEs and fast ion interactions will be discussed further in ch. 6.

1.7 Thesis overview

The following dissertation is composed of seven chapters. Chapter 1 covers the introduction with background on fusion plasmas, the Large Helical Device stellarator, and fast ions. Chapter 2 provides background on the primary fast ion diagnostic along with project details for a prototype fast ion spectrometer and hardware details for the LHD diagnostic. Chapter 4 introduces the synthetic diagnostic code FIDASIM which is used to infer the fast ion distribution from measurements. New feature implementations and fast ion distribution models are also discussed. Chapter 3 presents published results [31] on the evaluation of a new diagnostic sightline for the LHD fast ion diagnostic system. Chapter 5 covers the bulk of the thesis research and is divided into three sections. Section 5.1 details the selection process for discharges with little to no magnetohydrodynamic instabilities. Analysis of selected experimental data is discussed in section 5.2 followed by discussion of simulations in section 5.3. Results for cases with Alfvén eigenmode activity are presented in chapter 6. A summary is provided in chapter 7 along with discussion of future work.

Chapter 2

Fast-ion charge-exchange spectroscopy

This section discusses the fast ion charge exchange spectroscopy (FICXS) system on LHD in greater detail. Diagnostic sightlines for FICXS will be referred to as line-of-sight or LOS.

2.1 Diagnostic concept

The underlying method of using Balmerα emission as an active charge exchange diagnostic technique is also known as fast-ion Dα (FIDA) or fast-ion Hα (FIHA) in deuterium and hydrogen plasmas [20]. A diagram of the diagnostic method is shown in Fig. 2.1. FICXS relies on a dedicated diagnostic neutral beam (DNB) to inject neutrals into the plasma. Injected neutrals can charge exchange with a fast ion, producing an excited neutral according to eq. 2.1

$$\mathrm{D}^0 + \mathrm{D}^+ \rightarrow \mathrm{D}^+ + \mathrm{D}^{0*} \tag{2.1}$$

$$\mathrm{D}^{0*} \rightarrow \mathrm{D}^0 + h\nu \tag{2.2}$$

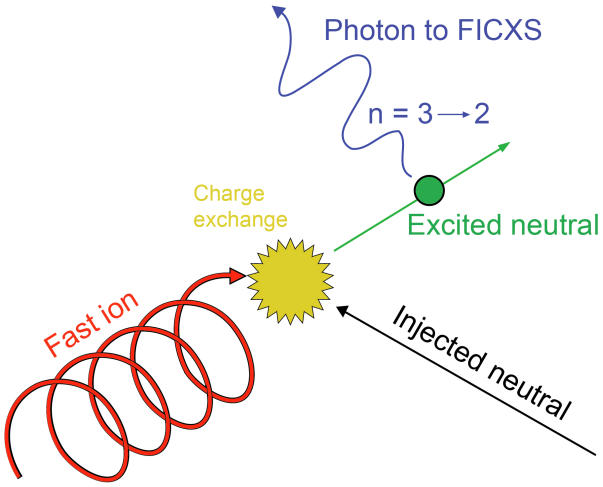

Figure 2.1: Diagram of fast-ion charge-exchange process and Balmer-α emission.

Excited neutrals in the n = 3 state can then undergo a Balmer transition to drop to the n = 2 state and emit a photon (eq. 2.2). The emitted photon, Doppler-shifted due to the velocity of the original fast ion, is captured by fiber optic cables and transmitted to a spectrometer. An example of a background-subtracted FICXS measurement is shown in Fig. 2.2. Additional details on spectrometer design are presented in the next section and details on the calculation of the net signal are presented in section 2.4.

Careful choice of the FICXS sightline geometry produces a phase-space resolved measurement of the fast ion distribution. Multiple radially-distributed channels are used to construct a radial profile that provides information on the spatial distribution of fast ions. The wavelength dependence of the FID(H)A feature provides information on the velocity-space distribution. In the present work, we will treat velocity-space as 2D in energy and pitch ($v_{||}/v$). Emission from fast ions with higher energy will experience larger Doppler shift from the unshifted Dα wavelength 656.10 nm (Hα 656.28 nm). Only the fast ion component that is parallel to the sightline contributes to the Doppler shift. Therefore, a given wavelength can correspond to a range in energy and pitch. The velocity-space sensitivity of FICXS LOS is discussed further in ch. 5.

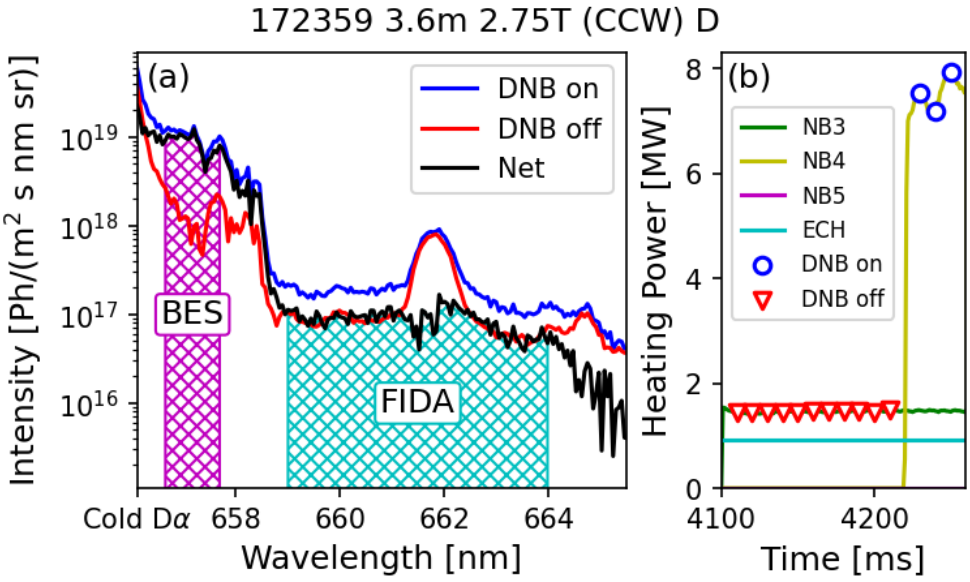

Figure 2.2: Background-subtracted FICXS spectrum for a 6-O LOS channel. (a) Measured intensity averaged over the diagnostic neutral beam (DNB) on time (blue) and DNB off time (red). The background-subtracted net signal is shown in black. Beam emission spectroscopy (BES) and FIDA features are shown with magenta and cyan hatching, respectively. (b) Diagnostic beam patterns with open blue circles indicating DNB on time stamps and open red triangles indicating DNB off time stamps.

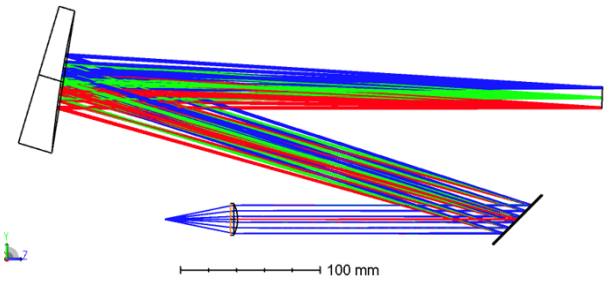

Figure 2.3: Diagram of prototype spectrometer in Zemax. Only the input from fibers, collimating lens, diffraction grating, off-axis parabolic mirror, and camera sensor are shown. The ultra-narrow bandpass filter is not shown.

2.2 Cold Dα filter methods

FID(H)A emission tends to have much lower intensity than the cold D(H)α emission so special techniques must be employed to avoid saturation on the diagnostic instrument. This section will discuss the development of a novel filter technique used in a prototype FICXS spectrometer developed at the DIII-D tokamak for installation on the JT-60SA tokamak. FICXS spectrometers at various devices use a neutral density filter or blocking bar to mask the cold D(H)α emission [21, 32]. Due to the proximity of the mask to the focal plane, there can be an some amount of scattered light or blooming that appears as artifacts in the measurement. Another method is to use an ultra-narrow bandpass (UNB) filter at the front of the spectrometer. This directs the intense cold D(H)α emission into a light dump and reduces scattering or blooming effects [33]. Figure 2.3 shows a diagram of the prototype spectrometer model in Zemax OpticStudio. An image of the prototype on an optical bench at DIII-D is shown in Fig. 2.4. Light is collected with two 200 μm fibers that have an F-number of 2.5. Diffraction is done with a blaze grating with a blaze angle of 26.7° and a grating density of 1800 grooves per mm. An off-axis parabolic (OAP) mirror with a 15° offset angle is used for the focusing optic. The camera is a SRI Avanti 768 with 768×256 pixels that are 18×18 μm^2 in size. The two fibers are separated vertically on the camera lens with channel 1 on the top half and channel 2 on the lower half.

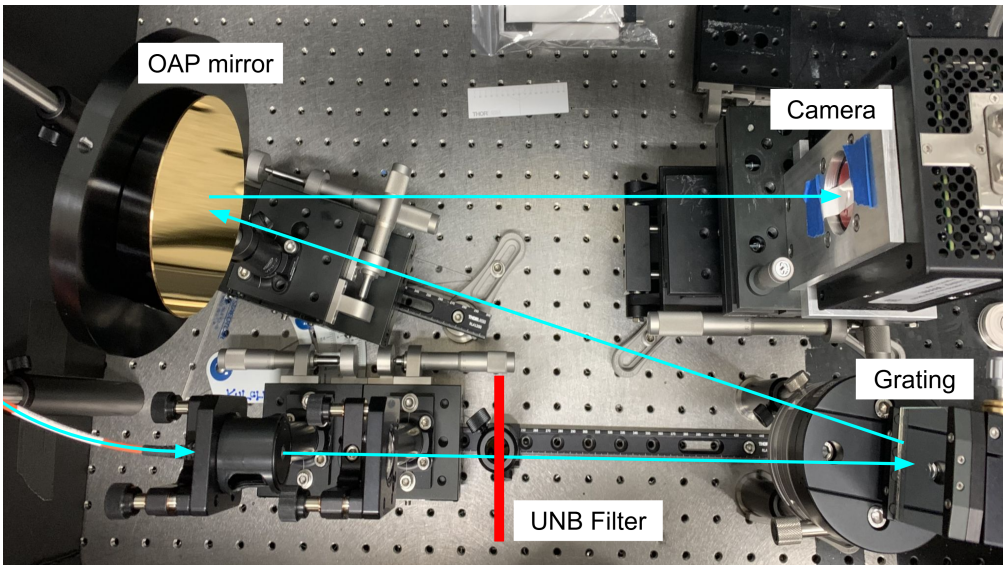

Figure 2.4: Image of prototype spectrometer on the optical bench. The path of light through the spectrometer is indicate by cyan arrows. The location of the ultra-narrow bandpass (UNB) filter is shown in red. Also pictured are the diffraction grating, off-axis parabolic (OAP) mirror, and camera.

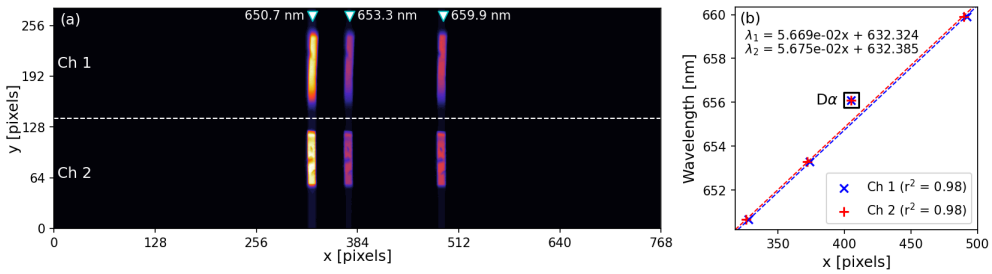

Figure 2.5: Wavelength calibration for the prototype spectrometer using the (a) neon lamp emission. The dispersion relation in (b) is calculated using neon emission along with Dα emission (highlighted with square marker). Dispersion relations for both channels and resulting r^2 values are listed.

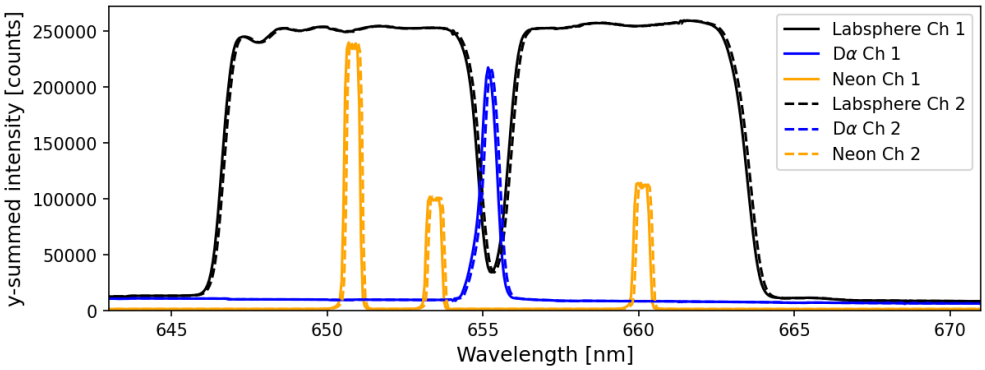

Figure 2.6: Measured spectrum of labsphere, Dα lamp, and neon lamp for both channels.

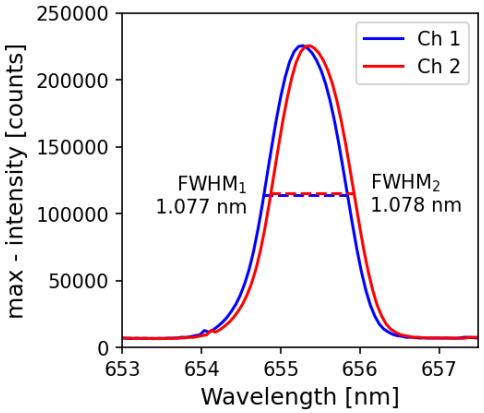

Figure 2.7: Full-width half-maximum (FWHM) calculated for the notch produced by the ultra-narrow bandpass filter.

Wavelength calibration of the prototype spectrometer is conducted using a neon lamp as well as a Dα lamp. Three emission lines for neon are measured at 650.7, 653.3, and 659.9 nm and one emission line for Dα is measured at 656.1 nm. The dispersion relation is calculated using linear regression of the emission location in pixels and the emission line wavelengths. Results of the calibration are shown in Fig. 2.5 with 5.67×10^{-2} nm per pixel. The wavelength spectra of an integrating labsphere, the neon lamp, and the Dα lamp are shown in Fig. 2.6 with a notch in the labsphere signal due to the UNB filter. With the filter, there is an 80% reduction in the emission around 656.1 nm.

A notch width of 1 nm is ideal in order to ensure broad coverage of the FIDA feature with sufficient blocking of the cold D(H)α emission. The notch width is characterized by the full-

	6OFIDA		PNBFIDA		NNBFIDA	
Ch	View Port	R [m]	View Port	R [m]	View Port	R [m]
1	6	2.958	7	4.061	7	3.943
2	6	3.029	7	3.943	7	3.943
3	6	3.099	7	3.829	7	4.120
4	6	3.168	7	3.713	7	4.061
5	6	3.237	6	3.029	7	4.002
6	6	3.283	6	3.168	7	3.955
7	6	3.329	6	3.283	7	3.943
8	6	3.374	6	3.329	7	3.931
9	6	3.419	6	3.374	7	3.829
10	6	3.464	6	3.419	7	3.713
11	6	3.509	6	3.464	6	3.237
12	6	3.553	6	3.509	6	3.329
13	6	3.597	6	3.553	6	3.419
14	6	3.642	6	3.597	6	3.509
15	6	3.685	6	3.641	6	3.597
16	6	3.729	6	3.685	6	3.685

Table 2.1: Three FICXS sightline configurations used on LHD. Diagnostic channels for each configuration are listed with the associated view port and the radial location of the intersection with the diagnostic beam. Sightlines are grouped and labeled according to their view ports (6-O LOS and 7-O LOS).

width half-maximum (FWHM) of the inverted notch. The notch is inverted by taking the difference between the maximum signal and the spectrum. Inverted profiles and calculated FWHM are shown in Fig. 2.7. Both channels have excellent agreement with the ideal 1 nm FWHM with approximate errors of 8%.

2.3 LHD hardware

The FICXS system on LHD uses 16 channels with 400 μm optical fibers for each channel that direct collected light to a FLP-200 BUNKOKEIKI spectrometer with a grating number of 1200 mm, focal length of 200 mm, and F-number of 2.8. Emission spectrum is measured on an iXon 897 ANDOR electron multiplying charge-coupled device (EMCCD) [21] The intense cold Dα feature (Hα in hydrogen plasmas) is blocked using a notch filter. Three sightline

configurations listed in table 2.1 are used throughout experiments presented in the present work.

2.4 Data processing

FICXS data presented in the following sections are calculated from background subtraction using beam modulation and normalized to the beam emission spectroscopy (BES) feature. BES-normalization is utilized due to (a) removing variations in local neutral density and (b) removing variations in instrumental factors. Both FICXS and BES signal for each channel are dependent on the local neutral density n_{DNB} due to the diagnostic neutral beam. Additionally, instrument specifications such as the gain factor for the camera varies between experiments. By normalizing the FICXS signal with BES, variations that are not relevant to the present study are removed. Wavelength-resolved FICXS samples are measured with a sampling rate of 100 Hz or 1 frame per 10 ms. The camera uses an exposure time of 7 ms, leaving the shutter closed for 3 ms. Active signals are taken from time stamps when the diagnostic beam is on. Passive signals are taken from time stamps when the diagnostic beam is off but the background heating beams are on. Selected DNB-on and DNB-off samples are shown in Fig. 2.2(b) with the resultant time-averaged background-subtracted signal in Fig. 2.2(a). Background-subtracted FIDA density is calculated with the appropriate error

propagation using the following equations

$$S_{\mathrm{i,j}}(t) = \int_{\lambda_j} S_{\mathrm{i}}(t,\lambda) d\lambda \tag{2.3}$$

$$\Delta S_j = \langle S_{\mathrm{active}} \rangle_t - \langle S_{\mathrm{passive}} \rangle_t \tag{2.4}$$

$$\sigma_j = \sqrt{\sigma_{\mathrm{active}} + \sigma_{\mathrm{passive}}} \tag{2.5}$$

$$S_y = \Delta S_{\mathrm{FIDA}} / \Delta S_{\mathrm{BES}} \tag{2.6}$$

$$\sigma_y = |S_y| \sqrt{\left(\frac{\sigma_{\mathrm{FIDA}}}{\Delta S_{\mathrm{FIDA}}}\right)^2 + \left(\frac{\sigma_{\mathrm{BES}}}{\Delta S_{\mathrm{BES}}}\right)^2} \tag{2.7}$$

where $i \in \{\text{active, passive}\}$ and $j \in \{\text{FIDA, BES}\}$ indicate the active and passive signals of the FID(H)A and BES features. Angle brackets $\langle\,\rangle$ and σ represent simple arithmetic mean and standard deviations over time.

Chapter 3

Forward modeling with FIDASIM

The fast ion distribution measured by FICXS and VNC is analyzed using forward modeling with the synthetic diagnostic code FIDASIM. This section discusses details on FIDASIM including recent feature implementations and comparison of fast ion distribution models.

3.1 Simulation method

FICXS measurements are compared to signals produced by the synthetic diagnostic code FIDASIM [34] extended to 3D geometries [35]. FIDASIM uses the measured plasma and beam parameters from the experiment along with a fast-ion distribution model to calculate a FICXS signal. The calculation of the FICXS signal S is dependent on a weight function $W(\boldsymbol{X})$ that describes the phase-space sensitivity of a given diagnostic sightline

$$S = \int W(\boldsymbol{X}) f(\boldsymbol{X}) d\boldsymbol{X} \tag{3.1}$$

where $f(\boldsymbol{X})$ is the fast-ion distribution function and $\boldsymbol{X}$ represents the phase-space coordinates. Fast ion distributions for FIDASIM are often represented in terms of 2 velocity-space

coordinates: energy and pitch ($v_{||}/v$), as well as 2 or 3 real-space coordinates: R, Z, ϕ, where ϕ is only considered for non-axisymmetric cases. Weight functions calculated by FIDASIM are represented in terms of energy, pitch and wavelength λ. The synthetic signal includes the FID(H)A feature as well as the BES full, half, and third energy components, the beam-thermal halo and direct charge-exchange (DCX) features, and the background bremsstrahlung emission. Emission due to thermal-thermal interactions is also possible with FIDASIM but is not included due to the lack of reliable measurements of the thermal neutral profile. In addition to spectral features, neutron emission is also calculated by FIDASIM for the total neutron emission rate. Recently, synthetic neutron camera signals were also implemented in FIDASIM and are used for further interpretation of the fast ion distribution using VNC measurements.

3.2 Feature implementation

This section discusses features implemented into FIDASIM by the author as part of the development and maintenance team. The three main implementations are adaptive grid cells to account for sharp gradients in plasma parameters, COCOS system to allow inputs of any coordinate system, and VMEC support to allow for input field structure generation for 3D equilibria. These features are part of the FIDASIM version 3.0 development.

3.2.1 Adaptive grid cells

The simulation space in FIDASIM is defined on a background passive grid in cylindrical coordinates (R, Z, ϕ) with field and plasma parameters mapped to the cylindrical grid. An additional beam grid is defined in cartesian coordinates (x, y, z) with x along the beamline axis ($x = 0$ at the NBI source), y and z respectively define the horizontal and

vertical position from the beamline. Regions with sharp gradients between grid cells can lead to numerical errors, impacting accuracy of calculations in those regions. Adaptive grid cells are implemented in FIDASIM to account for these sharp gradients in the `track` and `track_cylindrical` subroutines. Neutrals in the beam grid (`track`) or the passive grid (`track_cylindrical`) are stepped through the grid cells. A user-selected plasma parameter is evaluated within the grid cell and a tolerance is used to split the cell into sub cells. The number of sub cells is defined as

$$N_{\text{sub}} = \text{ceil}\left(\frac{|\Delta f|}{\bar{f} d\ell \varepsilon}\right) \tag{3.2}$$

where f is a given parameter (n_e , T_e , etc.), Δ corresponds to the difference in f at the point of entry f_{in} and exit f_{out} from the grid cell, $\bar{f}$ is the average value within the cell, $d\ell$ is the path length of the neutral within the cell, and ε is a tolerance value. For a finite value $1 < N_{\text{sub}} \leq N_{\text{max}}$, the path of the neutral within the grid cell is split into smaller paths and the relevant calculations are evaluated for each sub path. For a full implementation of adaptive grid cells in the `track` subroutine see appendix A.

3.2.2 COCOS coordinate system

FIDASIM uses a right-handed cylindrical coordinate system in (R, ϕ, Z) but inputs to FIDASIM can come from a variety of different coordinate systems. The toroidal angle ϕ in FIDASIM increases in the counter-clockwise (CCW) direction when viewing the system from the top down. Inputs to FIDASIM are assumed to use right-handed toroidal coordinates (ρ, ϕ, θ), where ρ is the normalized minor radius and θ is the poloidal angle, as well as poloidal flux defined by the "ribbon" rather than the "disk". In this coordinate system, θ increases in the CCW direction when viewing the system from the front with the poloidal plane to the right of the toroidal rotation axis. The "ribbon" poloidal flux Ψ_P is defined as the flux

through a surface bounded by the magnetic axis ($\rho = 0$) and a flux surface ($0 < \rho \leq 1$). In contrast, "disk" poloidal flux is defined as the flux through a surface lying in the equatorial plane bounded by the toroidal rotation axis (R = 0) and a flux surface. A common input format for FIDASIM is GEQDSK files output by the TRANSP code [36] which uses the same coordinate system as FIDASIM. However, in order to generalize the coordinate system to accept inputs from different coordinate conventions, the *COordinate COnventionS* (COCOS) system has been adopted into FIDASIM [37].

COCOS is an identifier for the coordinate conventions of cylindrical and toroidal coordinates of a given code or set of equations. This also allows transformations between COCOS systems. There are a total of 16 COCOS systems numbered 1-8 and 11-18 that are identified by four integers: $e_{\mathrm{Bp}} \in \{0, 1\}$, $\sigma_{\mathrm{Bp}} \in \{-1, +1\}$, $\sigma_{\mathrm{R}\phi\mathrm{Z}} \in \{-1, +1\}$, $\sigma_{\rho\theta\phi} \in \{-1, +1\}$. The cylindrical and toroidal coordinate identifiers, $\sigma_{\mathrm{R}\phi\mathrm{Z}}$ and $\sigma_{\rho\theta\phi}$, are determined by the handedness of (R, ϕ, Z) and (ρ, θ, ϕ). For a right-handed (R, ϕ, Z) system, $\sigma_{\mathrm{R}\phi\mathrm{Z}} = +1$ and for a left-handed system it is -1. For a right-handed (ρ, θ, ϕ) system, $\sigma_{\rho\theta\phi} = +1$ and for a left-handed system it is -1. The poloidal flux identifiers, e_{Bp} and σ_{Bp} come from a general definition of the magnetic field $\boldsymbol{B}$ as

$$\boldsymbol{B} = F\nabla\phi + \sigma_{\mathrm{Bp}}\frac{1}{(2\pi)^{e_{\mathrm{Bp}}}}\nabla\phi \times \nabla\psi_{\mathrm{ref}} \tag{3.3}$$

where ψ_{ref} is the effective poloidal flux. σ_{Bp} is then defined to be +1 when ψ_{ref} increases with minor radius and -1 when it decreases with minor radius. Additionally, e_{Bp} is defined as 1 when $\psi_{\mathrm{ref}} = \Psi_P$ and 0 when $\psi_{\mathrm{ref}} = \Psi_P/(2\pi)$, where the poloidal flux Ψ_P is defined as

$$\Psi_P = -\sigma_{\mathrm{Bp}} \int \boldsymbol{B} \cdot \boldsymbol{dS_p} \tag{3.4}$$

The differential surface element $\boldsymbol{dS_p}$ has the direction of the magnetic field at the toroidal rotation axis (R = 0) due to a current in the positive ϕ direction. For any two given COCOS

COCOS	e_{Bp}	σ_{Bp}	$\sigma_{\mathrm{R}\phi\mathrm{Z}}$	$\sigma_{\rho\theta\phi}$	Code
1/11	0/1	+1	+1	+1	
2/12	0/1	+1	-1	+1	
3/13	0/1	-1	+1	-1	VMEC (CCW B_t LHD)
4/14	0/1	-1	-1	-1	
5/15	0/1	+1	+1	-1	TRANSP, FIDASIM
6/16	0/1	+1	-1	-1	
7/17	0/1	-1	+1	+1	
8/18	0/1	-1	-1	+1	

Table 3.1: All COCOS values with identifiers and select codes. COCOS ≤ 8 with $e_{\mathrm{Bp}} = 0$ refers to $\psi_{\mathrm{ref}} = \Psi_P/(2\pi)$ while COCOS ≥ 11 with $e_{\mathrm{Bp}} = 1$ refers to $\psi_{\mathrm{ref}} = \Psi_P$.

systems, the transformations are defined as

$$e_{\mathrm{Bp}} \rightarrow e_{\mathrm{Bp,in}} - e_{\mathrm{Bp,out}} \tag{3.5}$$

$$\sigma_{\mathrm{Bp}} \rightarrow \sigma_{\mathrm{Bp,in}}\sigma_{\mathrm{Bp,out}} \tag{3.6}$$

$$\sigma_{\mathrm{R}\phi\mathrm{Z}} \rightarrow \sigma_{\mathrm{R}\phi\mathrm{Z,in}}\sigma_{\mathrm{R}\phi\mathrm{Z,out}} \tag{3.7}$$

$$\sigma_{\rho\theta\phi} \rightarrow \sigma_{\rho\theta\phi,\mathrm{in}}\sigma_{\rho\theta\phi,\mathrm{out}} \tag{3.8}$$

COCOS values are listed in table 3.1 along with the COCOS values for FIDASIM, TRANSP, and the 3D equilibrium code VMEC [13]. The full transformation of field parameters is given by *Sauter, et al.* [37]. The general implementation and TRANSP-GEQDSK implementation of COCOS for preprocessing inputs to FIDASIM is given in appendix B; the VMEC implementation is given in appendix C.

3.2.3 VMEC input support

Magnetic field equilibria is often calculated for non-axisymmetric stellarator geometries using the 3D equilibrium code VMEC [13]. The VMEC field structure is defined in toroidal flux coordinate (s, θ, ϕ), where $s = \psi/\psi_{\mathrm{edge}}$ is normalized toroidal flux and θ and ϕ are poloidal and toroidal angles. FIDASIM uses a field structure in cylindrical coordinates (R, Z, ϕ_{cyl})

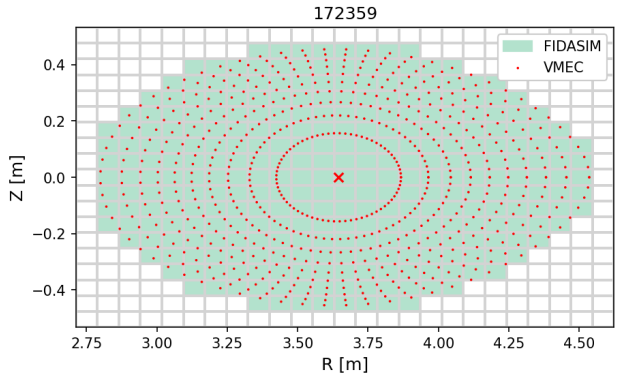

Figure 3.1: Interpolation of a vertical plane in VMEC coordinates to the R-Z plane in cylindrical coordinates. Red dots indicate grid centers in the VMEC s-θ plane, where $s = \psi/\psi_{\text{edge}}$ is normalized toroidal flux. The magnetic axis is marked by a red x. Gray lines indicate grid cell boundaries in cylindrical coordinates. Green shaded regions indicate cylindrical grid cells that are within the $s = 1$ surface.

so an appropriate transformation must be made to generate an input field structure from VMEC. Due to the periodic nature of stellarators, R and Z can be represented as Fourier series with cosine and sine terms as

$$R(s,\theta,\phi) = \sum_{m,n} R_{m,n}(s)\cos(m\theta - nN_{\text{fp}}\phi) \tag{3.9}$$

$$Z(s,\theta,\phi) = \sum_{m,n} Z_{m,n}(s)\sin(m\theta - nN_{\text{fp}}\phi) \tag{3.10}$$

$$\tag{3.11}$$

where N_{fp} is the number of toroidal field periods ($N_{\text{fp}}^{\text{LHD}} = 10$). Equations 3.9 and 3.10 define the R and Z grids in terms of flux surfaces s with poloidal angle θ. This allows for the equilibrium geometry to be interpolated onto the R-Z plane for each toroidal angle ϕ. An example of the interpolation is shown in Fig. 3.1. The plasma boundary is then defined as the $s = 1$ surface interpolated to cylindrical coordinates.

In addition to the equilibrium geometry, the vector field components B_R, B_Z, and $B_{\phi_{\text{cyl}}}$ must be interpolated from the covariant representation of the magnetic field

$$\boldsymbol{B} = B_s \nabla s + B_\theta \nabla \theta + B_\phi \nabla \phi. \tag{3.12}$$

The vector components of $\boldsymbol{B}$ are defined as

$$B_s(s,\theta,\phi) = \sum_{m,n} B_{s(m,n)}(s) \sin(m\theta - nN_{\text{fp}}\phi) \tag{3.13}$$

$$B_\theta(s,\theta,\phi) = \sum_{m,n} B_{\theta(m,n)}(s) \cos(m\theta - nN_{\text{fp}}\phi) \tag{3.14}$$

$$B_\phi(s,\theta,\phi) = \sum_{m,n} B_{\phi(m,n)}(s) \cos(m\theta - nN_{\text{fp}}\phi) \tag{3.15}$$

$$\tag{3.16}$$

While the toroidal angle variables ϕ and ϕ_{cyl} can be aligned so that $\phi = \phi_{\text{cyl}}$, the vector field components are not identical $B_\phi \neq B_{\phi_{\text{cyl}}}$. The transformation from VMEC field components to cylindrical field components is calculated using Eq. 3.12 as

$$B_R(s,\theta,\phi) = \left(\frac{\partial Z}{\partial \theta} B_s - \frac{\partial Z}{\partial s} B_\theta\right) B^* \tag{3.17}$$

$$B_Z(s,\theta,\phi) = \left(\frac{\partial R}{\partial s} B_\theta - \frac{\partial R}{\partial \theta} B_s\right) B^* \tag{3.18}$$

$$\begin{aligned} B_{\phi_{\text{cyl}}}(s,\theta,\phi) = \frac{1}{R}\Bigg[\Bigg(\Bigg(&\left(\frac{\partial R}{\partial \theta}\frac{\partial Z}{\partial \phi} - \frac{\partial R}{\partial \phi}\frac{\partial Z}{\partial \theta}\right) B_s \\ &+ \left(\frac{\partial R}{\partial \phi}\frac{\partial Z}{\partial s} - \frac{\partial R}{\partial s}\frac{\partial Z}{\partial \phi}\right) B_\theta\Bigg) B^* + B_\phi\Bigg] \end{aligned} \tag{3.19}$$

$$B^*(s,\theta,\phi) = \left(\frac{\partial R}{\partial s}\frac{\partial Z}{\partial \theta} - \frac{\partial R}{\partial \theta}\frac{\partial Z}{\partial s}\right)^{-1} \tag{3.20}$$

$$\tag{3.21}$$

The implementation of the VMEC field transformation in python preprocessing scripts for FIDASIM can be found in appendix C.

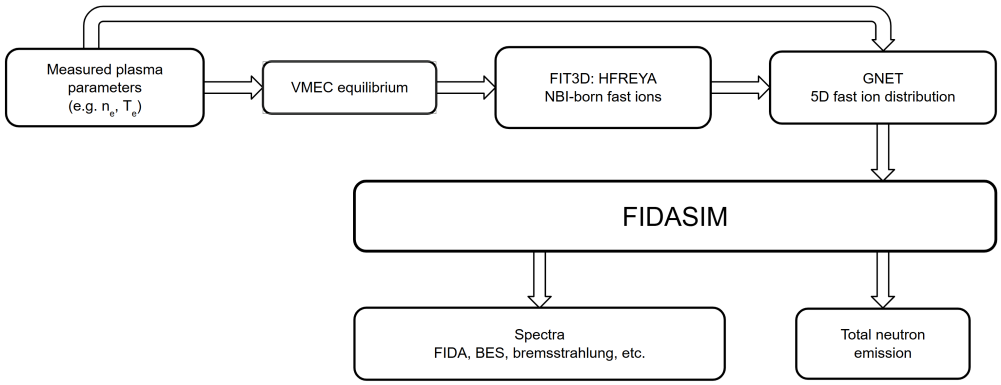

Figure 3.2: Flowchart for FIDASIM using a GNET distribution.

3.3 Full 5-D neoclassical distribution

The physics encapsulated by the fast-ion distribution model determines the level of agreement between the measured and simulated signals. Previous fast ion studies in LHD [35, 38] used fast ion distributions calculated by the 5-D global neoclassical transport code GNET [39]. GNET is also used for fast ion distributions used in Ch. 4. The workflow for FIDASIM with GNET is shown in Fig. 3.2. Plasma parameters are measured during the experiment and passed to VMEC to construct the equilibrium. The equilibrium and plasma profiles are then used with the HFREYA code to calculate the fast ion birth markers due to NBI. HFREYA is part of the FIT3D code suite for fast ion modeling in LHD [40]. Fast ion birth markers are input to GNET which solves the linearized drift kinetic equation for the 5D fast ion distribution as a steady state distribution [41]. The fast ion distribution, along with the thermal plasma profiles and equilibrium are input to FIDASIM which calculates the synthetic spectral features. While GNET provides a robust physical model for neoclassical behavior of fast ions, it is computationally expensive and reserved for select cases.

3.4 Reduced model distribution

For analysis presented in Ch. 5, a reduced model is necessary due to the volume of cases. The reduced model, herein referred to as the Goldston model or Goldston distribution, uses a steady-state solution to the collisional Fokker-Planck equation for the velocity-space distribution [42]. The full Fokker-Planck equation is

$$\frac{\partial f}{\partial t}(v,p,t) = \underbrace{S(v,p,t)}_{\text{fast-ion source}} \tag{3.22}$$

$$+ \underbrace{\frac{1}{\tau_{se}}\frac{\partial}{\partial v}[(v^3+v_c^3)f]}_{\text{election and ion friction}} + \underbrace{\frac{1}{2\tau_{se}}\frac{\partial}{\partial v}\left[\frac{v_e^2 m_e}{m_f}+\frac{v_c v_i^2 m_i}{v^3 m_f}\right]\frac{\partial f}{\partial v}}_{\text{energy diffusion}} \tag{3.23}$$

$$+ \underbrace{\frac{1}{2\tau_{se}}\frac{m_i}{m_f}\frac{Z_{eff}}{[Z]}\frac{v_c^3}{v^3}\frac{\partial}{\partial p}\left[(1-p^2)\frac{\partial f}{\partial p}\right]}_{\text{pitch-angle scattering}} \tag{3.24}$$

$$- \underbrace{\frac{eE_{\|}}{m_f}\left[p\frac{\partial f}{\partial v}+\frac{(1-p^2)}{v}\frac{\partial f}{\partial p}\right]}_{\text{electric field}} - \underbrace{\frac{f}{\tau_{cx}}}_{\text{charge exchange}} \tag{3.25}$$

where p is parallel pitch $v_{||}/v$. Assuming that the Coulomb collision time τ_S is much smaller than the orbit bounce time τ_b, a first-order solution $f^0(v,p,t)$ can be expanded in Legendre polynomials $P_\ell(p)$ with the index ℓ so $f^0(v,p,t) = \sum_\ell a_\ell P_\ell(p)$. The fast ion source term $S(v,p,t)$ can also be expanded in Legendre polynomials $S(v,p,t) = \sum_\ell S_\ell(t)\delta(v-v_0)P_\ell(p)$ with the source components S_ℓ defined using the completeness of the set of Legendre polynomials

$$S_\ell(t) = \frac{2\ell+1}{2}\int_{-1}^{1} S(v_0,p,t)P_\ell(p)\,dp \tag{3.26}$$

where v_0 is the fast ion birth velocity. The Fokker-Planck equation is then reduced in terms of a_ℓ

$$\frac{\partial a_\ell}{\partial t} = -\alpha_\ell a_\ell + \beta\frac{\partial a_\ell}{\partial v} + \gamma\frac{\partial^2 a_\ell}{\partial v^2} + S_\ell(v_0, p, t)\delta(v - v_0)/(4\pi v_o^2) \tag{3.27}$$

The terms α_ℓ, β, and γ correspond to the various velocity transport effects

$$\alpha_\ell = \underbrace{\frac{1}{\tau_{cx}}}_{\text{charge exchange}} + \underbrace{\frac{n_e}{2v_0^3}\ell(\ell+1)\langle Z\rangle\Gamma}_{\text{pitch-angle scattering}} - \underbrace{1.99\times10^{-20}\frac{n_e A_\mathrm{f}}{T_e^{3/2}}\Gamma}_{\text{velocity space compression}} \tag{3.28}$$

$$\beta = \underbrace{(6.62\times10^{-21}v_0 n_e A_\mathrm{f}/T_e^{3/2})\Gamma}_{\text{stationary electron distribution}} + \underbrace{\frac{[Z]}{v_0^2}\frac{A_\mathrm{f}}{\bar{A}_i}n_e\Gamma}_{\text{ions}} \pm \underbrace{\frac{9.58\times10^{11}}{A_\mathrm{f}}|\vec{E}|Z_\mathrm{f}\left(1-\frac{Z_\mathrm{f}}{Z_{eff}}\right)}_{\text{E-field and drifting electron distribution}} \tag{3.29}$$

$$\gamma = \underbrace{6.34\times10^{-9}\frac{n_e}{T_e^{1/2}}\Gamma}_{\text{electrons}} + \underbrace{9.58\times10^{11}\frac{n_e T_i}{v_0^3}\frac{[Z]}{\bar{A}_i}\Gamma}_{\text{ions}} \tag{3.30}$$

with temperatures in eV and densities in cm^{-3}. The subscript f corresponds to fast ions. Electron and ion coulomb logarithms are represented by $\ln\Lambda_e$ and $\ln\Lambda_i$. Other terms in eq. 3.28-3.30 are defined as

$$\Gamma = 2.39\times10^{11}\left(\frac{Z_b}{A_b}\right)^2\ln\Lambda_e$$

$$\langle Z\rangle = \frac{\sum n_i Z_i^2\ln\Lambda_i}{n_e\ln\Lambda_e}$$

$$[Z] = \frac{\bar{A}_i}{n_e}\sum n_j\frac{Z_j^2\ln\Lambda_j}{A_j\ln\Lambda_e}$$

$$\bar{A}_i = \frac{\sum n_i A_i}{\sum n_i}$$

The steady-state solution for a_ℓ is then

$$a_\ell(\Delta, \infty) = \frac{S_\ell/(4\pi v_0^2)}{\beta D_\ell} \exp\left[-\frac{\beta\Delta}{2\gamma}(1 + \text{sign}(\Delta) D_\ell)\right] \tag{3.31}$$

$$D_\ell = \sqrt{1 + \frac{4\alpha_\ell \gamma}{\beta^2}} \tag{3.32}$$

$$\Delta = v - v_0 \tag{3.33}$$

A full implementation of the steady-state Goldston solution is provided in appendix D.

The spatial distribution is determined by the heating beam deposition profile calculated by a preliminary FIDASIM run. The full FIDASIM workflow for this reduced model, shown in Fig. 3.3, is as follows:

1. a 3-D equilibrium and flux coordinate mapping is calculated with VMEC++,
2. the equilibrium and measured plasma parameters are input to FIDASIM and run with an empty distribution,
3. the resultant fast-ion birth profile in 3-D cylindrical coordinates is mapped to ρ,
4. a 2-D velocity-space distribution is calculated using the Goldston model for each flux surface in the radial birth profile,
5. the 3-D (Energy, Pitch, ρ) fast-ion distribution is mapped to 5-D (Energy, Pitch, R, Z, ϕ)
6. FIDASIM is run with the new distribution.

A normalization factor for the Goldston distribution will be further discussed in section 5.2.2. The Goldston model incorporates a term for charge-exchange losses of fast ions due to thermal neutrals. Due to a lack of measurements of the background neutral density, the charge-exchange loss term is not utilized for this study. Additional electric field effects in

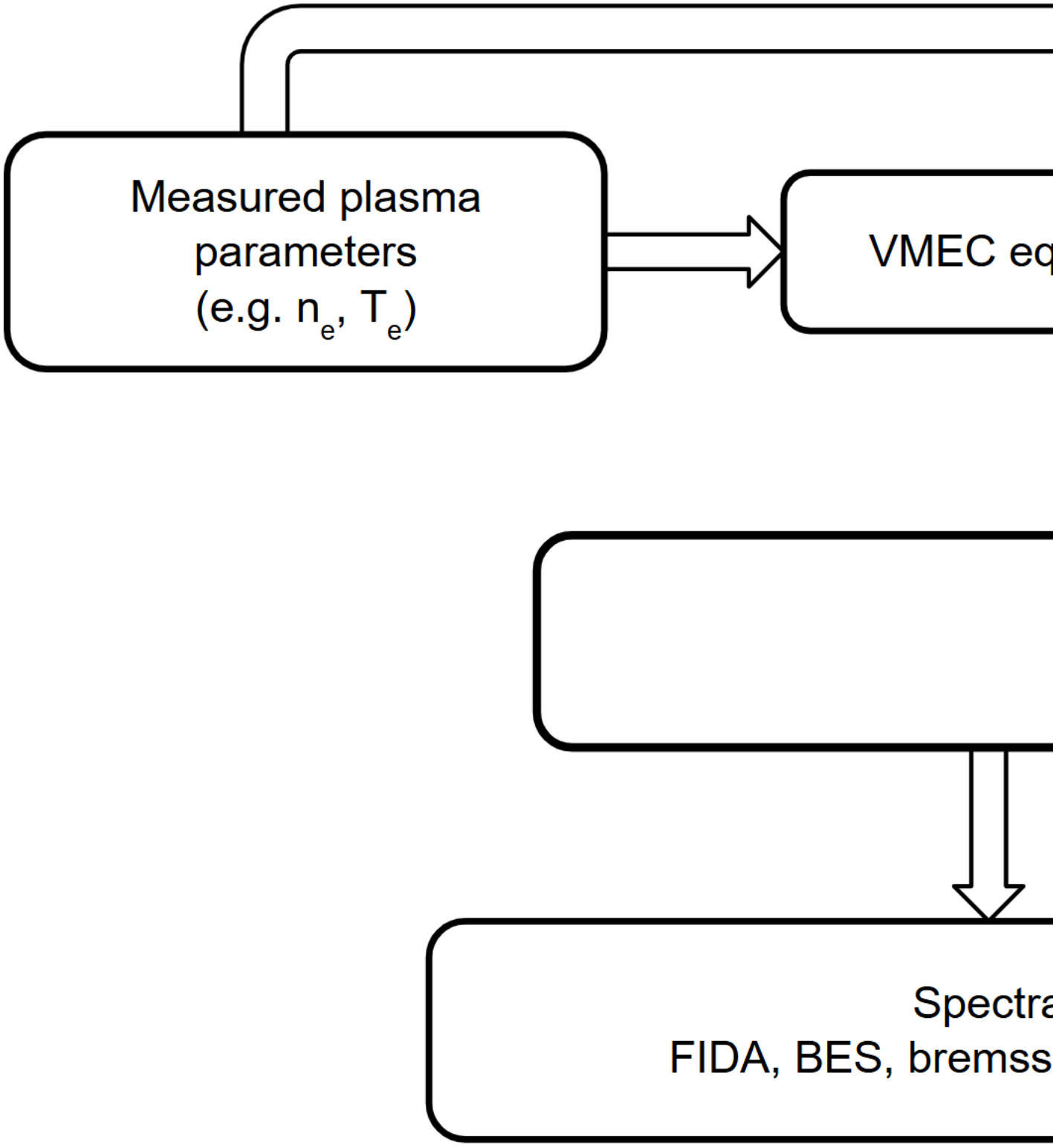

Figure 3.3: Flowchart for FIDASIM using a Goldston distribution.

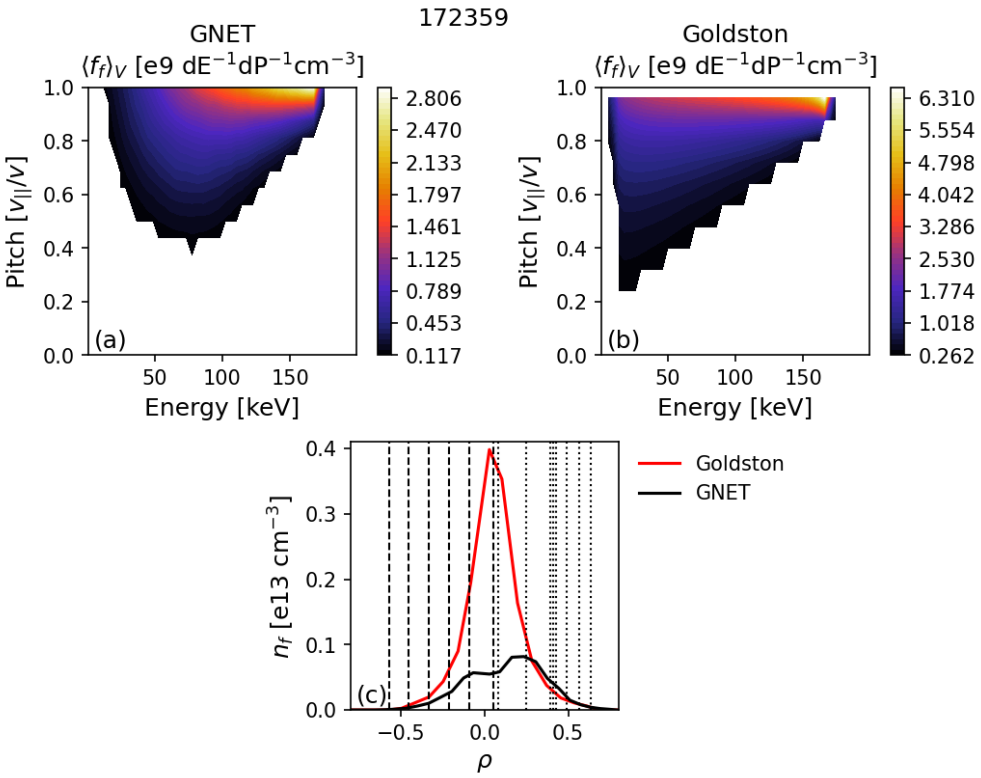

Figure 3.4: (a) GNET distribution, (b) Goldston distribution, and (c) fast ion densities for discharge 172359. Vertical dashed lines in (c) correspond to 6-O LOS channels while dotted lines correspond to 7-O LOS channels.

eq. 3.29 are negligible and ignored in the present study. The Goldston distribution is a classic slowing-down distribution and does not include neoclassical effects or instability effects; accordingly, it can be viewed as the distribution function of an ideal magnetic confinement device. Deviation of measurements from FIDASIM with a Goldston distribution can be attributed to neoclassical effects or instabilities. Figure 3.4 shows a typical volume-average GNET distribution calculated for a $R_{ax} = 3.6$ m case with a Goldston distribution calculated for the same case.

Chapter 4

Measurements near the injected neutral energy

This chapter details the evaluation of the 7-O port (red arrows Fig.1.3(a)) FICXS sightline (line-of-sight or LOS), a new diagnostic LOS that was installed in LHD to view fast ions near the high injection energy of NB3. The design of the new LOS was initially evaluated in a previous study [43]. This chapter focuses on the use of the new LOS in experiments, confirming the predictions from the previous study.

Experiments are conducted in LHD using NB3 for heating and for active charge-exchange diagnostics. In order to use NB3 as a heating and diagnostic beam the injected power was modulated with an 80% duty cycle. In addition to neutral beam injection (NBI), 1 MW electron cyclotron heating (ECH) is used to heat the plasma. Time traces for a favorable LHD discharge are shown in Fig. 4.1 for the injected NBI and ECH power, line-averaged electron density, electron and ion temperatures, and magnetic fluctuation power spectral density. NB4 is modulated with a 20% duty cycle to measure signal with the original 6-O port LOS (blue arrows Fig.1.3(a)) for comparison. NB3 (NB4) injection energy is 166 keV (56 keV)

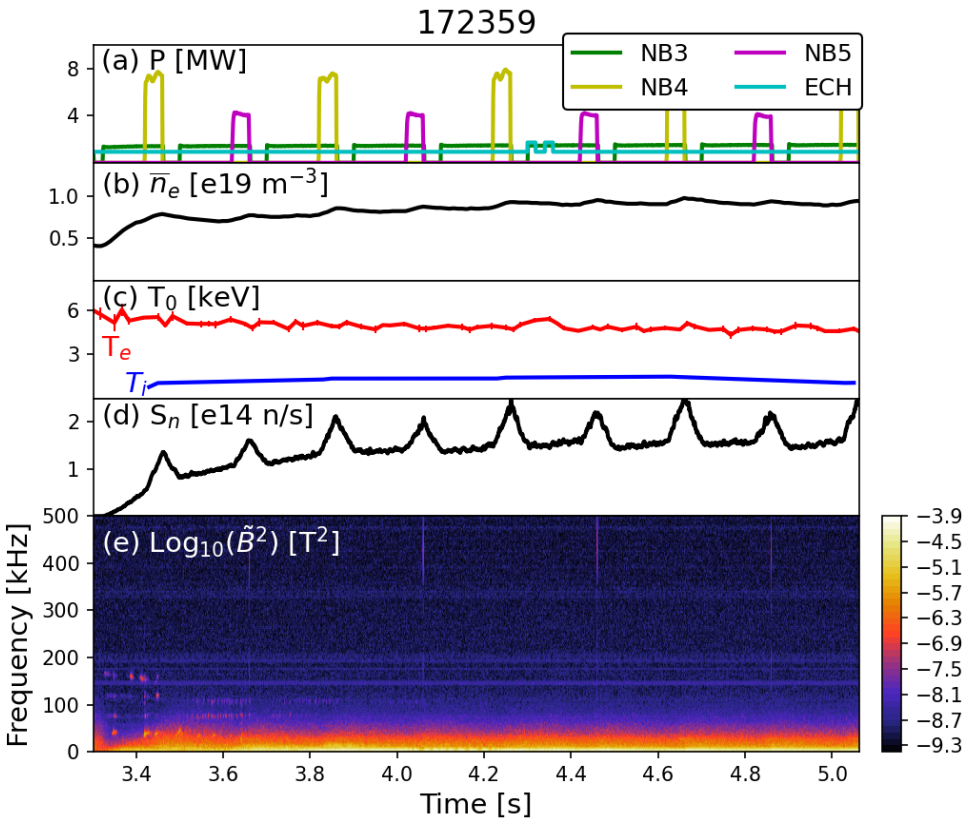

Figure 4.1: Time traces for discharge 172359 showing (a) heating power, (b) line-average electron density, (c) core electron and ion temperature, (d) global neutron emission rate, and (e) power spectral density of magnetic fluctuations.

and injection power is 1.5 MW (3.5 MW). The experiment used a magnetic configuration with a counterclockwise field B = 2.75 T and magnetic axis at $R_{ax} = 3.6$ m. The plasma had a central electron temperature of $T_{e0} = 5$ keV, central ion temperature of $T_{i0} = 1.4$ keV, a volume-averaged electron density of $\tilde{n}_e = 0.8 \times 10^{19}\ m^{-3}$, and a counterclockwise plasma current of $I = 5$ kA.

4.1 New sightline concept

The charge-exchange cross section for FIDA emission is dependent on the relative energy between the fast ions and the injected neutrals; this dependency peaks at around 30 keV/amu

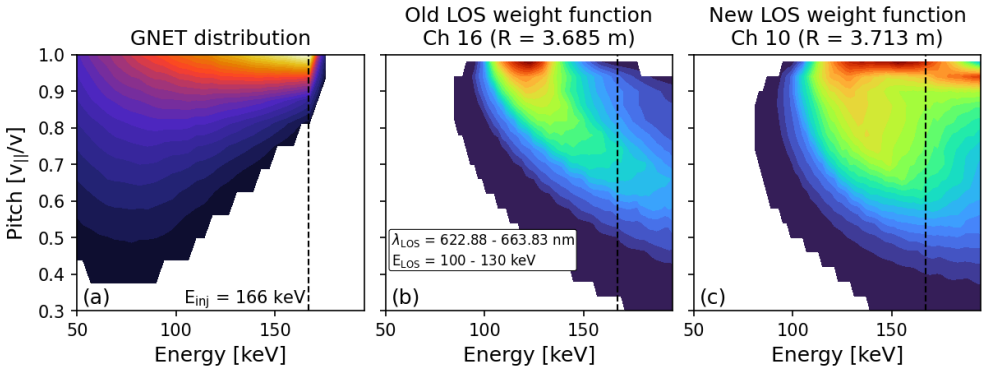

Figure 4.2: (a) GNET distribution function, (b) old LOS weight function, and (c) new LOS weight function for discharge 172359

for hydrogenic ions [20]. The original FICXS sightline in LHD uses the 6-O port with NB4 as the active beam. A large relative angle between the 6-O LOS with its active beam means that measured signals are limited to relatively low-energy fast ions. The new LOS uses NB3 as the active beam with a much smaller relative angle (red arrows Fig.1.3(a)). A small angle means that the relative energy is largely dependent on the relative magnitudes of the injected neutral energy and fast ion energy. As a result, the FICXS diagnostic with the new LOS is sensitive to fast ions with energies close to the high injected energies from the diagnostic beam. The old 6-O and new 7-O LOS are referred to as low-energy and high-energy LOS, respectively.

The effectiveness of the high-energy view at diagnosing high-energy fast ions was predicted in a previous study [43] using FIDASIM. Figure 4.2 shows the GNET distribution for FIDASIM analysis of 172359 along with weight functions for both LOS. Weight functions are integrated over $\lambda_{\mathrm{LOS}} = 622.88$ - 663.83 nm which corresponds to $E_{\mathrm{LOS}} = 100$ - 130 keV. The low-energy weight functions shows that the diagnostic sensitivity is concentrated around 120 keV. On the other hand, the high-energy weight function extends from 120 keV to the NB3 injection energy of 166 keV for a fast-ion pitch just below 1. This would indicate that the high-energy in the wavelength integration range is sensitive to strongly passing fast ions near their birth energy.

4.2 Measured data and simulation results

The FIDA emission observed in 172359 shows signals that are Doppler-shifted to the expected wavelength for high-energy fast ions. Background subtraction is used to construct the net signal using the difference between the beam-on time t = 3.98 s and the beam-off time t = 3.88 s. Figure 4.3 shows the time-averaged beam-on, beam-off, and net signal normalized to the background bremsstrahlung for the low-energy (a) and high-energy (b) views. The signals were initially normalized to the beam emission spectroscopy (BES) feature. However, the high intensity BES signals were found to be truncated above a certain count number making it unsuitable for normalization. The net signal in 4.3(b) shows the NNBI BES feature around 665 nm, as expected for a 166 keV injection energy, and the FIDA emission feature between 660 nm and 664 nm. The peak in the FIDA emission occurs at 662.2 nm which corresponds to fast ions with an energy component of 81 keV along the sightline. A similar analysis of the low-energy view found that the FIDA peak appears at 661.8nm or 71 keV along the sightline. The high-energy view has a greater Doppler-shift of the FIDA peak and a reduced signal for lower energies indicating that the high-energy view can isolate fast ions with greater energies.

The behavior of the net signal measured by the high-energy view is validated against FIDASIM under the same conditions as the experimental case. The comparison of the synthetic signals are shown in Figure 4.3(c) for the low-energy view and 4.3(d) for the high-energy view. Instrumental broadening was applied to the FIDASIM signal using empirically determined values from matching the OV impurity lines. The shape of the synthetic FIDA features have good agreement with the measured signal between 660 nm and 663 nm, while the normalized magnitude for both views is overestimated by FIDASIM. This discrepancy can be attributed to the loss of fast ions in the experiment due to charge-exchange with cold neutrals, among other considerations which are not accounted for in the simulation.

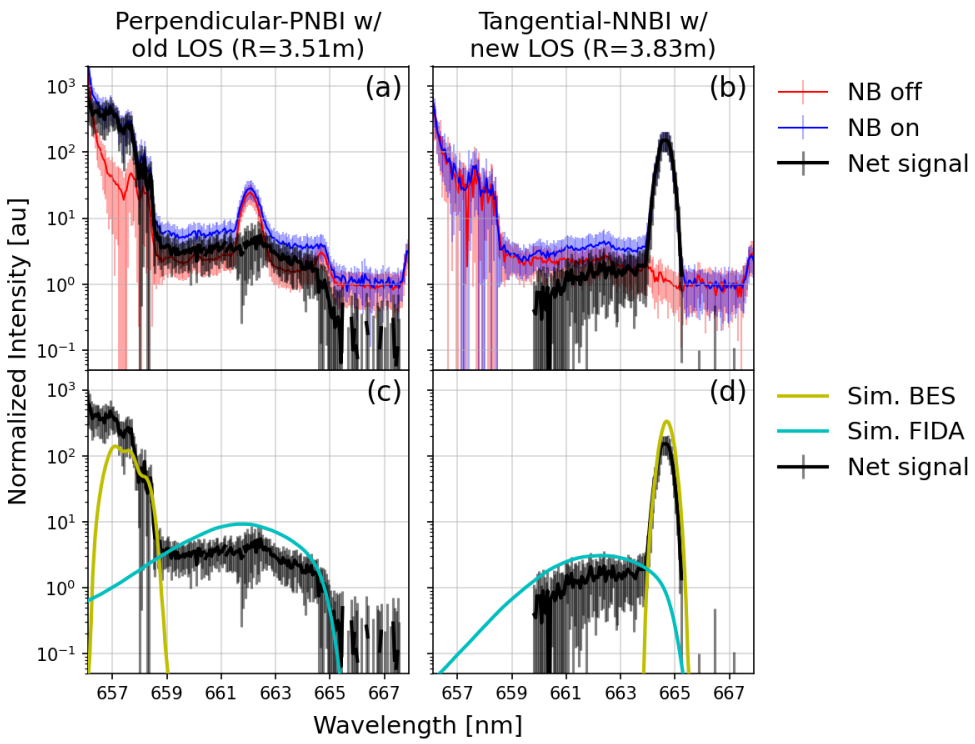

Figure 4.3: Comparison of measured FIDA density between (a) old LOS and (b) new LOS along with (c, d) comparison of measurements with FIDASIM.

The parametric dependencies of the FIDA feature are in qualitative agreement with theory. Theoretically, in addition to the cross-section dependence, the FIDA signal is proportional to the product of the injected-neutral and fast-ion densities, $n_{inj}n_f$. Increasing power of the diagnostic beam tends to increase n_{inj} and increasing power of the heating beam tends to increase n_f. Due to the hybrid diagnostic-heating NB3 beam pattern, the injected diagnostic beam power contributes to both the fast-ion density and injected neutral density. Figure 4.4(a) shows that, as expected, the signals for both the low- and high-energy views tend to increase with diagnostic beam power. Owing to the higher injected power of the PNBI compared to NNBI, the low-energy view has signals that are about twice as large as the high-energy view. Figure 4.4(b) shows that both the old and the new signals tend to decrease with increasing density $\bar{n}_e$. This also is expected [35, 44], since increasing density tends to decrease beam penetration (reducing n_{inj}) and increasing density lowers the slowing-down time (reducing n_f).

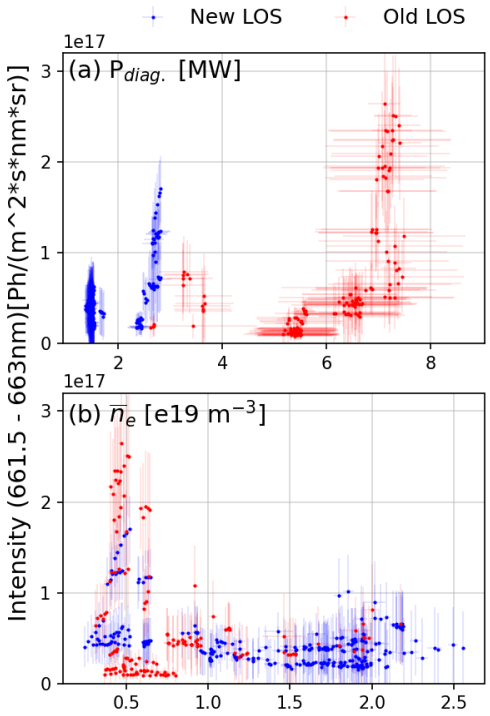

Figure 4.4: Parametric dependency of new LOS on (a) diagnostic beam heating power and (b) line-averaged electron density. Ordinates for both subplots are FIDA intensity integrated over 661.5 - 663 nm. Abscissa for (a) is diagnostic beam power and (b) is line-averaged electron density. Data points for the new LOS are in blue. Data points for the old LOS are in red. Error bars show one standard deviation.

Experimental results and FIDASIM calculations confirm predictions from *Muscatello, et al.* [43] that FIDA sightlines nearly tangential to the active beamline can be used to measure high-energy fast ions. The previous study used an ideal geometry for the high-energy view with a 180 keV NNBI heated plasma. This results in a predicted FIDA peak corresponding to 662.5 nm or fast ions with energies of 90 keV along the sightline. The difference in energy between [43] and the current experimental results can be attributed to using a lower injection energy (166 keV) and a deviation of the installed sightline from the ideal geometry. Despite this, the high-energy view on LHD can still isolate signals from fast ions with over 10 keV higher energies than the low-energy view. Based on this method, FIDA emission can be measured for fast ions above 100 keV in NBI-heated plasmas using higher injection energies.

Chapter 5

Quiet LHD plasmas

This chapter details a study in LHD plasmas with little to no magnetohydrodynamic (MHD) instabilities. The two primary motivations of this study are to (a) observe changes in neoclassical confinement of fast ions due to changes in the magnetic configuration and (b) characterize the parametric dependencies of the FICXS diagnostic system. Bulk plasma performance is known to improve in LHD when shifting the major radius position of the magnetic axis (R_{ax}) from 3.75 m to 3.6 m [45]. This is due to the increased amplitude of sideband helical modes $B_{m\neq1,10}$ which aligns B_{min} along a field line and reduces neoclassical transport [46]. This is similar to the σ-optimized configuration described by *Mynick et al.* [47]. Neoclassical transport theory predicts a minimum of the diffusion coefficient at R_{ax} = 3.53 m, known as the neoclassically-optimized configuration [48]. Due to operational limitations, the present study can only achieve a minimum R_{ax} of 3.55 m. Despite the constraint, a range of R_{ax} = 3.55-3.7 m is sufficient to study neoclassical effects on fast ions.

Various studies have been conducted to understand neoclassical effects on fast ions in LHD. Modeling of trapped fast ions shows marginally improved confinement at R_{ax} = 3.6 m [49]. Fast neutral measurements show that transport of these fast ions is dominated by neoclassical

effects [38]. Neutral profile measurements and triton burn-up ratio were found to increase with smaller R_{ax} [50]. Global neutron emission measurements were also found to increase with smaller R_{ax} [25]. Numerical studies have found that the R_{ax} = 3.6 m configuration is comparable to optimized reactor designs and quasisymmetric equilibria [51, 52]. In the present study, three magnetic axis positions are considered: R_{ax} = 3.55, 3.6, and 3.7 m. In addition to varying R_{ax}, selected samples cover a range of electron density, temperature, and NBI heating power to understand the parametric dependencies of the FICXS diagnostic. Toroidal field B_t is counter-clockwise (CCW) for all configurations with field strength set to keep a constant value of R_{ax} *B_t = 9.9 m T. Fast ions are observed using FICXS as the primary diagnostic with VNC as a secondary diagnostic. The fast ion distribution is inferred using FIDASIM with the reduced model Goldston distribution. The Goldston model does not include neoclassical effects that contribute to improved confinement in the inward shifted configurations. Differences, or lack thereof, between measurements and simulations across R_{ax} are attributed to the improvement or lack of improvement in neoclassical confinement with an inward-shifted axis. Confinement effects observed by diagnostics are further informed by comparisons of equilibrium calculations and fast ion orbit simulations.

5.1 Selection process

Experiments were conducted over multiple campaigns in order to select discharges where strong MHD activity is not observed. Discharges were first filtered to select cases with CCW B_t that used only one source of NB1, NB2, or NB3 to populate the passing fast ion orbits. Heating with only one tangentially-injected beam source is preferred in order to minimize MHD activity. While the focus is on non-ECH heated cases, a few discharges were selected with ECH heating for comparison. A measure of relative MHD-quiescence is then used to select cases with little to no impact from instabilities. This section details the selection

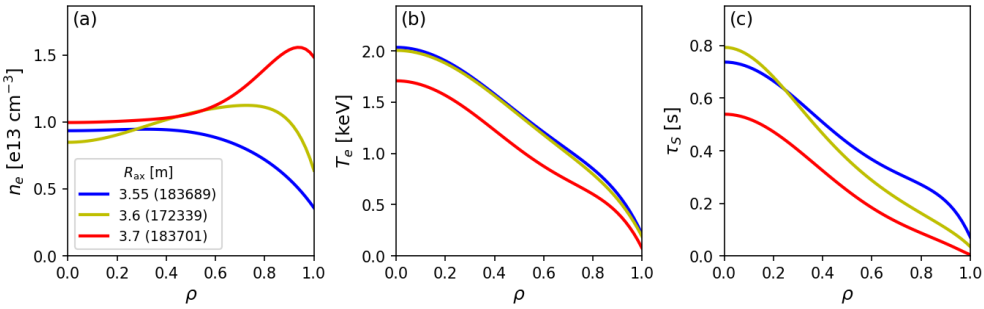

Figure 5.1: Typical profiles for electron (a) density, (b) temperature, and (c) Spitzer slowing-down time for three configurations vs normalized minor radius.

process for single source heating and for relative MHD-quiescence. A full listed of selected cases used in the analysis is listed in appendix E.

5.1.1 Plasma profiles and heating beam configurations

Data presented in the following analysis comes from a larger dataset composed of multiple experiments in LHD. While the larger dataset includes both hydrogen and deuterium plasmas with NBI and ECH heating, the present study will focus on deuterium beam and plasmas. A smaller subset includes ECH heated cases but the majority of analysis will focus on only NBI heated cases. Electron densities range from low (0.5×10^{19} m^{-3}) to moderate (2.0×10^{19} m^{-3}) and temperatures in non-ECH cases range 1-3 keV (4-8 keV for ECH cases). Typical profiles for three magnetic configurations are shown in Fig. 5.1. Observed density profiles tend to peak on-axis in the most inward shifted configuration R_{ax} = 3.55 m and become more hollow at larger R_{ax}. Temperature profiles are peaked on-axis for all configurations. Average rotational transform $\iota/2\pi$ and effective helical ripple $\varepsilon_{\rm eff}^{3/2}$ values are shown in Fig. 5.2. Average values are taken from selected discharges and timestamps for each R_{ax} configuration under consideration in the present study. Lower values of $\varepsilon_{\rm eff}^{3/2}$ correspond to improved neoclassical confinement in the $1/\nu$ transport regime [53]. The decrease in $\varepsilon_{\rm eff}^{3/2}$

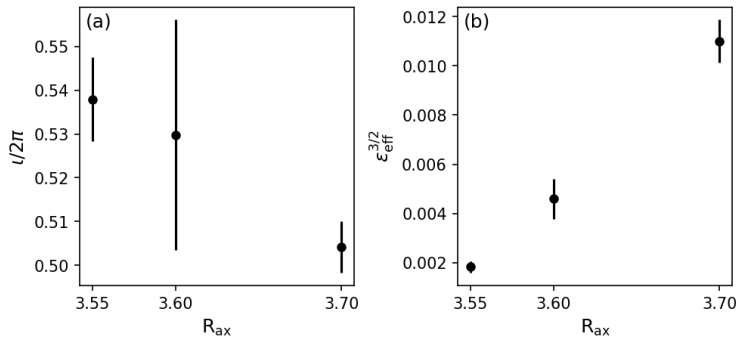

Figure 5.2: (a) Rotational transform $\iota/2\pi$ and (b) effective helical ripple $\varepsilon_{\text{eff}}^{3/2}$ values at the mid-radius ($\sqrt{\psi/\psi_{\text{edge}}} = 0.5$) vs R_{ax}. Error bars indicate one standard deviation.

with smaller R_{ax} means that we should expect increased neoclassical confinement in the inward-shifted configurations.

5.1.2 Quantitative selection of MHD-quiescent discharges

A measure of relative MHD-quiescence is used to select cases with little to no impact from instabilities. The selection process is shown in Fig. 5.3. Magnetic fluctuations are observed by a toroidal array of magnetic probes with a sampling rate of 1 MHz [54]. For each diagnostic beam cycle in the CCW-B_t one-source NBI cases, a power spectrum (power spectral density or PSD) with a 8.192 ms sliding window is calculated. The power spectrum $P_{xx}(t, f)$ is calculated using short-time Fourier-transforms of time-dependent magnetic fluctuation data $\tilde{B}(t)$ as

$$P_{xx}(t, f) = P_x(t, f)P_x^*(t, f) \tag{5.1}$$

$$P_x(t, f) = \int_{\mathbb{R}} \tilde{B}_x(t')\, w^*(t' - t)\, e^{-i2\pi f t'}\, dt' \tag{5.2}$$

where the superscript * indicates a complex conjugate, $w(\tau)$ is a sliding Hann window, and the subscript x indicates a magnetic probe. The cross-power spectral density is then defined as $P_{xy} : x \neq y$. Magnitude squared-coherence C_{xy}, defined using the cross-power spectral

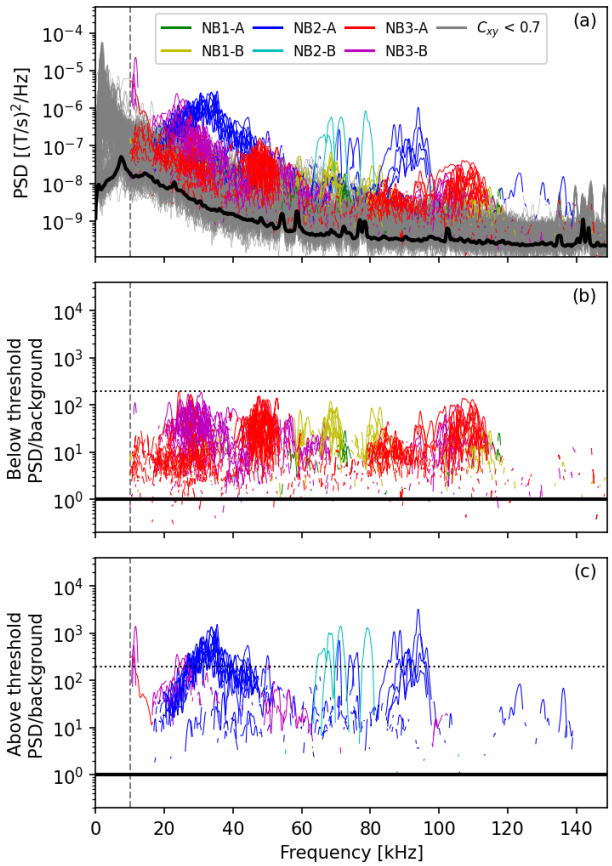

Figure 5.3: (a) Power spectral densities (PSD) for the filtered cases (single source NB1, NB2, or NB3 with CCW B_t). Signals with coherence above 0.7 are labeled by color corresponding to the heating source. Gray lines represent regions where the coherence is below 0.7. The solid black line represents the background signal calculated from the average of the lower 25th percentile. Vertical dashed line at 10 kHz represents the lower cutoff, below which the magnetic fluctuations are not used in the selection process. (b) PSD/background for cases where max(PSD/background) $<$ 2e2 and are labeled as MHD-quiescent. (c) PSD/background for cases that fail to meet the condition and are labeled as MHD-active. Solid black lines in (b, c) represent the background signal at PSD/background = 1. Dotted horizontal lines in (b, c) represent the selection condition at PSD/background = 2e2.

density

$$C_{xy}(t,f) = \frac{|P_{xy}(t,f)|^2}{P_{xx}(t,f)\,P_{yy}(t,f)} \tag{5.3}$$

is used to select coherent peaks between two different probes using the condition $C_{xy} > 0.7$. A background signal is constructed from the average of the lower 25th percentile in every frequency bin, shown in Fig. 5.3(a). Relatively MHD-quiescent cases are labeled with the condition $\mathrm{Max}(\mathrm{PSD_{coh}}/\mathrm{background}) < 2e2$. Cases meeting this condition are shown in Fig. 5.3(b) and cases that fail to meet this condition are shown in Fig. 5.3(c). All cases heated by NB2 are found to surpass the threshold so only NB1 and NB3 cases are selected for further analysis.

5.1.3 Shared radial coordinate for FICXS and VNC

Aside from changing the FICXS channel configuration (table 2.1), the sightline positions do not change during the experiments as $\mathrm{R_{ax}}$ changes so they do not align with the same flux surfaces. For effective analysis of the FICXS and VNC profiles, the coordinates are mapped to a common flux coordinate. Figure 5.4 shows FICXS and VNC sightlines projected onto the R-Z plane and overlaid on flux surfaces for three $\mathrm{R_{ax}}$ configurations. A mapping between real space and flux coordinates in an LHD plasma is provided by the Thomson system (TSMAP) which maps to the normalized radial coordinate r_{eff}/a_{99} [55]. TSMAP channels and FICXS channels map to horizontally-elongated sections of LHD so the FICXS profile can be interpolated from R to r_{eff}/a_{99}. This allow for a direct comparison of FICXS profiles between different $\mathrm{R_{ax}}$ cases by comparing channels with similar r_{eff}/a_{99} values. However, the VNC channels intersect a vertically-elongated section which does not align with the R to r_{eff}/a_{99} mapping. A map between the VNC channel locations in real-space and flux coordinates is calculated using VMEC [56]. The workflow in the present study employs VMEC++

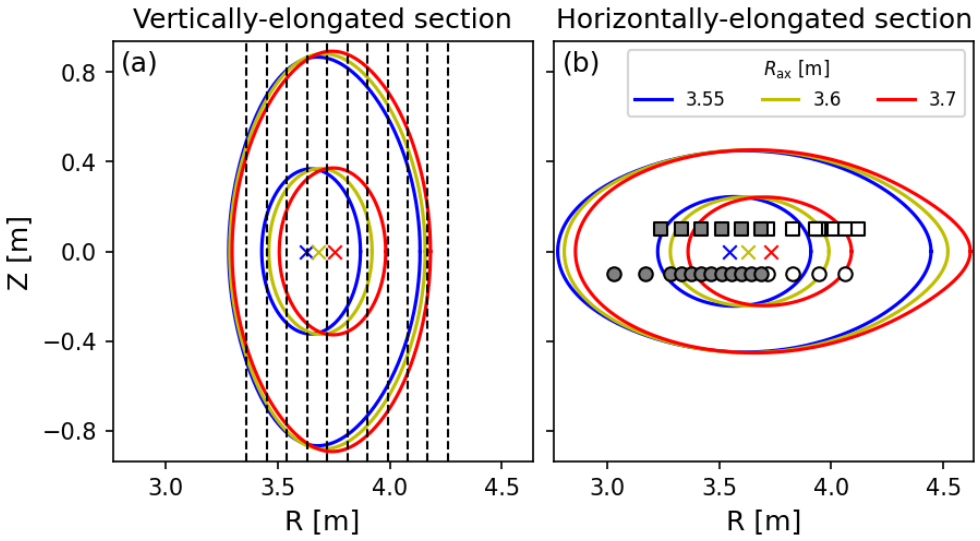

Figure 5.4: Flux surfaces for $\rho = 0.5$ and $\rho = 1.0$ calculated by VMEC for the (a) vertically-elongated and (b) horizontally elongated sections. Magnetic axes are marked by x's. Vertical dashed lines in (a) indicate the VNC sightlines. Markers in (b) indicate the FICXS sightline intersections with the poloidal plane for PNBFIDA (circles) and NNBFIDA (squares) fiber configurations. Closed and open markers indicate the 6-O and 7-O sightlines, respectively. Vertical displacement of the markers is exaggerated for clarity. Shot numbers for each configuration are listed in Fig. 5.5.

[57], a C++ based version of VMEC. A comparison of the TSMAP $r_{\rm eff}/a_{99}$ coordinate with the VMEC flux coordinate $\sqrt{\psi/\psi_{\rm edge}}$ is listed in table 5.1 with values interpolated from the position of channels for a standard $R_{\rm ax} = 3.6$ m case with the NNBFIDA configuration. Good agreement between the two systems is expected due to the use of original Fortran-based VMEC in the TSMAP workflow. Differences of 10^{-3} are attributed to slight differences in the preparation of input files for the two versions of VMEC and is considered acceptable for the comparison of FICXS to VNC. For these purposes, $r_{\rm eff}/a_{99}$ and $\sqrt{\psi/\psi_{\rm edge}}$ are treated as effectively identical. The normalized radial coordinate ρ is defined as $\rho = \sqrt{\psi/\psi_{\rm edge}} = r_{\rm eff}/a_{99}$ with negative values of ρ used for the inboard side of the poloidal plane. It should be noted that the magnetic axis in a finite-β plasma has a displacement that is dependent on the toroidal angle and torsion that is inversely proportional to the vacuum $\rm R_{ax}$ configuration as shown in Fig. 5.5.

	NNBFIDA (172339)			
Ch	View Port	R [m]	r_{eff}/a_{99}	$\sqrt{\psi/\psi_{\text{edge}}}$
1	7	3.943	0.443	0.437
2	7	3.943	0.443	0.437
3	7	4.120	0.651	0.650
4	7	4.061	0.585	0.582
5	7	4.002	0.516	0.511
6	7	3.955	0.458	0.452
7	7	3.943	0.443	0.437
8	7	3.931	0.428	0.422
9	7	3.829	0.294	0.284
10	7	3.713	0.134	0.121
11	6	3.237	-0.541	-0.540
12	6	3.329	-0.412	-0.409
13	6	3.419	-0.278	-0.274
14	6	3.509	-0.146	-0.140
15	6	3.597	-0.017	-0.009
16	6	3.685	0.117	0.118

Table 5.1: Comparison of flux coordinates for the Thomson system (r_{eff}/a_{99}) and for VMEC ($\sqrt{\psi/\psi_{\text{edge}}}$). Diagnostic channels are listed with the associated view port and the radial location of the intersection with the diagnostic beam. Sightlines are grouped and labeled according to their view ports (6-O LOS and 7-O LOS).

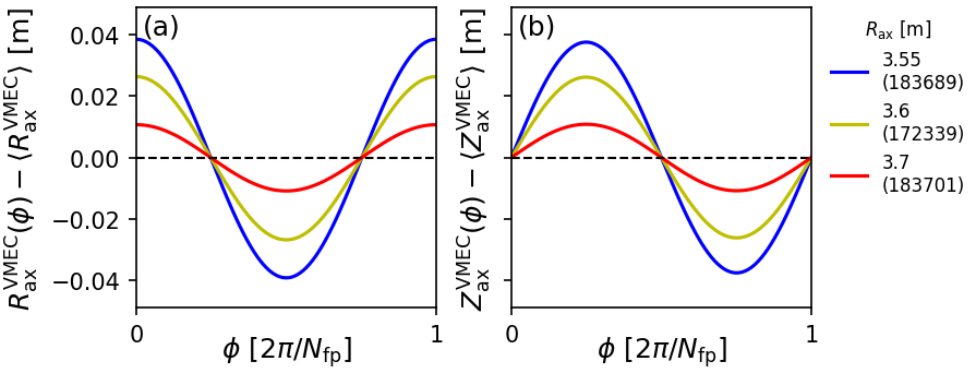

Figure 5.5: (a) Radial and (b) vertical displacement of the magnetic axis vs toroidal angle over one field period calculated by VMEC. Displacements are with respect to the average magnetic axis position over one field period. Curves are labeled by their vacuum R_{ax} configuration.

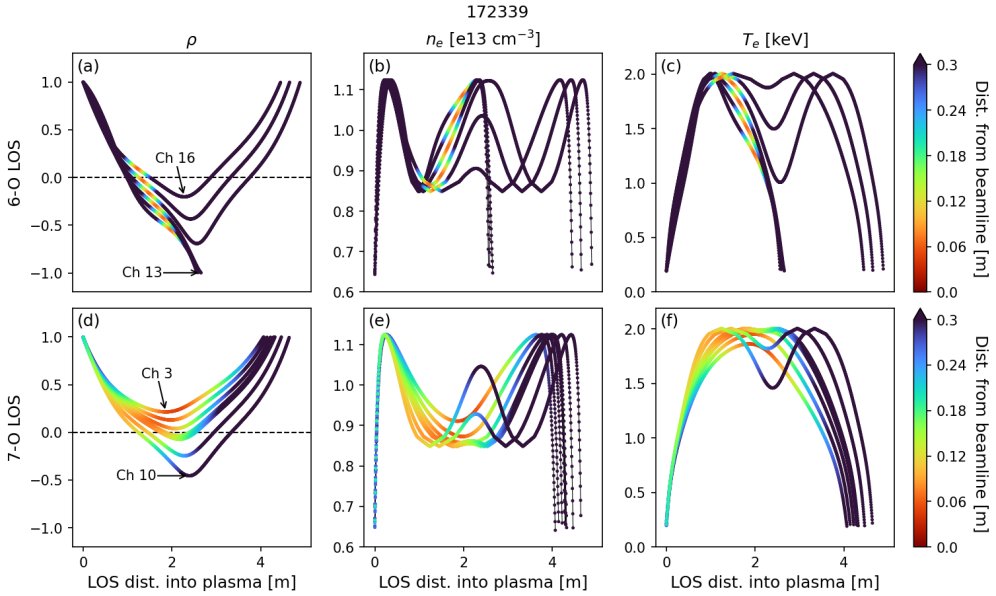

Figure 5.6: Parameters along 6-O LOS (top row) and 7-O LOS (bottom row) for a R_{ax} = 3.6 m case. Colors correspond to the distance from the diagnostic beamline (NB3 for 7-O LOS, NB4 for 6-O LOS) with values truncated above 30 cm. (a) Radial flux coordinate $\rho = \sqrt{\psi/\psi_{edge}}$. Electron (b) density and (c) temperature along the sightlines.

FICXS signals in the present study are normalized by the beam emission spectrum (BES) to account for the neutral density profile of the injected diagnostic beam. Using the BES-normalized signal, we define FIDA density = FICXS/BES. Additionally, signals are integrated over wavelengths corresponding to E_{LOS} = 20 - 60 keV for the 6-O LOS and 100 - 120 keV for the 7-O LOS. Profiles for the two sightlines with their respective integration regions are referred to as low-energy FIDA density (6-O LOS) and high-energy FIDA density (7-O LOS).

5.1.4 Considerations for 7-O LOS collecting volume

The parametric study presented in section 5.2.1 relies on plasma parameters that are local to the intersection of the sightline and the diagnostic beamline. However, due to the small angle between the high-energy view and the associated diagnostic beam, some disagreement with the local model is expected. Recalling that the high-energy view uses 7-O LOS with NB3

and the low-energy view uses 6-O LOS with NB4, the viewing angle between the LOS and diagnostic beam is $\sim 10^\circ$ for the high-energy view and $\sim 30^\circ$ for the low-energy view. NB3 and NB4 beam footprints are approximated by the aperture radius of 30 cm. The sightline collecting volume can then be reduced to the length of the sightline within the 30 cm radius. Parameters within the collecting volumes for 6-O and 7-O LOS are shown in Fig. 5.6. The first column of Fig. 5.6 shows that the 7-O LOS stays within the beam footprint from the outer flux surface ($\rho = 1$) to the axis ($\rho = 0$) while the 6-O LOS is localized to different locations for each channel. The second and third columns show electron parameters over the collecting volume. As expected due to the large span in ρ, the plasma parameters along the 7-O LOS collecting volume vary greatly. Quantitative comparisons of variations in plasma parameters and a metric ℓ for the collecting volume are shown in Fig. 5.7. The parameter ℓ is defined as a line integral

$$\ell = \int_L \rho \, dl \tag{5.4}$$

where L is the section of the LOS that is within 30 cm of the beam centerline and dl is along the LOS. There is virtually no variation in ℓ for the 6-O LOS with a constant value of 0.7 m^2. For the 7-O LOS, ℓ ranges 2.3-3.8 m^2, 3-5$\times$ larger than the 6-O LOS. Variations in plasma parameters along the LOS are quantified by Δn_e and ΔT_e where the difference Δ is taken between the maximum and minimum value of the parameter along the active LOS. While there is some variation of parameters along the 6-O LOS, it is well below the volume-averaged density $\bar{n}_e \sim 1.0 \times 10^{19}$ m^{-3} and temperature $\bar{T}_e \sim 1.0$ keV. The variation of parameters along the 7-O LOS is much greater with Δn_e nearly half of $\bar{n}_e$ and ΔT_e around 75% larger than $\bar{T}_e$ for almost all channels. Due to the small angle between the 7-O LOS and NB3, the local model discussed in section 5.2.1 is expected to deviate from ideal values.

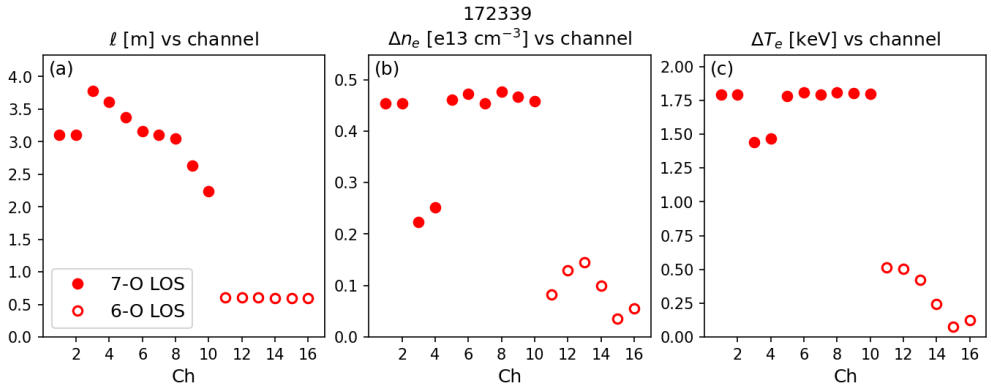

Figure 5.7: Change in parameters along sightlines within a 0.3 m half-width beam footprint for the diagnostic beams for a $R_{ax} = 3.6$ m case. (a) Length ℓ of sightline within the beam footprint. Change in electron (b) density and (c) temperature along the sightline within the diagnostic beam volume.

5.1.5 Normalization of Goldston distribution

FIDASIM results are calculated for two diagnostic beam cycles from each selected sample in the dataset using the Goldston model discussed in section 3.4. After the Goldston distribution $f_f^{Gold} \equiv f(\text{Energy}, \text{Pitch}, \rho)$ is calculated, it is normalized to the injected neutral current due to the heating beams I_{HNB} and a free-scaling parameter f_0 that is constant across all cases. The free parameter is determined by finding the best match between the neutron rate calculated by FIDASIM with neutron flux measurements [22] across all cases. The measured neutron emission rate is compared to FIDASIM in Fig. 5.8 for Goldston distributions with f_0 set to 1e3. Agreement within the same order of magnitude suggests a good estimation of the total number of fast ions in the Goldston distribution. A similar comparison of neutron rate calculations with a steady state distribution similar to the Goldston model was conducted in the PLT tokamak with similar agreement to measurements [26]. Scaling the distribution using neutron rates is primarily valid at high energies due to the velocity-space sensitivity of neutron emission described below.

Weight functions calculated using FIDASIM are compared between each configuration for select cases in Fig. 5.9. Weight functions $W \equiv W(\text{Energy}, \text{Pitch}, \lambda)$ for the low-energy view

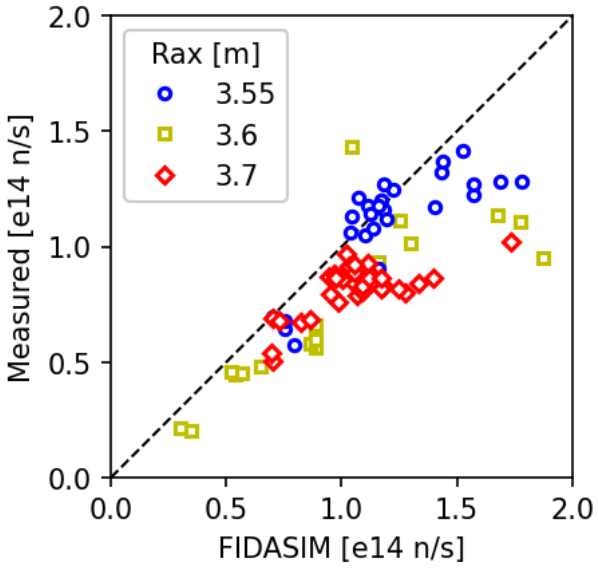

Figure 5.8: Measured vs simulated global neutron emission rates for three configurations. Open blue circle markers are R_{ax} = 3.6 m, open yellow square markers are R_{ax} = 3.55 m, and open red diamond markers are R_{ax} = 3.7 m. Markers for all three configurations are fairly linear showing close to one-to-one relation between measurements and FIDASIM. At higher values the markers start to diverge from the y = x line.

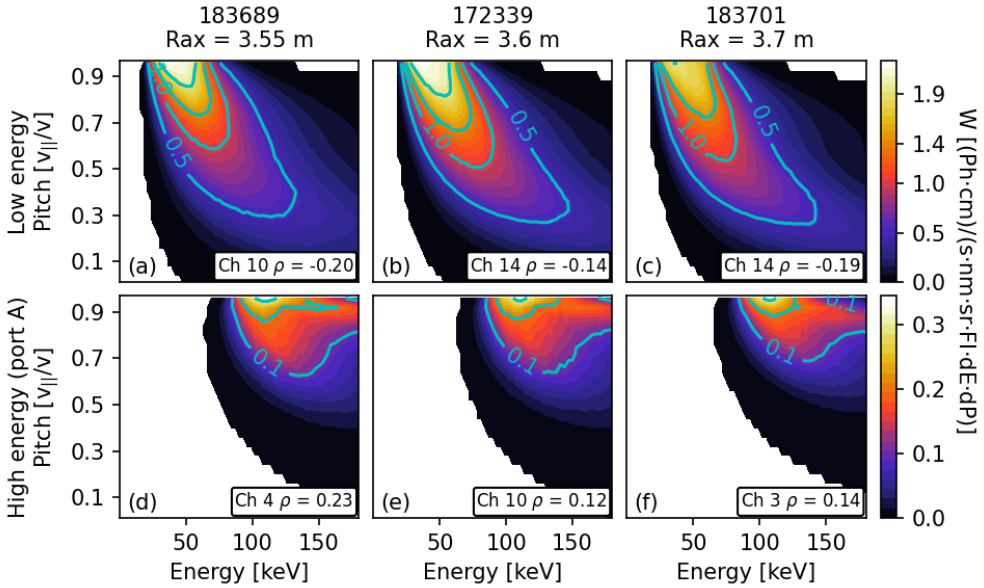

Figure 5.9: Weight functions calculated by FIDASIM for three configurations. Weight functions for each sightline are integrated over the wavelengths for E_{LOS} = 20-60 keV for low energy (top row) and E_{LOS} = 100-120 keV for high energy (bottom row). Each filled contour is a 5% increase from W_{min} to W_{max}, where W_{min} is the lowest nonzero value. Contour levels associated with the colorbar ticks are highlighted in cyan.

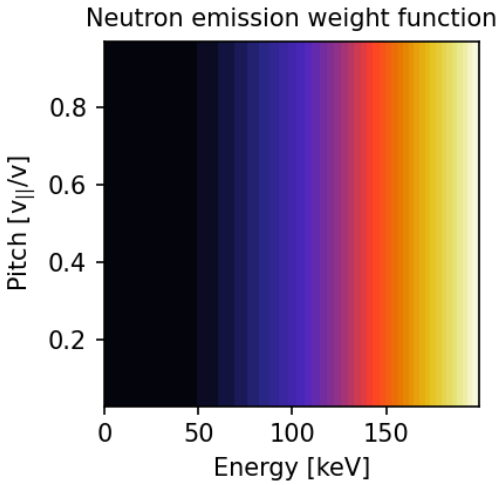

Figure 5.10: Weight function for global neutron emission.

extend to pitch = 0.3 within $0.25\max(W)$ while weight functions for the high-energy view quickly fall off below pitch = 0.6. The R_{ax} = 3.55 and 3.6 m cases have similar sensitivity for the low-energy view while the R_{ax} = 3.7 m case is less sensitive with a 25% reduction of $\max(W)$. FICXS signals are calculated by integrating over velocity-space so the weight function for the R_{ax} = 3.7 m is considered to be similar to other configurations. Weight functions for the high-energy view are virtually identical for all three configurations with a sensitivity to strongly passing fast ions near the injection energy. The energy dependence of high-energy view weight functions is similar to the neutron emission weight function shown in Fig. 5.10. In finite-rotation plasmas, the neutron emission weight function is anisotropic in pitch However, for LHD plasmas with minimal rotation the neutron emission weight function is independent of pitch angle.

5.1.6 Variation in Doppler broadening of beam emission feature

The two heating beams considered in the present study use two sources each with slightly different geometries. Here we discuss the changes in FIDA density measurements due to the different geometries of the two NB3 sources. The on- or off-axis geometries for source A and source B results in different fast ion birth profiles. However, relaxation of birth profiles to

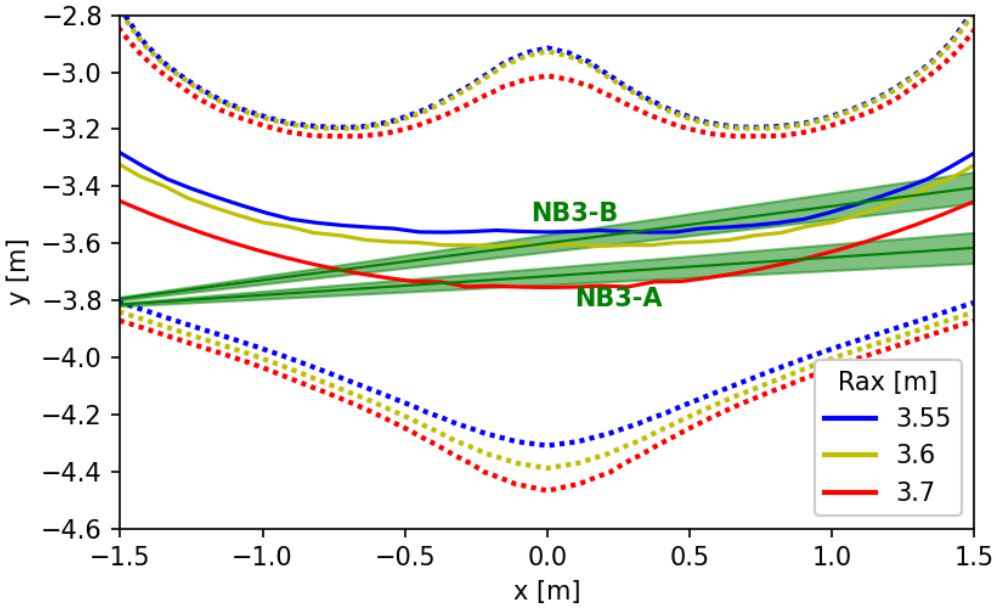

Figure 5.11: Mid plane view of NB3 injection geometries and VMEC equilibria for three configurations. Solid lines indicate magnetic axes and dotted lines indicate boundary surfaces. Shaded regions surrounding the beamlines show the estimated beam footprint due to the beam divergence.

the full distribution due to transport may mitigate any differences caused by source A vs source B. Figure 5.11 shows the NB3 source geometries overlaid on the magnetic axes and boundary surfaces for three configurations. NB1 has a similar geometry. Source B typically injects on-axis for $R_{ax} = 3.55$ and 3.6 m cases while source A is on-axis for $R_{ax} = 3.7$ m cases. A comparison of measured FIDA density with source A and B is shown in Fig. 5.12. Due to parametric dependencies discussed in section 5.2.1, comparison of ports is restricted to cases with similar densities. The $R_{ax} = 3.6$ m case (Fig. 5.12 middle column) lacks a sufficient number of low-energy source A samples for comparison with source B, as well as lacking samples for both sources for the high-energy FIDA density. However, there is sufficient data for both ports for $R_{ax} = 3.55$ and 3.7 m with additional source B values hidden in Fig. 5.12 (left and right columns) due to overlapping of points. Under identical plasma conditions for the low-energy case, there appears to be little difference in the measured FIDA density between the A and B ports for the $R_{ax} = 3.55$ case as well as for the 3.7 m case. Interpolating in between, the low-energy $R_{ax} = 3.6$ m case can then be assumed to be indifferent to the A

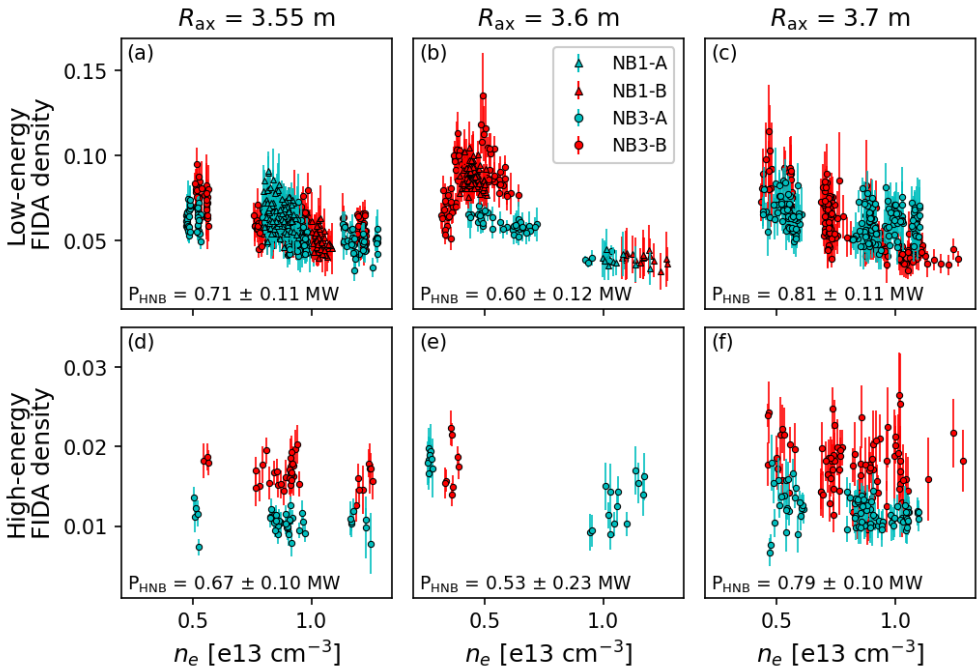

Figure 5.12: FIDA density for three configurations vs electron density for all MHD-quiescent cases. Error bars are one standard deviation. Triangle markers indicate NB1 heating and circle markers indicate NB3 heating with cyan and red indicating source A and source B, respectively. Average heating power within each sample is listed for each configuration. Due to overlap in points in (a, c), some additional source B points are hidden under source A points.

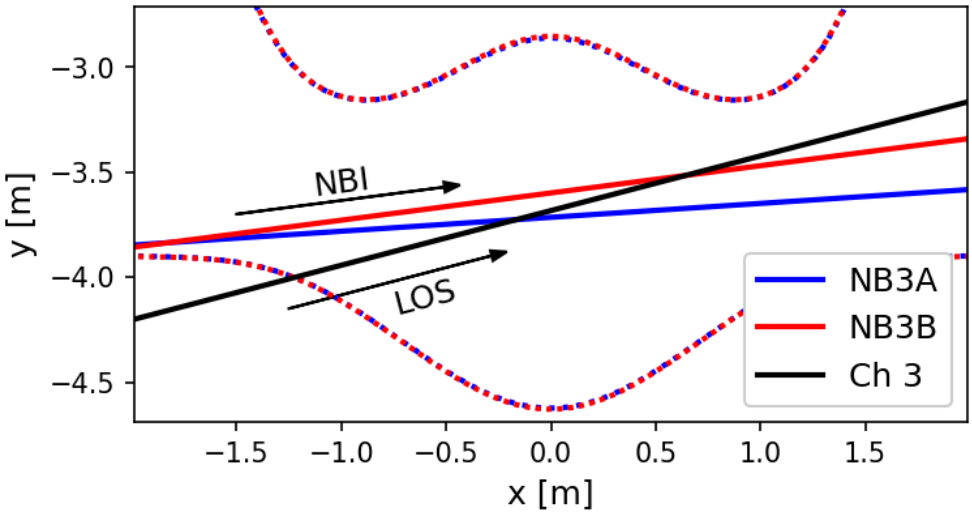

Figure 5.13: Mid plane view of NB3 injections geometries and 7-O LOS channel 3 geometry. Plasma boundaries calculated by VMEC are shown by dashed lines for NB3-A heating (blue, 183699) and NB3-B heating (red, 183698). Solid lines in blue and red indicate the NB3-A and NB3-B beamline geometries, respectively. The geometry for 7-O LOS channel 3 is indicated by a solid black line. Arrows indicate the direction away from the NBI source or FICXS collecting optics.

and B ports. This also suggests that the distribution of low-energy fast ions is independent of source A vs source B, confirming that slowing down of the initial birth profile due to transport mitigates any differences. For the high-energy case, there is consistent difference in FIDA density due to NB3 source A and source B. However, the difference in measurements is independent of R_{ax}. Note that NB1 sources are not considered in the high-energy cases since only one heating source is used and NB3 is used for both heating and diagnostic purposes. The consistent difference in signal across R_{ax} suggests this effect is not caused by differences in the fast ion birth profile due to source A vs source B. Overall, the fast ion distribution does not appear to be significantly affected by source A vs source B injection of the tangential heating beams but additional considerations must be made to explain the differences in the high-energy FIDA density.

High-energy cases show that source B FIDA density is higher regardless of the magnetic configuration under similar plasma conditions. Recalling that FIDA density is calculated

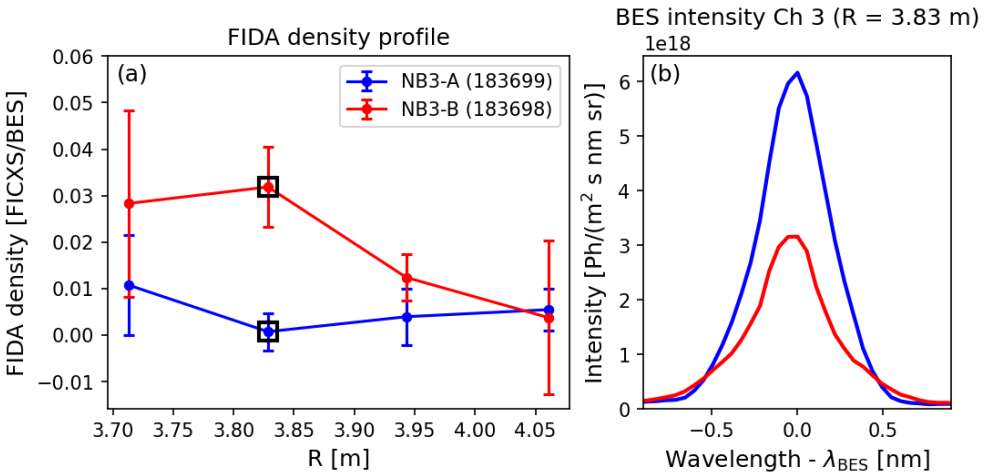

Figure 5.14: (a) FIDA density profile and (b) BES intensity for NB3-A heating (blue) and NB3-B heating (red). BES intensity in (b) is shown for channel 3 which is highlighted by an open square marker in (a). The abscissa origin in (b) is set to the wavelength of the BES peak.

by normalizing FICXS with the beam emission spectra (BES) feature from the diagnostic beam, the high-energy view uses a single beam for both heating and diagnostic purposes. The viewing angle between the high-energy view and NB3 is relatively small ($\sim 10°$) so the BES normalization requires special consideration depending on which beam source is used. The small viewing angle between the 7-O LOS and the NB3 ports results in different Doppler-broadening of the BES feature that is sensitive to the small angle difference in the source A and source B geometries ($\sim 4°$). The geometry for one high-energy LOS (Ch. 3) is shown in Fig. 5.13. Source B BES features experience more Doppler broadening resulting in a smaller BES normalization factor and an overall higher FIDA density. BES features for Ch. 3 resulting from source A vs source B are shown in Fig. 5.14. Conversely, a similar analysis of the low-energy FIDA density vs the diagnostic NB4 sources finds no significant dependence on the diagnostic beam source. The viewing angle between the low-energy LOS and NB4 sources is $\sim 30°$ and the difference in NB4 source A and source B geometries is $\sim 6°$. The larger viewing angle results in Doppler-broadening of the low-energy view BES feature that is insensitive to NB4 source A vs source B. The following analysis will treat

the low-energy FIDA density as unaffected by the heating and diagnostic sources while the high-energy FIDA density will be separated according to the heating-diagnostic sources.

5.2 Experimental results

5.2.1 Parametric study of FICXS measurements

A parameter scan is conducted over the selected MHD-quiescent discharges with individual samples for each diagnostic cycle in each discharge. Measured FIDA density is dependent on the diagnostic beam parameters, heating beam parameters, and plasma parameters local to the sightline [44]. Using a local approximation, the measured FICXS signal is proportional to the fast ion density n_f and injected neutral density of the diagnostic neutral beam (DNB) n_{DNB}. Since the NB1 and NB3 injection energy (160 keV) is larger than the critical energy ($\sim$ 30 keV), fast ions slow down primarily on electrons. Therefore, a rough estimate of n_f can be made by the heating neutral beam (HNB) power P_{HNB} and the Spitzer slowing-down time $\tau_S \propto T_e^{1.5}/n_e$. Additionally, the BES feature is proportional to the diagnostic beam neutral density n_{DNB} and electron density n_e. Consequently, the FIDA density $\hat{S}$ = FICXS/BES is expected to depend approximately on the beam and plasma parameters by

$$\hat{S} \propto n_f/n_e \propto P_{HNB} T_e^{1.5} n_e^{-2}. \tag{5.5}$$

To analyze the data, we assume the more general dependence,

$$\hat{S} = A_0 P_{HNB}^{a_1} T_e^{a_2} n_e^{a_3}, \tag{5.6}$$

where A_0 is a constant and a_1, a_2 and a_3 are fitting coefficients.

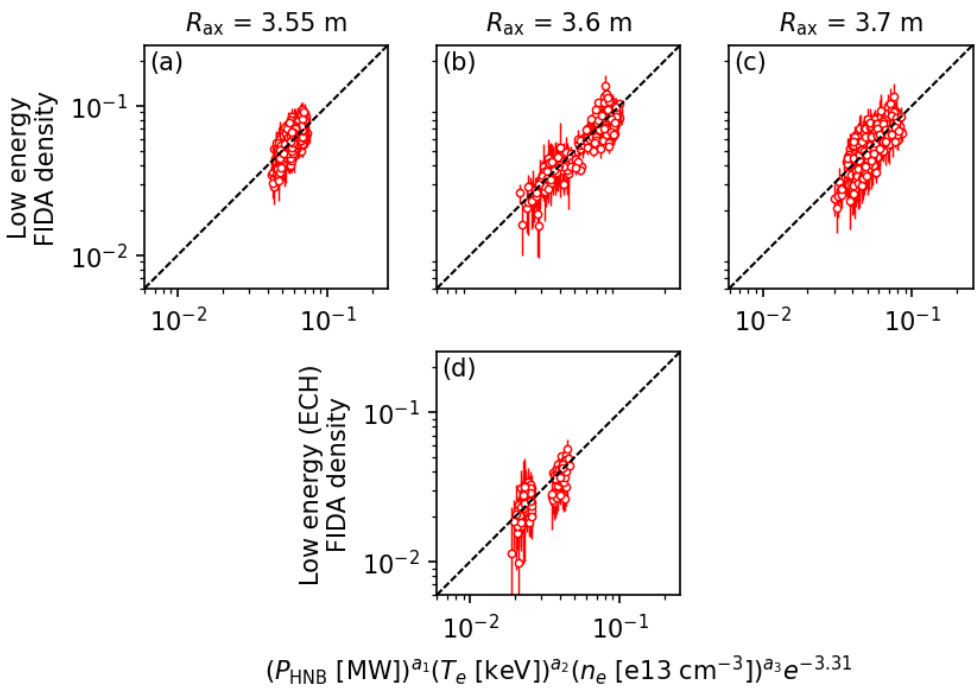

Figure 5.15: Low-energy FIDA density vs fitted plasma and beam parameters for (a-c) NBI heated cases and (d) NBI + ECH heated cases. Error bars are one standard deviation. Dashed lines are y = x.

Fitting coefficients are determined by log-linear regression shown in Fig. 5.15 for the low-energy FIDA density and Fig. 5.16 for the high-energy FIDA density cases. A_0 is determined empirically by comparison of goodness-of-fit using reduced-chi square χ^2_ν values across all three R_{ax} configurations. Results of the regression are listed in Table 5.2 for low-energy FIDA density and Table 5.3 for high-energy FIDA density.

The low-energy FIDA density behavior has some agreement with expectations with a positive correlation with power (a_1), a positive correlation with temperature (a_2) and a negative correlation with density (a_3). However, the dependencies are weaker than expected with $a_1 < 1$, $a_2 < 1.5$, and $|a_4| < 2$ for all R_{ax}. The ECH-heated cases are similar to the non-ECH cases but with an even weaker temperature dependence. The weak temperature dependence of the ECH-heated cases agrees with a previous study that used the LHD FICXS diagnostic [35].

Measurement	Fitting coefficient	R_{ax} [m] 3.55	3.6	3.7
Low energy FIDA density No ECH	a_1	0.34 ± 0.04	0.38 ± 0.03	0.25 ± 0.10
	a_2	0.74 ± 0.01	0.63 ± 0.03	0.91 ± 0.03
	a_3	−0.33 ± 0.03	−0.67 ± 0.03	−0.54 ± 0.06
	χ^2_ν	1.65	2.44	1.44
	ν	627	287	482
Low energy FIDA density With ECH	a_1		0.81 ± 0.04	
	a_2		0.13 ± 0.02	
	a_3		−0.43 ± 0.05	
	χ^2_ν		1.18	
	ν		123	

Table 5.2: Log-linear fitting coefficients for low-energy FIDA density across three configurations with only NBI heating along with ECH cases for R_{ax} = 3.6 m. Goodness-of-fit measures are listed as χ^2_ν with the associated degrees of freedom ν. Parameters are fit to $\hat{S} = A_0 P_{HNB}^{a_1} T_e^{a_2} n_e^{a_3}$ with power in MW, temperature in keV, density in 10^{13} cm^{-3} and $A_0 = e^{-3.31}$.

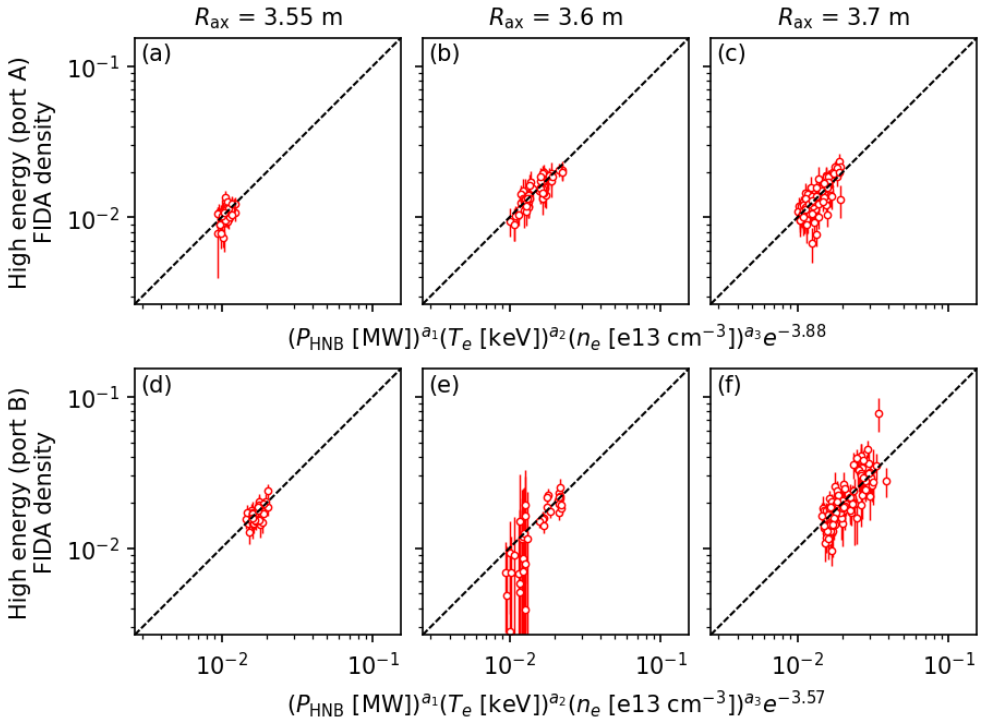

Figure 5.16: High-energy FIDA density vs fitted plasma and beam parameters for (a-c) source A heating and (d-f) source B heating. Error bars are one standard deviation. Dashed lines are y = x.

Measurement	Fitting coefficient	R_{ax} [m] 3.55	3.6	3.7
High energy FIDA density source A	a_1	1.26 ± 0.36	0.01 ± 0.07	0.61 ± 0.21
	a_2	-0.54 ± 0.20	-1.09 ± 0.08	-1.04 ± 0.06
	a_3	-1.05 ± 0.22	-0.31 ± 0.06	-0.61 ± 0.13
	χ^2_ν	0.80	0.44	1.22
	ν	43	57	109
High energy FIDA density source B	a_1	0.73 ± 0.38	1.16 ± 0.34	-2.24 ± 0.31
	a_2	-0.58 ± 0.16	-1.23 ± 0.17	-1.24 ± 0.06
	a_3	-0.78 ± 0.24	-1.18 ± 0.31	0.87 ± 0.18
	χ^2_ν	0.66	0.94	1.25
	ν	43	36	109

Table 5.3: Log-linear fitting coefficients for high-energy FIDA density across three configurations for source A and source B heating. Goodness-of-fit measures are listed as χ^2_ν with the associated degrees of freedom ν. Parameters are fit to $\hat{S} = A_0 P_{\mathrm{HNB}}^{a_1} T_e^{a_2} n_e^{a_3}$ with power in MW, temperature in keV, density in 10^{13} cm^{-3} and $A_0 = e^{-3.88}$ for source A and $e^{-3.57}$ for source B.

The high-energy FIDA density is inconsistent across R_{ax} resulting in moderate to considerable deviation from the local model in eq. 5.5. Fitting coefficients for heating power (a_1) are positive and relatively close to unity except for a very weak dependency for $R_{ax} = 3.6$ m with source A and a negative coefficient for $R_{ax} = 3.7$ m with source B. Fitting coefficients for electron temperature (a_2) are all negative for both ports which does not match the expected behavior. Fitting coefficients for electron density (a_3) are all negative except for $R_{ax} = 3.7$ m with source B. Negative values for a_3 range from -0.31 ($R_{ax} = 3.6$ m, source A), which is similar to the lowest a_3 value in table 5.2, up to -1.18 which is the closest to the expected value of -2.

One possible explanation for poor agreement with eq. 5.5 is due to charge-exchange losses of fast ions due to thermal neutrals. The local model assumes that the fast-ion density n_f is proportional to the slowing-down time on electrons, $\tau_s \propto T_e^{3/2}/n_e$. However, if charge-exchange losses are important, then n_f ceases to increase with τ_S when τ_S exceeds the charge-exchange loss time τ_{CX}, implying a weaker dependence of the normalized FIDA signal on T_e than $T_e^{3/2}$ and on n_e than n_e^{-2}. At low densities ($\sim 0.5{\times}10^{19}$ m^{-3}), there is a finite

thermal neutral profile that is peaked at the edge. Indeed, in a study of the neutron decay rate following short beam pulses, *Nuga, et al.* found that, when τ_S was long, the measured decay rate was shorter than predicted [25]. Due to the radial dependence of the profile, it stands to reason that FIDA density should have a radial dependence independent of the contributions of the radial electron density and temperature profiles. The generalized local model is modified to include the radial flux coordinate for each FICXS channel

$$\hat{S} = A_0 P_{HNB}^{a_1} T_e^{a_2} n_e^{a_3} s^{a_4}, \tag{5.7}$$

where $s = \psi/\psi_{\text{edge}}$. However, the fitting coefficient a_4 is found to be negligible with values around $\sim 10^{-2}$. In this case, any radial dependence of FIDA density must be provided by the density and temperature profiles with no additional contribution from the radial thermal neutral profile.

Another possible explanation for poor agreement of the low-energy FIDA density is due to the exclusion of thermal ion and impurity species in the local model. Fast ions primarily slow down on thermal electrons especially near the injection energy [16]. However, below the critical energy ion friction is comparable to electron friction. The critical energy E_{c} is defined as

$$E_{\text{c}} = 14.8\, A_{\text{f}}\, T_e \left\langle \frac{Z_i^2}{A_i} \right\rangle^{2/3} \tag{5.8}$$

$$\left\langle \frac{Z_i^2}{A_i} \right\rangle = \frac{\sum_i n_i (Z_i^2/A_i) \ln\Lambda_i}{n_e \ln\Lambda_e} \tag{5.9}$$

where A_{f} is the fast ion atomic number, A_i is the thermal ion atomic number, T_{e} is electron temperature in eV, n_{e} and n_{i} are electron and ion densities in cm^{-3}, Z_i is the thermal ion charge number, $\ln\Lambda_e$ and $\ln\Lambda_i$ are the electron and ion Coulomb logarithms, and subscript i is a species index [58]. Low-energy FIDA densities are integrated over $E_{\text{LOS}} = 20$-60 keV, which is near the expected critical energy of 30-50 keV. Within this range, the slowing-down time of

fast ions can vary 15-20% when including or excluding thermal ions. Unfortunately, thermal ion profiles are unavailable for many of the samples. Similar to FICXS, ion measurements are conducted using a charge-exchange spectroscopy (CXS) system with NB4 or NB5 as the diagnostic beam [15]. The CXS system measures carbon as the primary impurity which is used to calculate thermal ion profiles. Good CXS measurements require full power injection of the diagnostic beams. Many of the discharges in the data set use only half power which is found to produce sufficient FIDA emission for FICXS but insufficient for CXS. Carbon profile measurements are not available for many cases due to a lack of beam power for the diagnostic charge exchange system and are excluded from the present study. On the other hand, in a similar energy range (E_{LOS} = 30-80 keV), the tokamak study [44] found a relatively weak dependence of predicted FIDA signal on Z_{eff}, suggesting that the lack of impurity data is not a major shortcoming of our analysis.

Some disagreement between the high-energy density measurements and the local model is expected due to the large collecting volume discussed previously in section 5.1.4. An expanded model with finite spatial resolution could improve agreement with measurements. In the present study, we use FIDASIM with the Goldston distribution as an expanded model to evaluate both low- and high-energy FIDA density measurements.

5.2.2 Measurements compared to reduced model FIDASIM

While the Goldston model lacks radial transport, some agreement is found between FIDASIM and measurements just inside the mid-radius. Figure 5.17 shows the comparison of FIDA density between measurements and simulation. Low-energy FIDA density (Fig. 5.17(a-c)) show the best agreement just inside the mid-radius ($0.2 \leq \rho < 0.4$) with FIDASIM overestimating the core channels due to the absence of radial transport in the Goldston distribution. A qualitative order-of-magnitude comparison between $\mathrm{R_{ax}}$ configurations shows little change

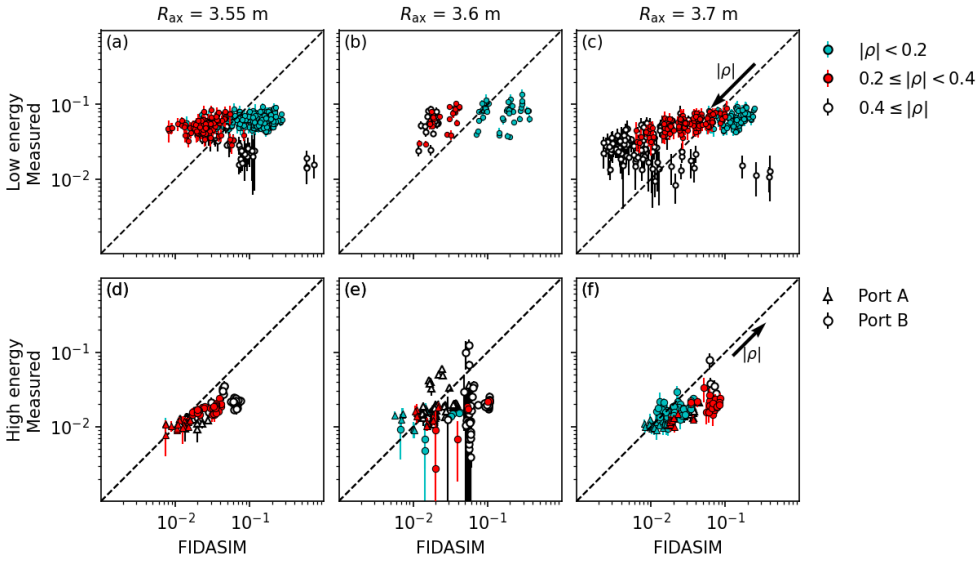

Figure 5.17: FIDA density measurements vs FIDASIM for three configurations. Closed circles indicate channels with $\rho < 0.4$ and open circles indicate channels with $\rho \geq 0.4$. Cyan circles indicate channels near the magnetic axis with $\rho < 0.2$ and red circles are near the mid-radius with $0.2 \leq \rho < 0.4$. Arrows in (c, f) show the direction of increasing ρ. Dashed lines correspond to y = x.

in FIDA density with the mid-radius to core channels consistently measuring just below $\hat{S} = 10^{-1}$. High-energy FIDA density (Fig. 5.17(d-f)) show a weaker radial dependence than the low-energy FIDA density resulting in a flat profile with an increase towards the plasma boundary. The weak radial dependence of the high-energy FIDA density is likely caused by the low spatial resolution as well as the use of the heating beam as a diagnostic beam since P_{HNB} and n_{DNB} come from the same source. For the high-energy FIDA density, FIDASIM consistently overestimates values for all ρ. This is due to the high-energy sensitivity of the high-energy FIDA density. Fast ions near the injected energy are expected to have a radial profile similar to the birth profile. The radial distribution for the Goldston model matches the birth profile, resulting in the shape of the simulated high-energy FIDA density profile matching the shape of the measured profile. The difference in overall magnitude is attributed to the use of an ideal model in FIDASIM, resulting in a higher number of fast ions across all ρ. This is consistent with a previous study using the high-energy LOS [31]. Similar to the low-energy FIDA density, the best agreement is near the mid radius.

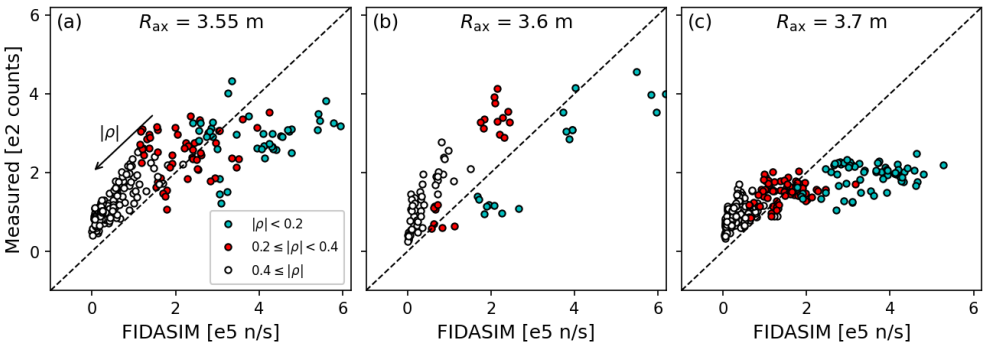

Figure 5.18: Relative comparison of measured VNC vs FIDASIM for three configurations. Closed circles indicate channels with $\rho < 0.4$ and open circles indicate channels with $\rho \geq 0.4$. Cyan circles indicate channels near the magnetic axis with $\rho < 0.2$ and red circles are near the mid-radius with $0.2 \leq \rho < 0.4$. Dashed lines represent y = x. The arrow in (a) show the direction of increasing ρ. Note that measured values have units of 1e2 counts while FIDASIM values have units of 1e5 neutrons/s.

Similar to simulated FIDA density, simulated VNC overestimates values near the axis and underestimates values near the edge due to the lack of radial transport in the Goldston model. Previous studies on the TFTR tokamak showed strongly peaked neutron collimator signals [59, 60]. In the tokamak studies, the experimental profiles agree well with simulated profiles calculated using the TRANSP code [36]. The Goldston model is intended for an ideal axisymmetric toroidal device so agreement with TRANSP is expected. Unlike the tokamak cases, the measured VNC has a broader profile than simulation, which results in FIDASIM overestimating neutron emission in the core and underestimating emission near the edge. The difference suggests that some high-energy fast ions experience transport that broadens the profile. Additionally, a study in the TFTR tokamak found that scattering of neutrons from the vessel walls can result in a 1-5% increase of the measured neutron flux which would contribute to disagreement with FIDASIM [61].

Figure 5.19 shows the experiment/theory ratio of FIDA density vs R_{ax} for both sightlines with averages taken from the ensemble of points associated with each R_{ax}. Values in the ensembles are selected to minimize the variation in plasma parameters while ensuring a reasonable number of data points. The number of points in each group that contribute

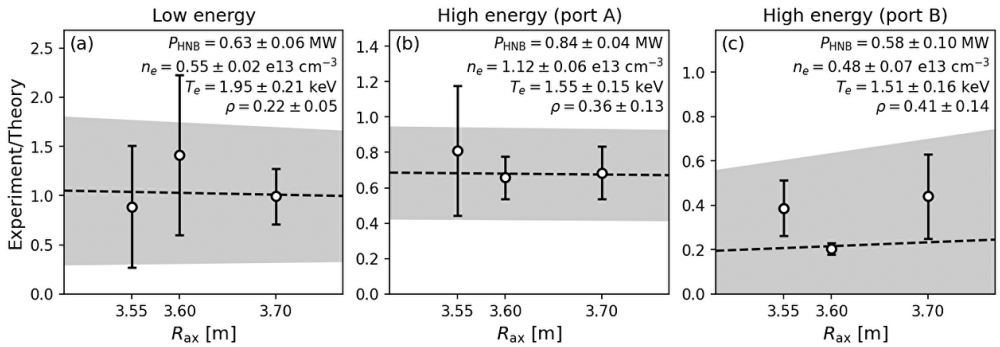

Figure 5.19: Experiment/theory ratio vs R_{ax} for (a) low-energy FIDA density, (b) high-energy FIDA density for source A heating, and (c) high-energy FIDA density for source B heating. Best-fit lines are shown by dashed lines. Shaded regions around the best-fit line represents the cumulative error of the fit and the variance of the means. Average beam and plasma parameters are listed for each case.

	R_{ax} [m]		
Measurement	3.55	3.6	3.7
Low-energy FIDA density	11	9	12
High energy FIDA density (source A)	12	22	13
High energy FIDA density (source B)	6	10	8
VNC	10	3	10

Table 5.4: Number of data points used in calculating values for Fig. 5.19 and Fig. 5.20(d).

to the values in Fig. 5.19 are listed in Table 5.4. Averages of measured FIDA density for each R_{ax} are acquired by an inverse-variance weighted average. Standard deviations of measured FIDA density for each R_{ax} are acquired from the cumulative error of the individual measured errors and the variance of the data points. Averages and standard deviations of simulated FIDA density for each R_{ax} are acquired from an arithmetic mean and variance of data points. Experiment/theory values for both low-energy FIDA density (Fig. 5.19(a)) and high-energy FIDA density for source A Fig. 5.19(b)) are within 1 standard deviation across R_{ax}. Experiment/theory values for high-energy FIDA density with source B (Fig. 5.19(c)) for $R_{ax} = 3.55$ and 3.7 m are identical but there is a decrease at $R_{ax} = 3.6$ m. The decrease is likely due to differences in beam and plasma parameters which are virtually identical between $R_{ax} = 3.55$ and 3.7 m while samples with identical parameters for $R_{ax} = 3.6$ m could not be found.

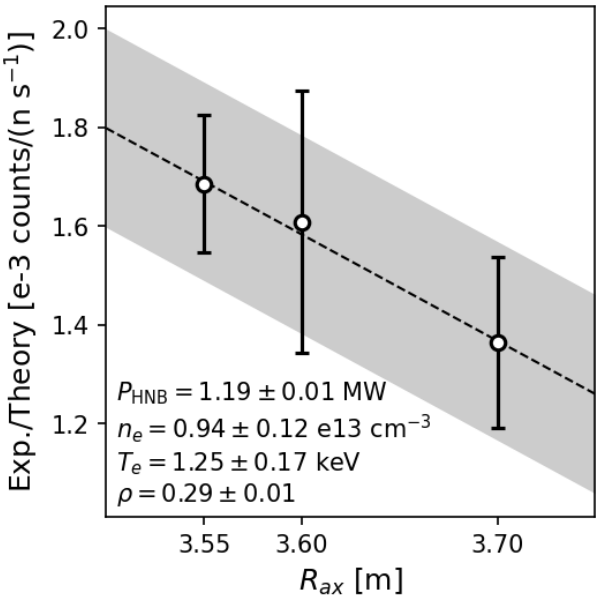

Figure 5.20: Experiment/theory ratio for VNC vs R_{ax}. Errorbars represent one standard deviation. Best-fit lines are shown by a dashed line. Shaded regions around the best-fit line represents the cumulative error of the fit and the variance of the means. Note that experiment/theory values are plotted with units of $1{\times}10^{-3}$ counts/(n/s).

Experiment/theory values for VNC across R_{ax} are shown in Fig. 5.20. Sample sizes for each R_{ax} group are listed in Table 5.4. Averages and standard deviation in Fig. 5.20 are acquired from an arithmetic mean and variance of data points. Both R_{ax} = 3.55 and 3.7 m fall within one standard deviation of experiment/theory for R_{ax} = 3.6 m. However, only 3 samples were used for the R_{ax} = 3.6 m case compared to 10 samples for the other two configurations (table 5.4). The difference in experiment/theory values between R_{ax} = 3.55 and 3.7 m suggests reduced neoclassical transport. Similarities between measurements and FIDASIM resulting in experiment/theory close to unity are expected to some degree since the input plasma parameters are taken directly from measurements. The increase in experiment/theory values at smaller R_{ax} is likely due to the exclusion of neoclassical transport in the Goldston distribution. Additionally, the lack of dependence on R_{ax} for FIDA density (Fig. 5.19) suggests that fast ion orbits visible to FICXS do not experience improved confinement due to the shifted axis while orbits visible to VNC do experience improved confinement. Inward-shifted configurations are expected to primarily affect low-

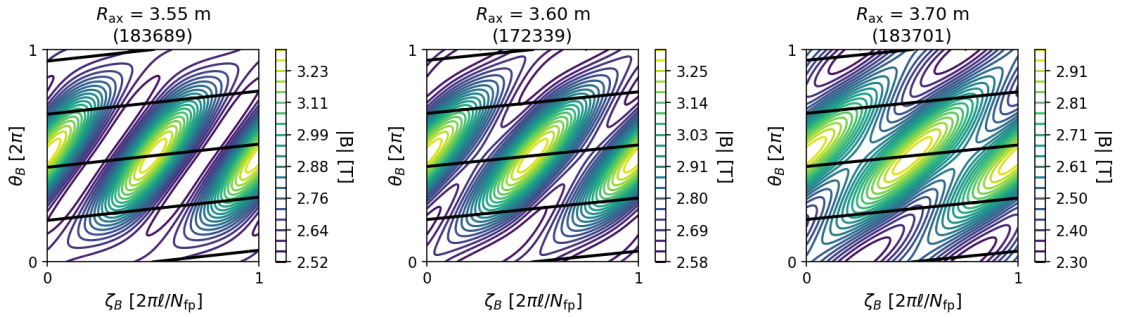

Figure 5.21: Field contours at the $\sqrt{\psi/\psi_{\text{edge}}} = 0.5$ surface for three configurations. Fields are calculated by VMEC and transformed to Boozer coordinates using BOOZ_XFORM. Each contour line is a 5% increase from B_{min} to B_{max}. Black lines indicate field lines.

pitch trapped fast ion orbits. VNC is insensitive to pitch (Fig. 5.10) and is able to diagnose regions of phase space at low pitch that is invisible to FICXS (Fig. 5.9). Further analysis of fast ion orbits across different pitch angles is discussed in the next section.

5.3 Extended simulation results

In this section, equilibrium calculations and orbit simulations are used to further infer changes or lack of changes in neoclassical confinement seen by the fast ion diagnostics.

5.3.1 Pressure-induced axis shift

Previous results by *Wakasa, et al.* [46] relied on vacuum-field VMEC with clockwise B_t for a hydrogen plasma to analyze the R_{ax} = 3.6 m case, in finite-β plasmas this is found to correspond to the R_{ax} = 3.55 m case due to the pressure-induced shift of the axis. Figure 5.21 shows B-field contours calculated by finite-β VMEC for three configurations at the mid-radius as functions of Boozer angles calculated by BOOZ_XFORM[62]. The R_{ax} = 3.7 m case shows a large variation in B_{min} along a field line while the R_{ax} = 3.55 m case shows a reasonably uniform B_{min}. This is highlighted in Fig. 5.22 which shows the field strength

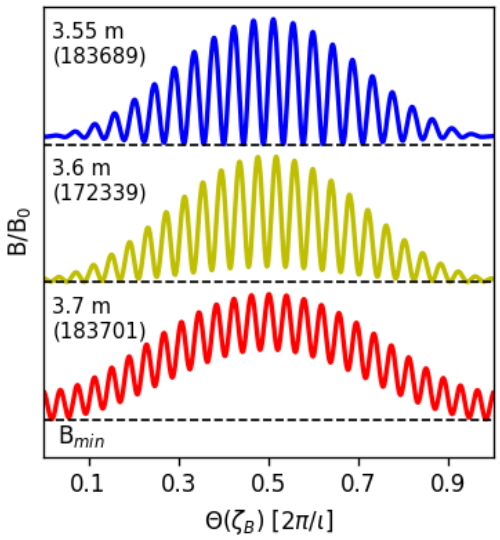

Figure 5.22: Normalized field strength along the field lines in Fig. 5.21. Curves are labeled by their vacuum R_{ax} . The x-axis is the Boozer field line parameter $\Theta(\zeta_B) = m\theta_B - nN_{fp}\zeta_B = (m\iota - nN_{fp})\zeta_B$ using the relation $\theta_B = \iota\zeta_B$.

along a field line for three configurations. The uniform B_{min} for the R_{ax} = 3.55 m case matches what was previously found for the R_{ax} = 3.6 m case using vacuum-field VMEC. In the previous study, The uniform B_{min} was found to be caused by an increase in amplitude of the (m, n) = (1, 10) and (3, 10) Fourier components $B_{m,n}$ for the magnetic field. Fourier components for the finite-β case with counterclockwise B_t in a deuterium plasma are shown in Fig. 5.23. An increase in the (1, -10) and (3, -10) amplitudes matches the previous clockwise B_t results. There is also an increase in the (0, 10) and (2, 0) components observed in the finite-β case.

The difference in R_{ax} between the vacuum-field vase and finite-β case is further highlighted with the calculated pressure-induced shift in R_{ax} . Figure 5.24 shows the field-period averaged magnetic axis position calculated by finite-β VMEC vs the vacuum R_{ax} configuration. Since the cases were selected to have identical plasma parameters, the plasma β is relatively constant across R_{ax} configurations and all axes are shifted by approximately 5 cm. This results in the R_{ax} = 3.55 m case matching the expected behavior of vacuum R_{ax} = 3.6 m during experiments.

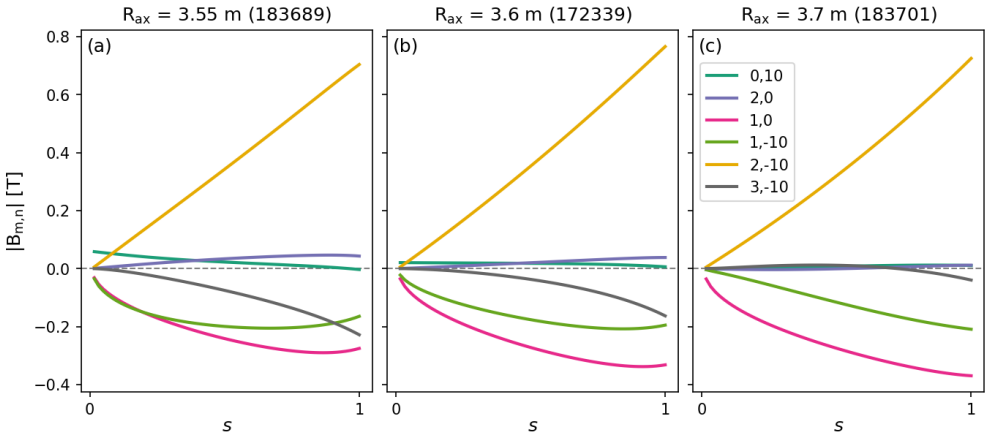

Figure 5.23: Fourier components of magnetic field strength for three R_{ax} configurations.

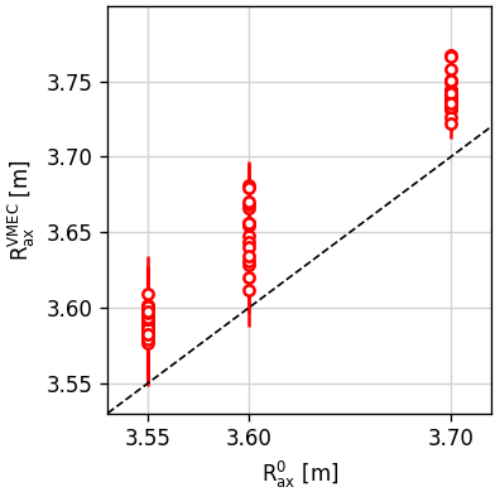

Figure 5.24: Field-period-averaged R_{ax} calculated by VMEC compared to the vacuum configuration. VMEC values are acquired from averaging the calculated, toroidally-dependent R_{ax} values over one field period with error bars representing one standard deviation.

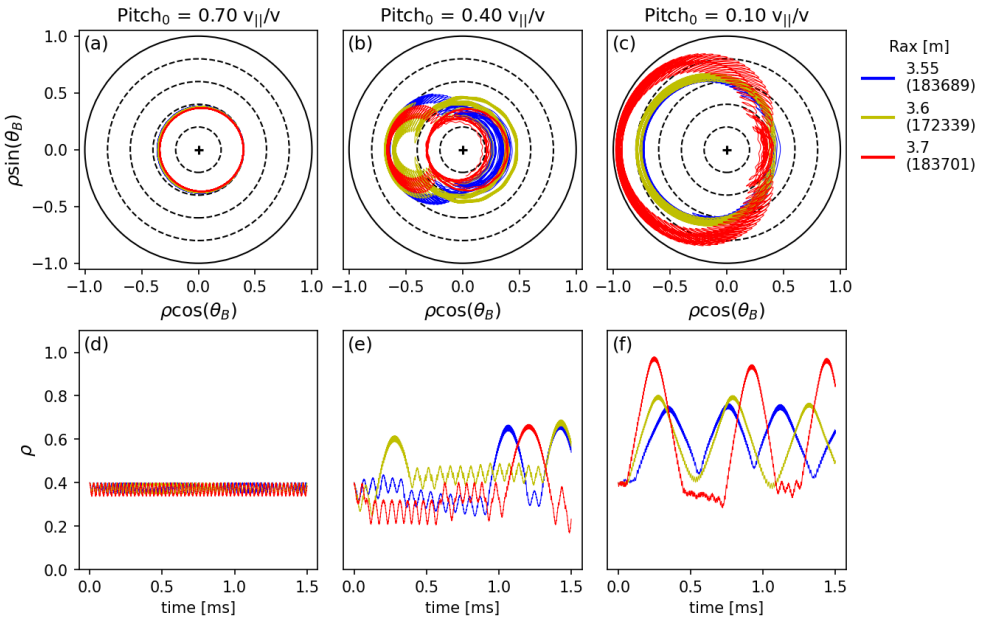

Figure 5.25: Orbits calculated by DELTA5D for three configurations and three initial pitch values. (a-c) Poloidal projection of flux-surface-mapped orbits. Dashed-line circles indicate flux surfaces at $\rho = (0.2, 0.4, 0.6, 0.8)$ with a solid line for $\rho = 1$. (d-f) Radial displacement vs time.

5.3.2 Orbit simulations

Collisional guiding-center simulations are conducted using DELTA5D [63] to identify different orbit classes at different pitch values. 50 keV fast ions are launched from the mid-radius with three pitch values = 0.7, 0.4, 0.1 and followed for 1.5 ms. Results are shown in Fig. 5.25. Fast ions with pitch = 0.7 remain passing within the runtime regardless of R_{ax} configuration. At pitch $\sim$ 0.4, fast ions enter weakly-trapped transition orbits with similar radial drifts ($\Delta\rho \sim 0.3$). At pitch $\sim$ 0.1, fast ions in the R_{ax} = 3.55 and 3.6 m cases enter deeply trapped orbits with moderate radial drift ($\Delta\rho \sim 0.3$). Fast ions in the R_{ax} = 3.7 m case stay in transition orbits with large radial drift ($\Delta\rho > 0.6$). Weight functions for both FICXS sightlines (Fig. 5.9) suggests that the majority of measurements are sensitive to fast ions with pitch above 0.6. This would mean that only passing fast ions are seen by the FICXS diagnostic. Improvement in confinement due to inward-shifted R_{ax} is largely reserved for trapped particles [47, 46, 38]. Therefore, FICXS does not see any improvement in fast ion

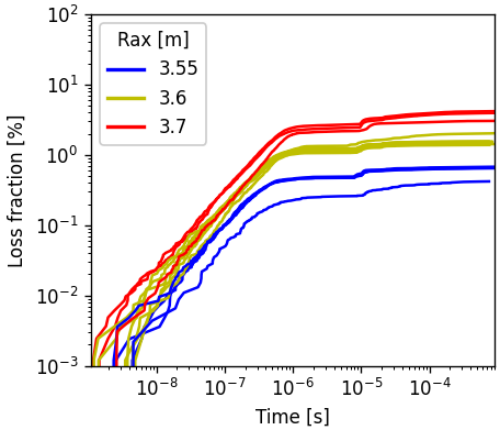

Figure 5.26: Loss fraction vs time of passing fast ions with initial energy 50 keV for three configurations calculated by SIMSOPT. Passing fast ions are considered lost when they transition to a trapped orbit or exit the plasma.

confinement due to the reduced neoclassical transport in the inward-shifted configuration. This is further supported by the observed increase in VNC signal with smaller R_{ax}. Since the VNC diagnostic sensitivity (Fig. 5.10) extends to low pitch, improved confinement of trapped fast ions with pitch below 0.6 is visible to VNC.

In addition to DELTA5D simulations, loss fractions are calculated using SIMSOPT [64] to track 50 keV passing fast ions. Fast ions are given an initial pitch of 0.95 and are considered lost if they exit the plasma or transition to a non-passing orbit. Loss fractions for three R_{ax} configurations are shown in Fig. 5.26. Simulations show a 3% reduction in losses from R_{ax} = 3.7 to 3.55 m which is unexpected. Passing fast ion orbits are dismissed in neoclassical theory since the net radial drift is often negligible compared to trapped orbits [47]. However, a 3% change in signal is smaller than measurement errors (Fig. 5.19) and weaker than the parametric dependencies discussed in section 5.2.1.

Chapter 6

LHD plasmas with instabilities

This chapter will discuss Alfvén eigenmodes (AE) observed in LHD and the effects on fast ion confinement. AEs are readily observed in low-field discharges in LHD with the toroidal (TAE) and reverse-shear (RSAE) modes exhibiting behavior similar to tokamaks [65, 29]. Helicity-induced (HAE) modes existing in continuum gaps caused by helical coupling have also been observed in LHD [30]. Radial transport of fast ions due to AEs in LHD has been observed using neutral particle measurements, fast neutron emission measurements, and fast-ion loss detectors [66, 67]. The study presented in this chapter will focus on FIDA density measurements in discharges where mode activity is observed. The first section discusses observations of modes in high-field cases, the second section discusses observations of modes in a low-field case. Measurements are compared to FIDASIM using the Goldston model. Both measurements and FIDASIM are compared to results from the previous chapter on measurements in MHD-quiescent plasma.

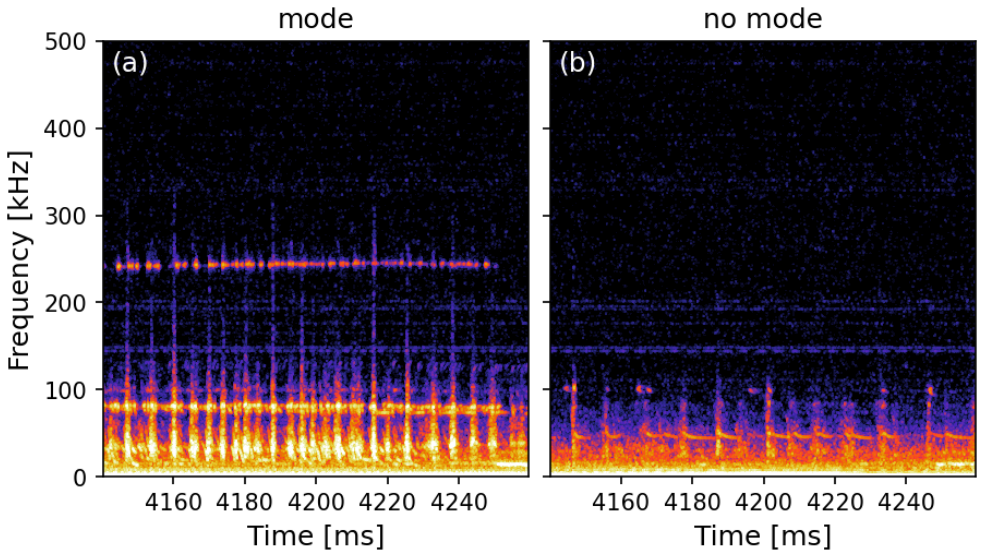

Figure 6.1: Power spectral densities for high-field cases with a 240 kHz mode (a) and no mode activity (b).

6.1 High-field cases

AE-like instabilities are measured in LHD at high-field due to counter-B_t injected NBI. Figure 6.1 shows power spectral densities of magnetic fluctuations for a case with full power NB2 (a) and half power NB2 (b). Both discharges are from the same experiment with R_{ax} = 3.6 m, B_t = 2.75 T on axis, CCW-B_t, and deuterium beams into deuterium plasma. Time traces for beam power, neutron emission, and magnetic fluctuations are shown in Fig. 6.2. The instability is observed in discharge 172348 with twice the injected NB2 power compared to discharge 172352 where no instability is observed. Global neutron emission rate is observed to increase with total injected beam power. While confinement properties for co- and counter-passing fast ions are different [68], an overall increase in fast ions due to neutral beam heating contributes to an increase in neutron emission.

Alfvén continuum calculations are compared with toroidal mode numbers n calculated from the array of magnetic fluctuation probes. An array of six probes are placed at integer multiples of $2\pi/N_{fp}$. Only coherent activity $C_{xy} > 0.7$ is considered. The magnitude-squared

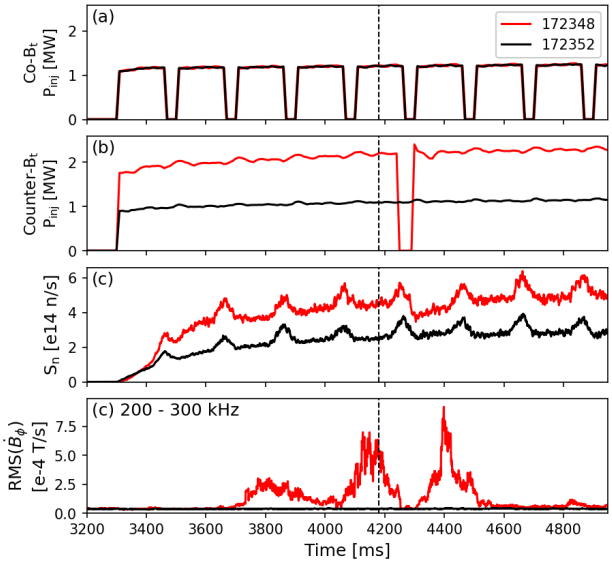

Figure 6.2: Time traces for high-field cases showing (a) co-B_t injected NBI power, (b) counter-B_t injected NBI power, (c) global neutron emission rate, and (d) root-mean-square (RMS) of toroidal magnetic field fluctuations in the 200-300 kHz range.

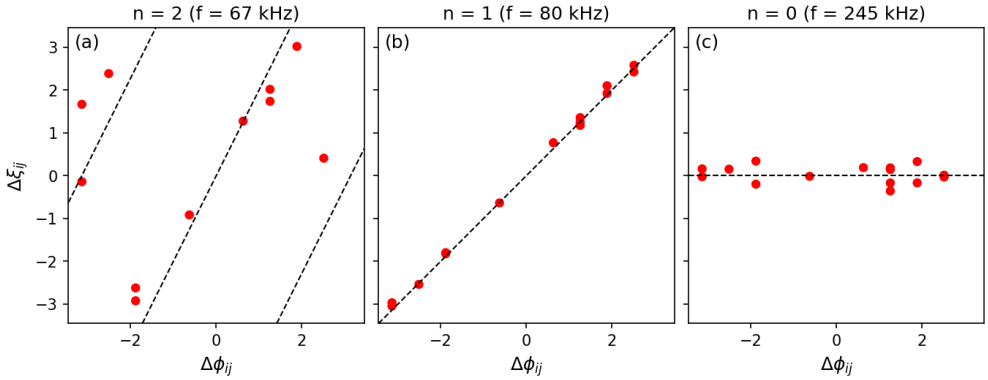

Figure 6.3: Phase shift vs probe spacing for three frequencies with the calculated toroidal mode numbers. Values in the abscissa correspond to spacing between probes. Values in the ordinate correspond to phase angle between probes. Dashed lines show the calculated mode number as $y = nx$.

coherence C_{xy} between two probes is calculated by

$$C_{xy} = \frac{|P_{xy}|^2}{P_{xx}P_{yy}} \tag{6.1}$$

where P_{xy} is the cross power between the probes and P_{xx} and P_{yy} are auto-power spectral densities. Phase shifts are then calculated for coherent activity. The phase shift $\Delta\phi^{i,j}_{\text{phase}}$ is defined as the the phase angle between probe i and probe $j > i$

$$\Delta\phi^{xy}_{\text{phase}} = \tan^{-1}\left(\frac{\text{Im}(P_x \cdot P_y^*)}{\text{Re}(P_x \cdot P_y^*)}\right) \tag{6.2}$$

where P_x and P_y are short time Fourier transforms (STFT) of the magnetic fluctuation time traces and the superscript * indicates a complex conjugate. Defining the difference in toroidal location of probes as $\Delta\phi^{xy}_{\text{probe}} = \phi^{x}_{\text{probe}} - \phi^{y}_{\text{probe}}$ the toroidal mode number can be found using linear regression with the equation

$$\Delta\phi_{\text{probe}} = n\Delta\phi_{\text{phase}} \tag{6.3}$$

over all combinations of probe x and probe $y > x$. The use of linear regression provides r^2 as a measure of goodness-of-fit. Mode numbers with $r^2 > 0.8$ are considered to be reasonably accurate. Linear regression results for the instability case 172348 are shown in Fig. 6.3 for three coherent modes: two at low frequency (< 100 kHz) and one at high frequency (> 100 kHz). Full mode number calculations within a time and frequency window are shown in Fig. 6.4 (top row).

Alfvén continuum calculations indicate that the high-frequency mode resides in a gap outside the mid-radius. Gaps in the Alfvén continuum are calculated using the STELLGAP code [28]. STELLGAP results for both cases are shown in Fig. 6.4 (bottom row). It should be noted that the sign of calculated mode numbers from magnetic probe measurements corresponds to the toroidal direction with mode numbers increasing in the counter-clockwise

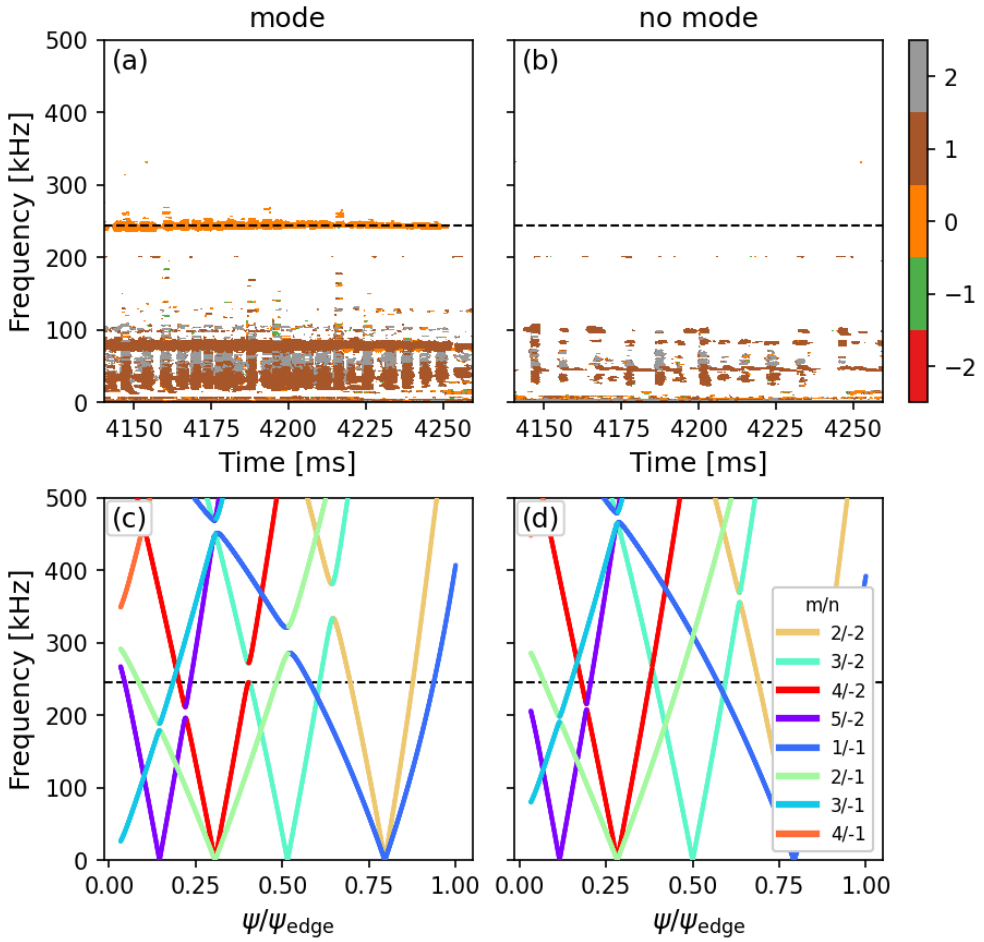

Figure 6.4: Calculated toroidal mode number (top row) and Alfvén continuum calculations by STELLGAP (bottom row). The horizontal dashed line marks the 240 kHz mode. Left column is discharge 172348 where the mode is observed. Right column is discharge 172352 where no mode is observed.

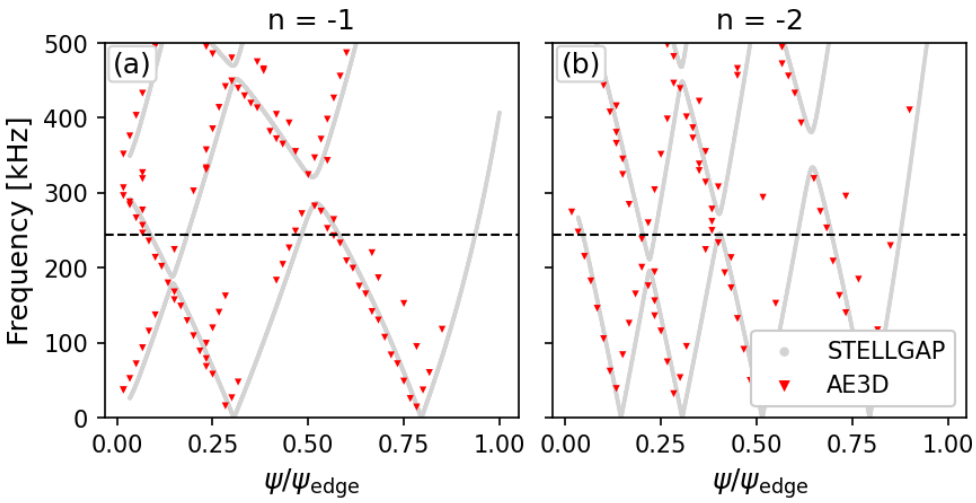

Figure 6.5: Alfvén continuum calculations by STELLGAP (light gray) and AE3D (red). Radial locations of the AE3D values correspond to the peak in the calculated eigenfunctions. The horizontal dashed line marks the 240 kHz mode.

(CCW) direction. Toroidal mode numbers in the continuum calculated by STELLGAP use the opposite convention for CCW-B_t cases. For CCW-B_t LHD cases, an observed mode number of $n = +1$ corresponds to a STELLGAP mode number of n = -1. Low frequency ($<$ 100 kHz) $n = 1$ and 2 modes are observed in both cases but the activity is much more apparent in the instability case with higher amplitudes (see Fig. 6.1). These modes cross the continuum and do not exist within a gap. Magnetic probe measurements indicate that the 240 kHz mode in the instability case is an $n = 0$ mode. However, this mode appears in an n = -2 gap with radial extent calculated by STELLGAP (Fig. 6.4(c)). The gap appears due to poloidal coupling between $m = 3$ and 4. No gapes are found for the case without the 240 kHz mode (Fig. 6.4(d)).

Although the 240 kHz mode is observed to have a mode number of $n = 0$, calculations of the continuum and eigenfunctions shows n = -2 modes residing in the associated gap. Figure 6.5 shows the Alfvén continuum calculated by STELLGAP for the n = -1 and -2 modes with an overlay of the frequencies calculated by the AE3D code. AE3D calculates the radial structure of the eigenmode [69]. Red markers in Fig. 6.5 show the radial location of the peak

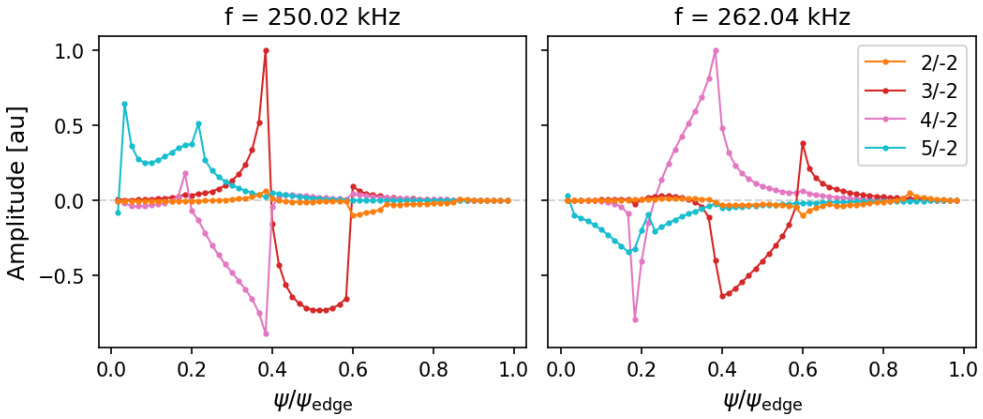

Figure 6.6: Radial eigenfunctions calculated by AE3D for 172348 at $t = 4200$ ms.

of calculated eigenmodes along with their frequency. Two TAEs appear in a gap created by poloidal mode coupling of the m/n = 3/-2 and 4/-2 modes. Radial structures of the two modes calculated by AE3D are shown in Fig. 6.6. Both calculated eigenmodes show coupled m = 3, 4 modes with odd parity. The lower frequency mode (f = 250.02 kHz) intersects the $n = -2$ continuum above $\psi/\psi_{\text{edge}} = 0.4$ where it appears to experience continuum damping. The higher frequency mode (f = 262.04 kHz) extends past $\psi/\psi_{\text{edge}} = 0.4$ until $\psi/\psi_{\text{edge}} = 0.6$ where it appears to experience continuum damping. Therefore, resonance with fast ions is expected in the range of ψ/ψ_{edge} = 0.4-0.6 or $\sqrt{\psi/\psi_{\text{edge}}}$ = 0.6-0.8.

Calculations of the Alfvén speed profile suggests that the primary resonance condition for TAEs is not satisfied but v_A is above the sideband resonance condition. Plasma profiles for both cases are shown in Fig. 6.7. Electron density profiles differ by approximately 12% at the mid-radius ($\sqrt{\psi/\psi_{\text{edge}}} = 0.5$) while electron temperature and slowing down profiles differ by less than 10% across the volume. Similarly, ion density profiles differ by approximately 10% at the mid-radius while ion temperature profiles differ by less than 10% across the volume. Alfvén speed v_A profiles are calculated using ion density measurements for the main deuterium species as well as impurity hydrogen, helium, and carbon species. Figure 6.8 shows the thermal ion and impurity profiles. The magnetic field contribution to v_A is calculated using flux surface-averaged field $\langle B \rangle_{\theta,\phi}$. $\langle B \rangle_{\theta,\phi}$ values are nearly identical for both cases.

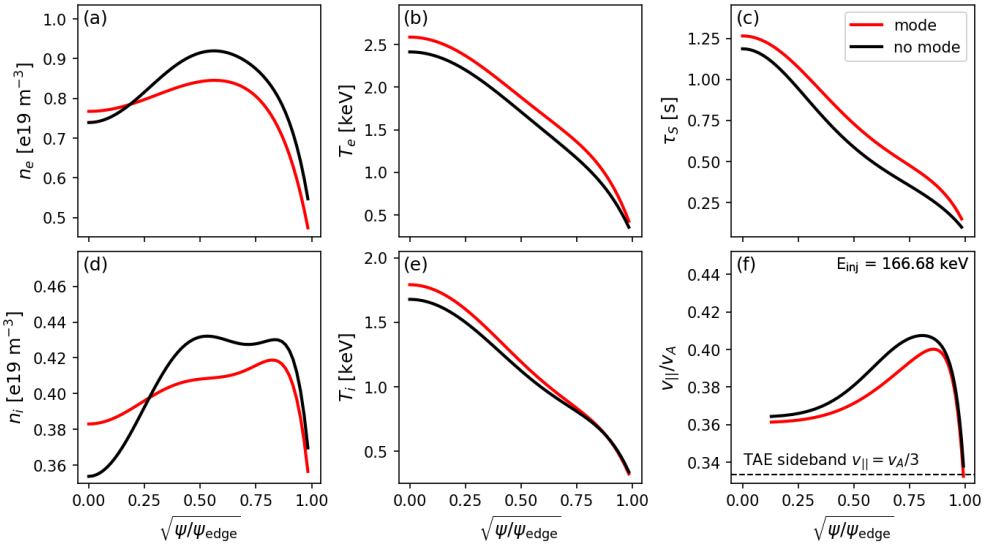

Figure 6.7: Plasma profiles for high-field cases showing (a) electron density, (b) electron temperature, (c) Spitzer slowing-down time, (d) ion density, (e) ion temperature, and (f) speed of a passing fast ion at the NB3 injection energy divided by the Alfvén speed. The horizontal dashed line indicates the TAE sideband resonance condition $v_{||} = v_A/3$.

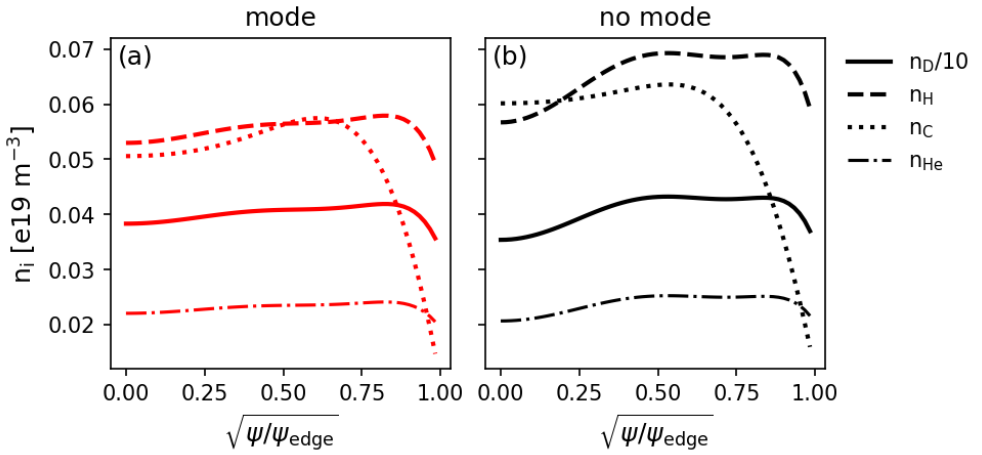

Figure 6.8: Thermal ion profiles for (a) 172348 and (b) 172352. Solid lines indicate main ion profiles divided by 10. Dashed lines indicate hydrogen profiles. Dotted lines indicate carbon profiles. Dash-dotted lines indicate helium profiles.

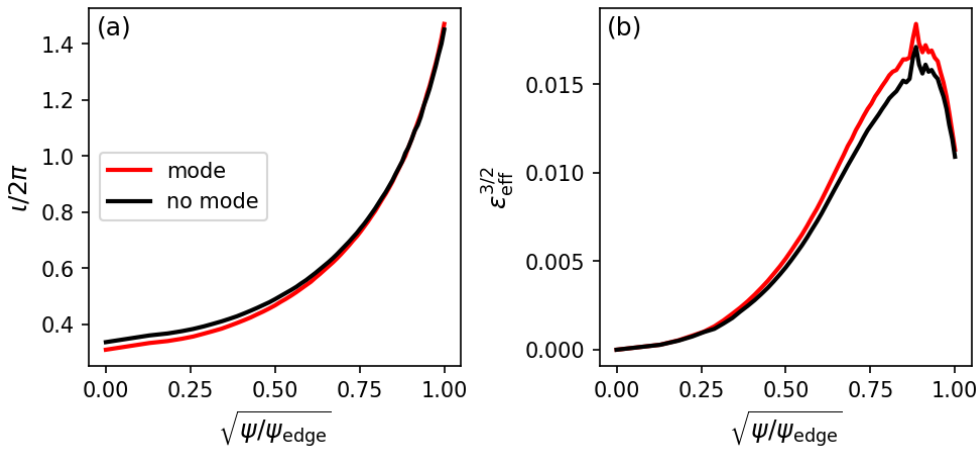

Figure 6.9: Iota profile and effective helicity $\varepsilon_{\text{eff}}^{3/2}$ for the high-field cases.

Assuming quasineutrality in a deuterium plasma with helium and carbon impurities, Alfvén speed scales with electron density $v_A \propto n_e^{-1/2}$ so a 12% difference in n_e should correspond to a 6% change in $\mathrm{v_A}$. This is because the charge-to-mass ratio for the three ion species are all $A_i/Z_i = 2$ and they contribute evenly to the mass density Carbon is assumed to be the main impurity but hydrogen density measurements are comparable to carbon density measurements (Fig. 6.8). The predicted $\mathrm{v_A}$ profiles differ by approximately 5% around the mid-radius (Fig. 6.7(f)). The $\mathrm{v_A}$ profiles in Fig. 6.7(f) show the resonance with a passing fast ion that is near the heating beam injection energy. Recalling resonance conditions for AEs in eq. 1.16, the fundamental resonance for TAEs ($\mu = 1$, $\nu = 0$) requires $v_{||}/v_A = 1$ but the profile peaks at $v_{||}/v_A = 0.41$. However, the sideband resonance condition for TAEs $v_{||}/v_A \geq 1/3$ is satisfied which suggests that the observed mode may be a TAE driven by sideband excitation.

Rotational transform and effective helicity profiles for the high-field cases are similar to the quiescent cases as expected. Figure 6.9 shows $\iota/2\pi$ and $\varepsilon_{\text{eff}}^{3/2}$ profiles for the high-field cases. The main difference in plasma conditions between the present study and the quiescent study is due to the increase in heating beam power and resultant MHD activity. The magnetic

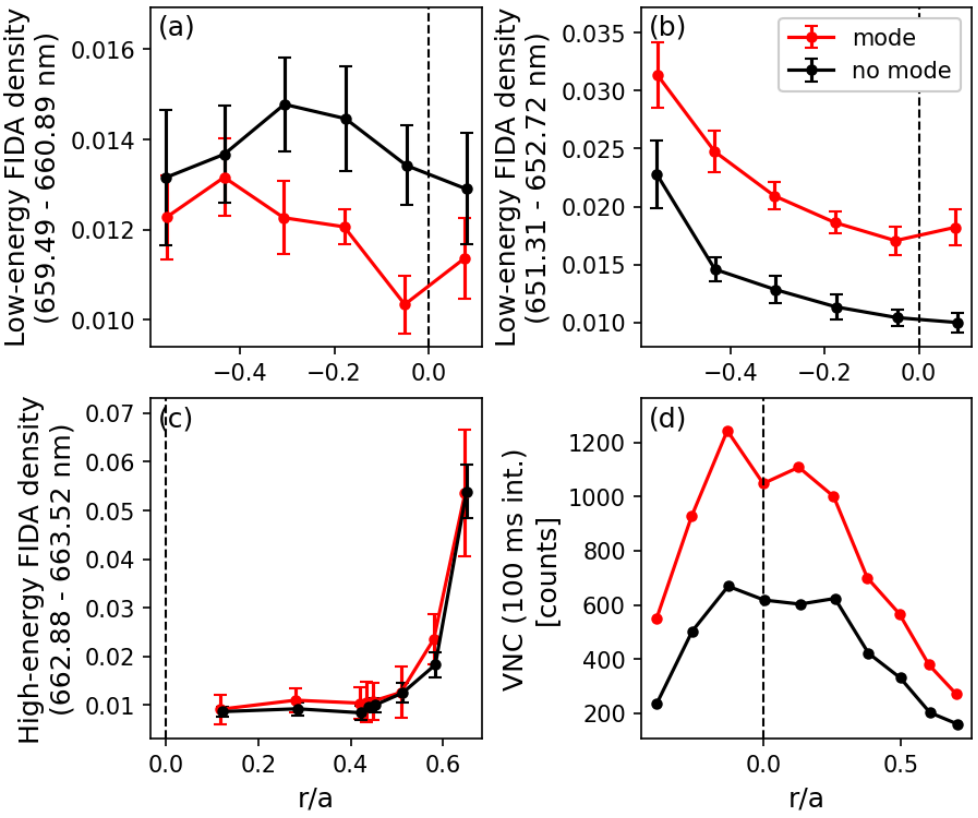

Figure 6.10: Low-energy FIDA density profiles for (a) co-passing fast ions and (b) counter-passing fast ions along with (c) high-energy FIDA density and (d) VNC for high-field cases at $t = 4200$ ms.

field configurations are identical to the quiescent $R_{ax} = 3.6$ m case so $\iota/2\pi(\rho = 0.5) = 0.5$ and $\varepsilon_{\text{eff}}^{3/2}(\rho = 0.5) = 0.005$ are identical to the previously observed values (Fig. 5.2).

Fast ion measurements show a decrease in the low-energy FIDA density when the instability is present in the high-field case. Figure 6.10 shows FIDA density and VNC measurements for both high-field cases with and without the instability. Low-energy FIDA density for red-shifted signal corresponding to co-passing fast ions populated by NB3 with energies just below the critical energy should be similar due to the identical NB3 heating power and similar slowing down times. However, a decrease in signal for the instability case suggests that fast ions are redistributed from the core, possibly due to the mode activity. Low-energy FIDA density for blue-shifted signal $\lambda < 656.1$ nm corresponds to counter-passing fast ions

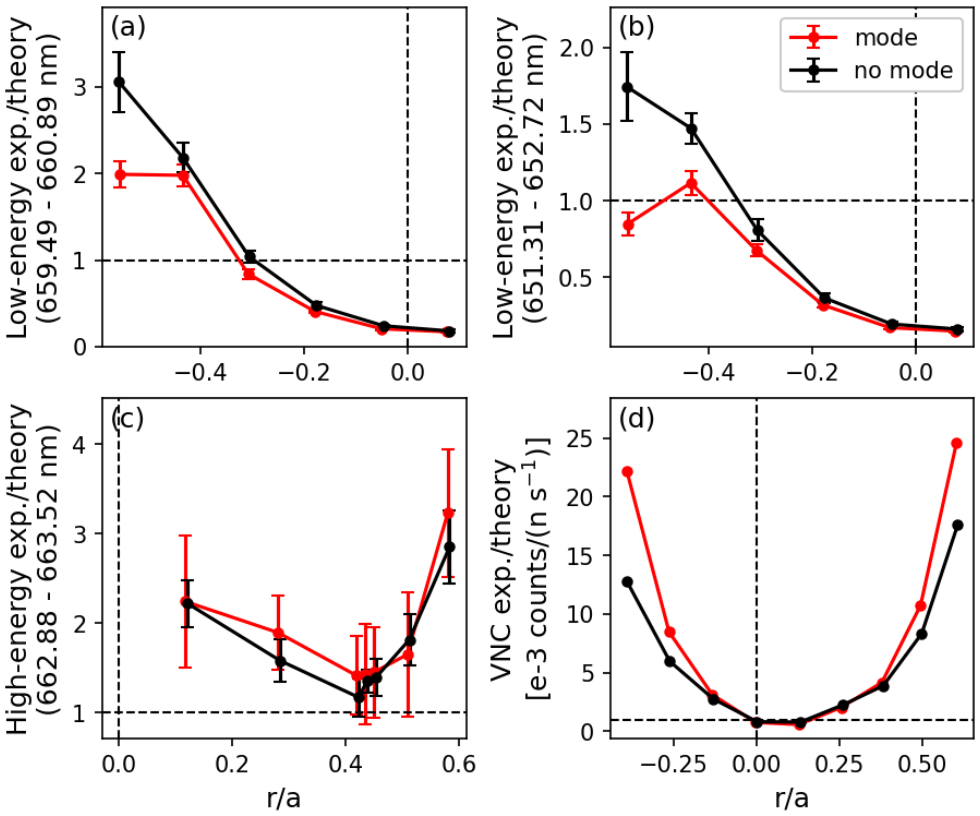

Figure 6.11: Experiment/theory ratios for profiles in Fig. 6.10.

populated by NB2. Higher signal for the full-power NB2 case indicates that more counter-passing fast ions are being populated, which is expected. High-energy FIDA density for red-shifted signal $\lambda > 656.1$ nm corresponds to co-passing fast ions populated by NB3 that are near the 160 keV injection energy. Nearly identical profiles are expected since the NB3 heating powers are identical. VNC profiles, similar to global neutron emission, increase with total heating power so the higher signal with full-power NB2 is expected.

Effects of the observed instability on the fast ion distribution is inferred through forward-modeling with FIDASIM. Experiment/theory ratios are shown in Fig. 6.11 using Goldston distributions in FIDASIM. Instability effects are not included in the Goldston model so divergence between the two cases implies additional transport of fast ions due to the mode. However, FIDA density and VNC profiles are virtually identical between both cases within the mid-radius. Similar to the quiescent study in Ch. 5, the best agreement between ob-

served and simulated low-energy FIDA density is just inside the mid-radius $0.2 < \mathrm{r/a} < 0.4$. Here, the normalized minor radius r/a is equivalent to $\sqrt{\psi/\psi_{\mathrm{edge}}}$ with an additional signed component that corresponds to the inboard (-1) and outboard (+1) side. Low-energy FIDA densities and VNC profiles start to diverge at the mid-radius where there is the largest difference in thermal profiles. Agreement of the experiment/theory ratios between both cases despite the decrease in low-energy FIDA density in Fig. 6.10(a) suggests that the decreased signal is independent of instability effects. Due to identical NB3 heating powers, the birth profile of co-passing fast ions between the two cases should be nearly identical. This is apparent in the identical high-energy FIDA density profiles (Fig. 6.10(c)) that measure fast ions just below the injection energy. At such high energies, fast ions mainly slow down on electrons which have similar profiles with and without the instability (difference of $\sim$ 12%). Low-energy FIDA density measures fast ions below the critical energy which experience non-negligible slowing down on thermal ions. This means that there is a non-negligible contribution to the FIDA density profiles due to the thermal ion profiles. Although the NB3-born co-passing fast ions have similar birth profiles, the cumulative differences in thermal profiles results in the decreased signal in Fig. 6.10(a). This is confirmed by the nearly identical experiment/theory ratios in Fig. 6.11(a) since the Goldston model used with FIDASIM does not account for AE activity but it does include slowing down due to thermal profiles. The simulated FIDA density for the instability case is reduced by the same amount as the measured profile. This can be extended to the blue-shifted signal in Fig. 6.10 and Fig. 6.11. However, the blue-shifted signal is proportional to the NB2 heating power which populates the counter-passing fast ion orbits. The instability case has higher NB2 power resulting in an overall higher counter-passing fast ion population measured by the blue-shifted low-energy FIDA density.

The lack of transport due to AEs in low-energy FIDA density profiles is confirmed with comparison to profiles from the quiescent study. Figure 6.12 shows measured, FIDASIM, and experiment/theory profiles for low-energy and high-energy FIDA density as well as

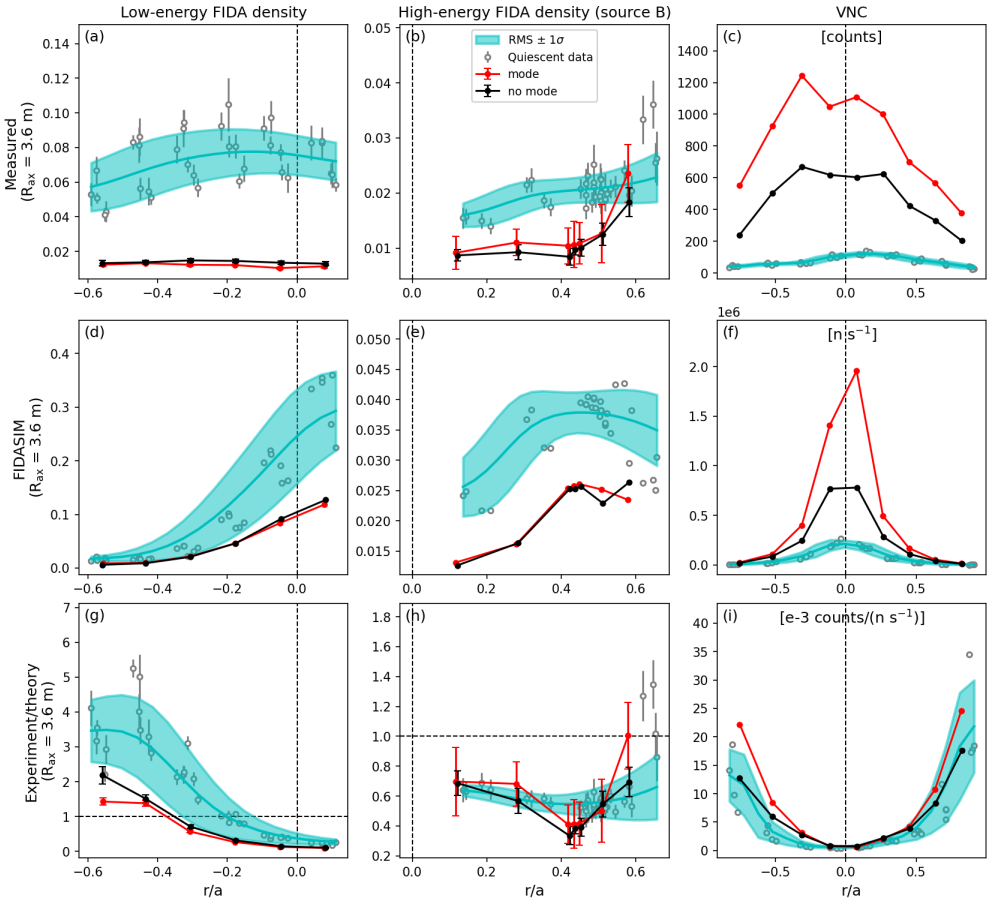

Figure 6.12: (left column) Low-energy FIDA density, (middle column) high-energy FIDA density, and (right column) VNC values from (top row) measurements, (middle row) FIDASIM, and (bottom row) measured/FIDASIM. Low-energy FIDA density values are integrated over the red-shifted region (659.49 - 660.89 nm). Profiles for 172348 and 172352 are shown in red and black, respectively. Open gray circle markers indicate the profile values for the quiescent cases. Error bars indicate one standard deviation. The cyan shaded region indicates one standard deviation around the root-mean-square (RMS) of the quiescent cases.

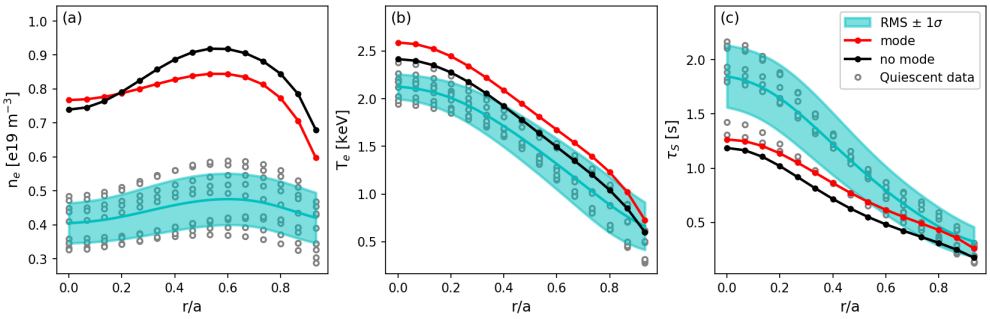

Figure 6.13: (a) Electron density, (b) temperature, and (c) slowing-down time profiles for the high-field cases compared to the $R_{ax} = 3.6$ m quiescent cases. Profiles for 172348 and 172352 are shown in red and black, respectively. Open gray circle markers indicate the profile values for the quiescent cases. The cyan shaded region indicates one standard deviation around the root-mean-square (RMS) of the quiescent cases.

VNC. Only red-shifted signals are considered since blue-shifted signals were not used in the quiescent study. Low-energy FIDA density measurements and FIDASIM results are lower for both high-field cases in the present study compared to the quiescent cases. Some decrease in measured FIDA density is expected due to higher electron densities. Figure 6.13 shows the electron density, temperature, and Spitzer slowing-down times for the high-field cases compared to the quiescent cases. Density profiles are considerably higher with a 50% increase compared to the quiescent cases but temperature profiles are similar with only a $\sim$ 15% increase near the core. Slowing-down times are comparable with a 20% decrease at the core and little to no change from the mid-radius to the edge. Since both measured and FIDASIM values are decreased proportionately (Fig. 6.12 left column), experiment/theory values are similar to the quiescent cases. High-energy FIDA density measurements and simulation results (Fig. 6.12 middle column) are also decreased proportionately and experiment/theory values are consistent with the quiescent cases. Similarly, measured and FIDASIM VNC profiles are increased proportionately (Fig. 6.12 right column) and experiment/theory values are similar. The largest disagreement in VNC profiles occurs outside the mid-radius for both the inboard and outboard side. This is attributed to the increase of measured VNC values outside the mid-radius due to neutrons reflected from the vessel wall which was observed in the TFTR tokamak using a similar neutron collimation system [61]. Experiment/theory

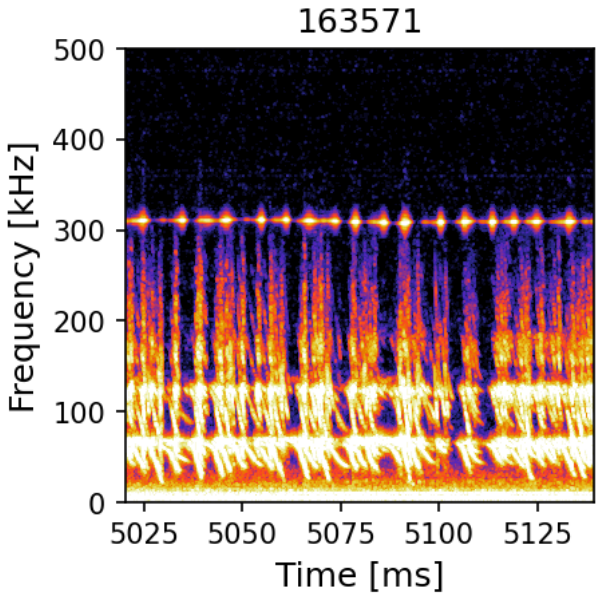

Figure 6.14: Power spectral density for the low-field case with observed modes at 50 kHz, 120 kHz, and 310 kHz.

values for low-energy FIDA density and VNC agree with the quiescent cases within reason which suggests that transport due to the AE is not observed by diagnostics.

6.2 Low-field case

Instabilities are also observed at low-field where the lower Alfvén speed approaches the fundamental TAE resonance condition $v_{||} = v_A$. Figure 6.14 shows the power spectral density of magnetic fluctuations for discharge 163571. Rapid frequency chirping is observed around 60 kHz and 120 kHz along with bursting activity just above 300 kHz. Similar to the high field case, this discharge has a magnetic configuration with $R_{ax} = 3.6$ m, CCW-B_t, and deuterium beams into deuterium plasma but the on-axis B_t is 1.0 T. In addition to NB3 and NB2, NB1 is also injected into the plasma with Fig. 6.15(a) showing NB1 + NB3 injected power. NB2 injected power is 1.0 MW (Fig. 6.15(b)), similar to the high-field case with half-power NB2 where no activity is observed. Global neutron emission rate (Fig. 6.15(c)) is only 1×10^{14}

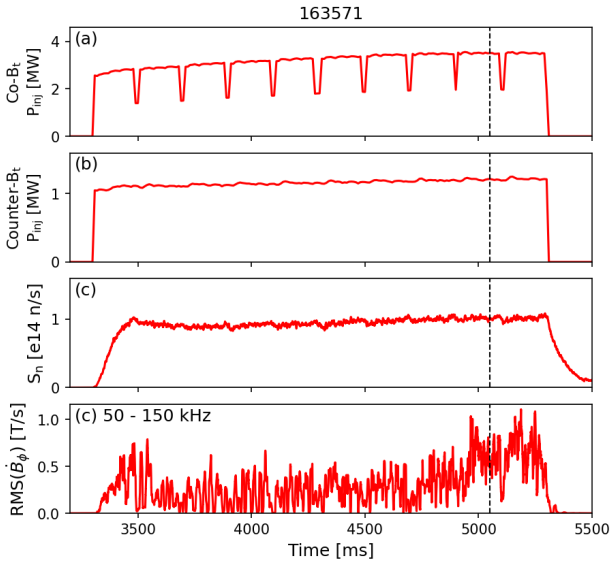

Figure 6.15: Time traces for the low-field case showing (a) co-B_t injected NBI power, (b) counter-B_t injected NBI power, (c) global neutron emission rate, and (d) root-mean-square (RMS) of toroidal magnetic field fluctuations in the 50-150 kHz range.

n/s, which is lower than the average neutron emission rate for both high-field cases with 2×10^{14} n/s and 4×10^{14} n/s for the half-power and full-power NB2 cases, respectively.

Toroidal mode number calculations show multiple mode numbers that differ from continuum calculations. Figure 6.16 shows toroidal mode number calculations and the Alfvén continuum calculated by STELLGAP. A gap is found at 100 kHz for n = -1 and -2 just outside the mid-radius (r/a = 0.5 $\rightarrow$ $\psi/\psi_{\text{edge}} = 0.25$). However, calculations from measurements show that the observed activity has a mode number of $n = 2$ at 100 kHz and $n = 1$ at 50 kHz. The 300 kHz mode, with an observed mode number of $n = -1$ or $n = 0$, appears to intersect the continuum and does not reside in a gap. Eigenvalues calculated by AE3D are shown in Fig. 6.17 with eigenfunctions appearing within the $m/n = 1/-1$ and $m/n = 3/-2$ gaps. Radial structures for these eigenfunctions calculated using AE3D are shown in Fig. 6.18. An $n = -1$ TAE is found with $m = 1, 2$ coupling and even parity. An $n = -2$ mode is also found with some coupling between $m = 3$ and 4 and even parity. However, the poloidal mode coupling of the $n = -2$ mode appears weak due to little overlap in the radial structures and the mode may not be a TAE. Nevertheless, the $n = -2$ mode appears to agree with the

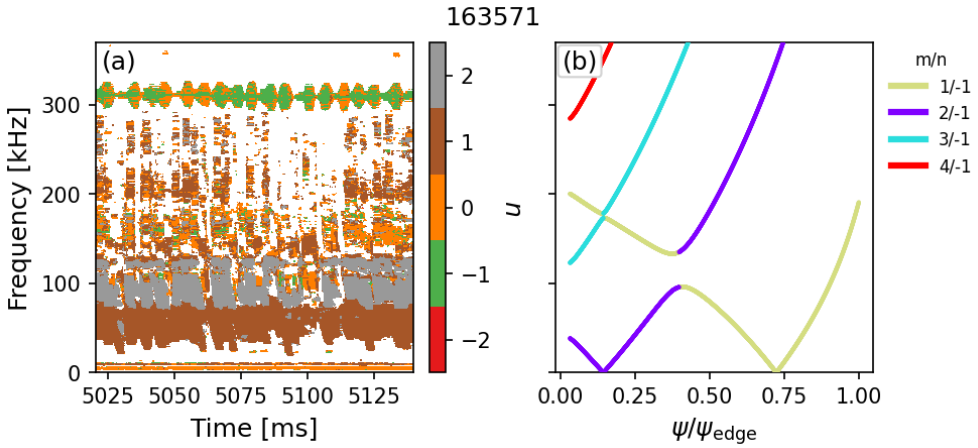

Figure 6.16: (a) Calculated toroidal mode numbers and (b) Alfvén continuum calculated by STELLGAP.

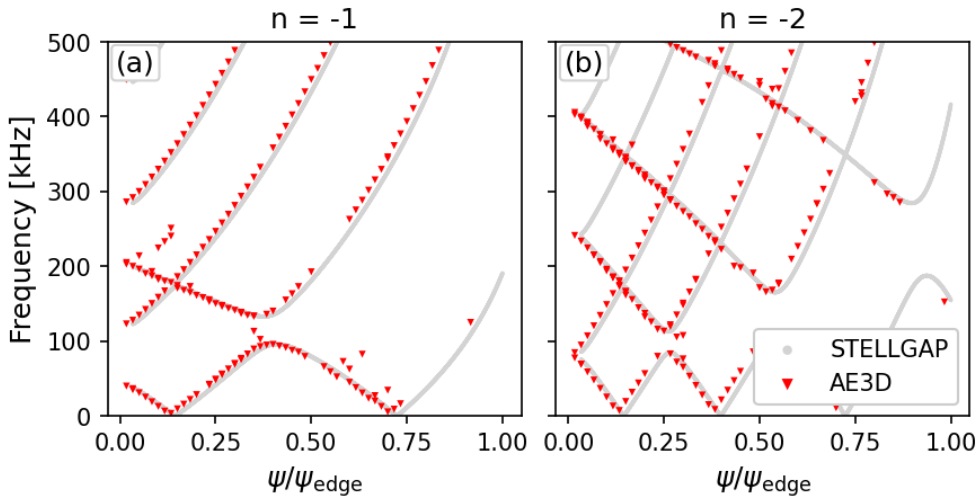

Figure 6.17: Alfvén continuum calculations by STELLGAP (light gray) and AE3D (red). Radial locations of the AE3D values correspond to the peak in the calculated eigenfunctions.

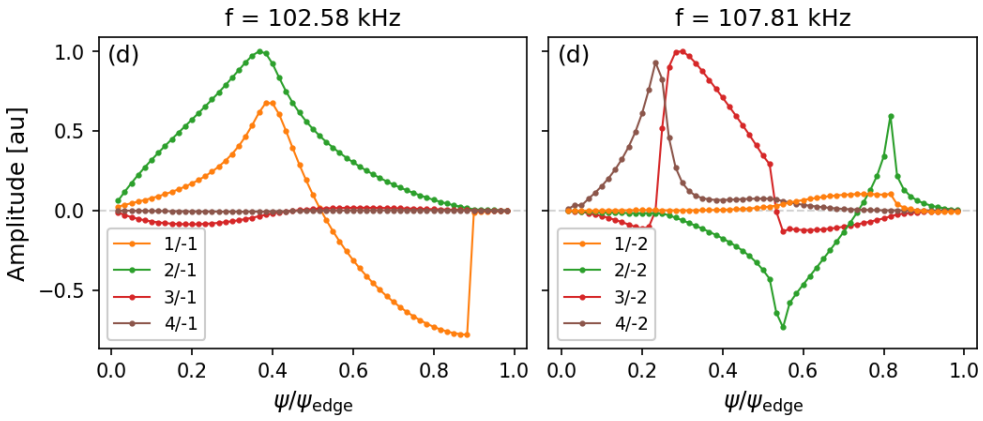

Figure 6.18: Radial eigenfunctions calculated by AE3D for 163571 at $t = 5000$ ms.

observed mode number $n = 2$ for the 100 kHz mode when recalling the opposite signs due to the different conventions.

Plasma profiles for the low-field case are shown in Fig. 6.19. Maximum electron density values $\max(n_e) \sim 0.43 \times 10^{19}$ m^{-3} and core electron temperature values $T_{e0} \sim 1.2$ keV are approximately half of the values observed in the high-field cases. Maximum thermal ion density for the main deuterium species $\max(n_D) \sim 0.35 \times 10^{19}$ m^{-3} are around 15% less than the high-field cases with ion densities around $\sim 0.42 \times 10^{19}$ m^{-3}. Thermal ion and impurity density profiles are shown in Fig. 6.20. In contrast to the high-field cases, hydrogen density in the low-field case is considerably higher than carbon density. Slowing-down time τ_S is approximately 20% less for the low-field case with $\tau_S \sim 1.0$ s on axis compared to $\tau_S \sim 1.25$ s for the high-field cases.

While the toroidal field strength is lower, $\iota/2\pi$ is similar to the high-field cases which corresponds to a higher poloidal field. Figure 6.21 shows the $\iota/2\pi$ and $\varepsilon_{\text{eff}}^{3/2}$ profiles. The toroidal field strength is considerably lower (1.0 T) in the present study compared to the high-field cases and quiescent study which use the same toroidal field strength for the $R_{ax} = 3.6$ m configuration (2.75 T). Rotational transform $\iota/2\pi$ is approximated by the toroidal field B_t and poloidal field B_p as $\iota/2\pi \propto B_p/B_t$. Since B_t is lower and $\iota/2\pi\,(\rho = 0.5) = 0.5$ is identical

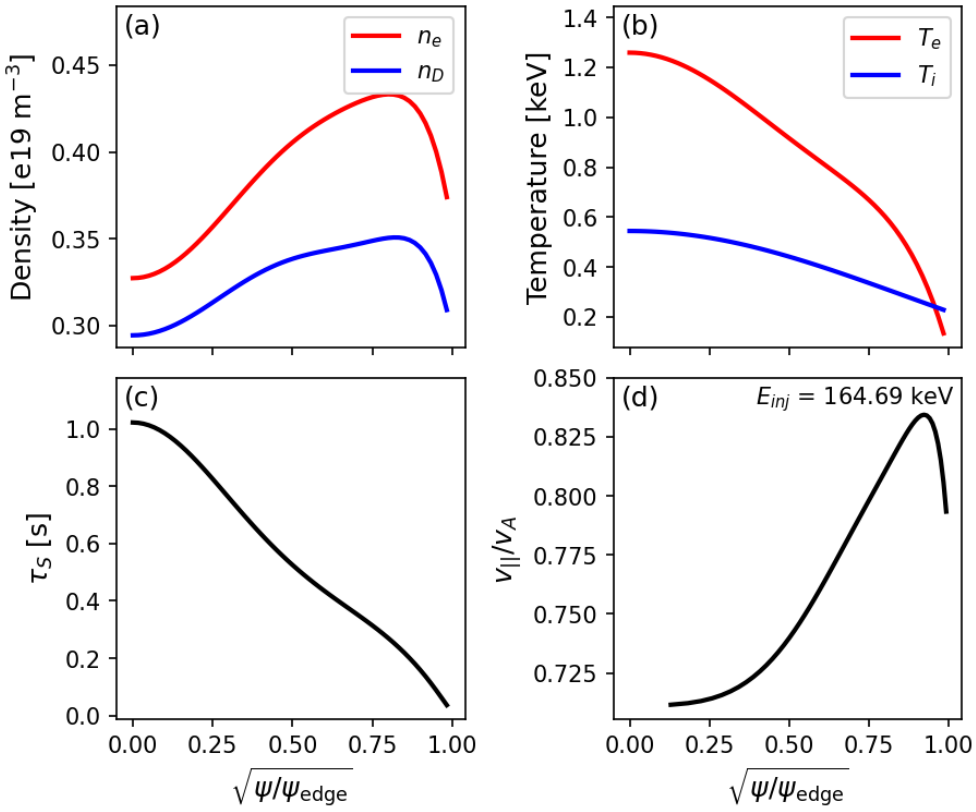

Figure 6.19: Plasma profiles for the low-field case showing (a) electron and ion densities, (b) electron and ion temperatures, (c) Spitzer slowing-down time, and (d) speed of a fast ion at the NB3 injection energy divided by the Alfvén speed.

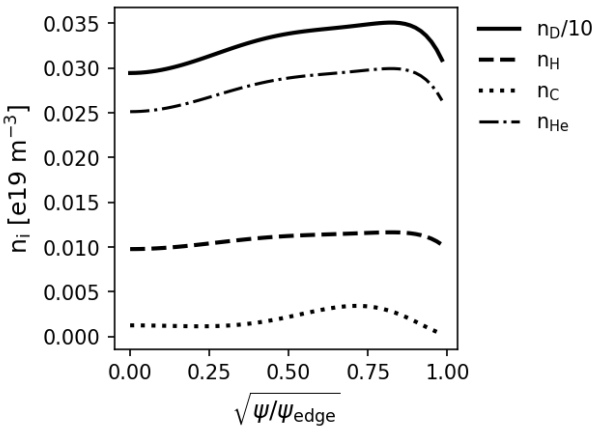

Figure 6.20: Thermal ion density profiles for deuterium divided by 10 (solid), hydrogen (dashed), carbon (dotted), and helium (dash-dotted).

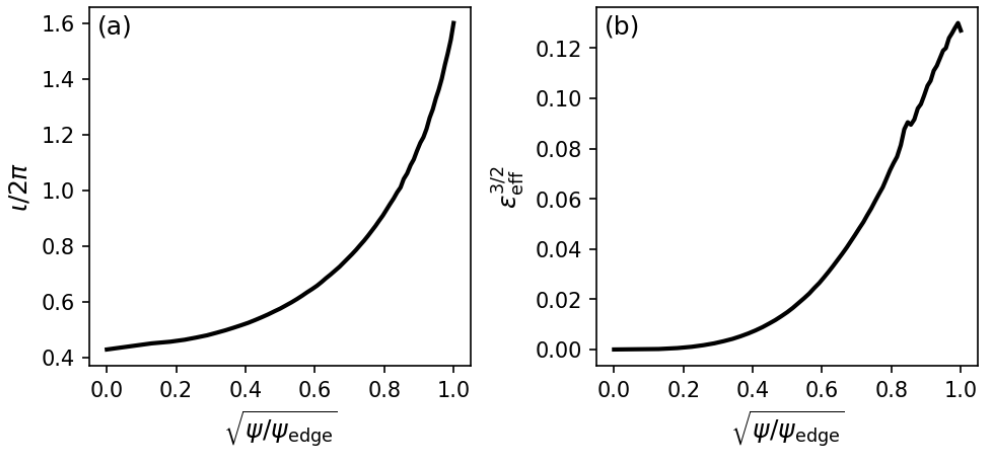

Figure 6.21: (a) Rotational transform $\iota/2\pi$ and (b) effective helicity $\varepsilon_{\text{eff}}^{3/2}$ profiles for the low-field case.

to the quiescent and high-field studies, B_p must be lower. Drift surfaces are dependent on B_p so some disagreement in fast ion measurements with previous results is expected. The changes in drift orbits and reduced neoclassical confinement are quantified by the increased effective helical ripple $\varepsilon_{\text{eff}}^{3/2}(\rho = 0.5) = 0.015$ which is higher than the quiescent $R_{ax} = 3.7$ m case.

Measured FIDA density is comparable to the high-field cases while VNC values are reduced by an order of magnitude. Disagreement in fast ion measurements with the high-field cases is expected due to different B_p. Figure 6.22 (top row) shows measured profiles for red- and blue-shifted FIDA density as well as VNC. Red-shifted FIDA density values inside the mid-radius (r/a$<$ 0.5) are around 0.015, similar to 0.012 and 0.014 for the high-field cases with and without instabilities. Blue-shifted FIDA density values inside the mid-radius are around 0.01 which is similar to the high-field case without instabilities. Both the present study and the high-field case without instabilities use only 1 MW of injected NB2 power. The VNC profile has a maximum value of $\sim$ 110 normalized counts. In this case normalized counts is the ratio of 1 measured count to 1000 neutrons per second calculated by FIDASIM. Calibrated values for measured VNC are not available so only a relative comparison can be made to the high-field VNC measurements. VNC profiles in the high-field case are moderately peaked

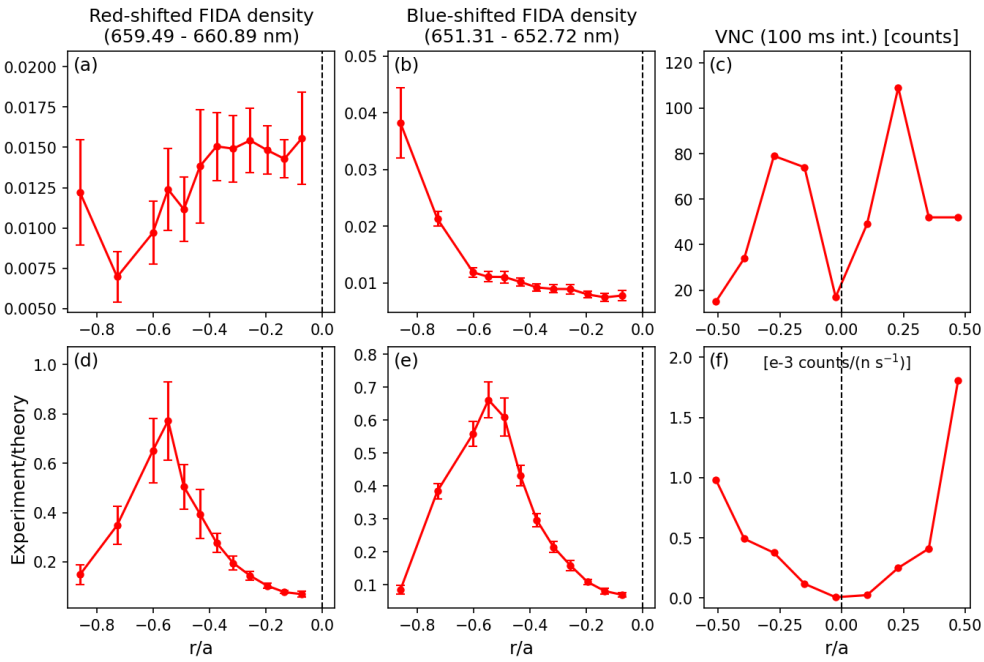

Figure 6.22: Measured profiles (top row) and experiment/theory values (bottom row) for 163571 at $t = 5000$ ms. (a) Low-energy FIDA density for co-passing fast ions, (b) low-energy FIDA density for counter-passing fast ions, (c) measured VNC counts, (d) experiment/theory of low-energy FIDA density (co-passing), (e) experiment/theory of low-energy FIDA density (counter-passing), (f) experiment/theory of VNC.

towards the core with approximately 2-3x increase in values from the mid-radius to the core. However, the VNC profile for the low-field case shows a hollow profile with two peaks at r/ax = ± 0.25.

Experiment/theory ratios using FIDASIM with a Goldston distribution (Fig. 6.22 bottom row) show that the predicted FIDA densities for co- and counter-passing fast ions are consistently overestimating measurements. The predicted red-shifted FIDA density (Fig. 6.22(d)) and blue-shifted FIDA density (Fig. 6.22(e)) are close to the measured values near the mid-radius, similar to the high-field cases and the comparison in section 5.2.2. However, experiment/theory ratios for both FIDA density profiles never cross unity and values decrease towards the plasma edge. Due to the lack of radial transport in the Goldston model, experiment/theory values above 1 are expected outside the mid-radius. This expected behavior is seen in both the high-field and quiescent cases. Values below 1 seen in Fig. 6.22(d, e) suggests that the fast ion density outside the mid-radius is lower than the ideal distribution predicted by the Goldston model. This appears to affect both co- and counter-passing fast ions since the effect is present in both red- and blue-shifted signals. A relative comparison of the experiment/theory VNC values between the low-field and high-field cases show similar convex profiles. Since measured VNC values are not calibrated, an absolute comparison of VNC values is unavailable.

Experiment/theory ratios for FIDA density and VNC suggest a decrease in fast ions compared to the quiescent study Figure 6.23 shows measured, FIDASIM, and experiment/theory values for low-energy FIDA density, high-energy FIDA density and VNC. Low-energy FIDA density measurements are considerably lower in the low-field case. Figure 6.24 shows the electron density, temperature, and slowing-down times for the present study compared to the quiescent study. The electron density profile are similar to the quiescent profiles but the temperature is lower in the core resulting in shorter slowing-down time. Shorter slowing-down time explains some of the decrease in FIDA density measurements in Fig. 6.23(a).

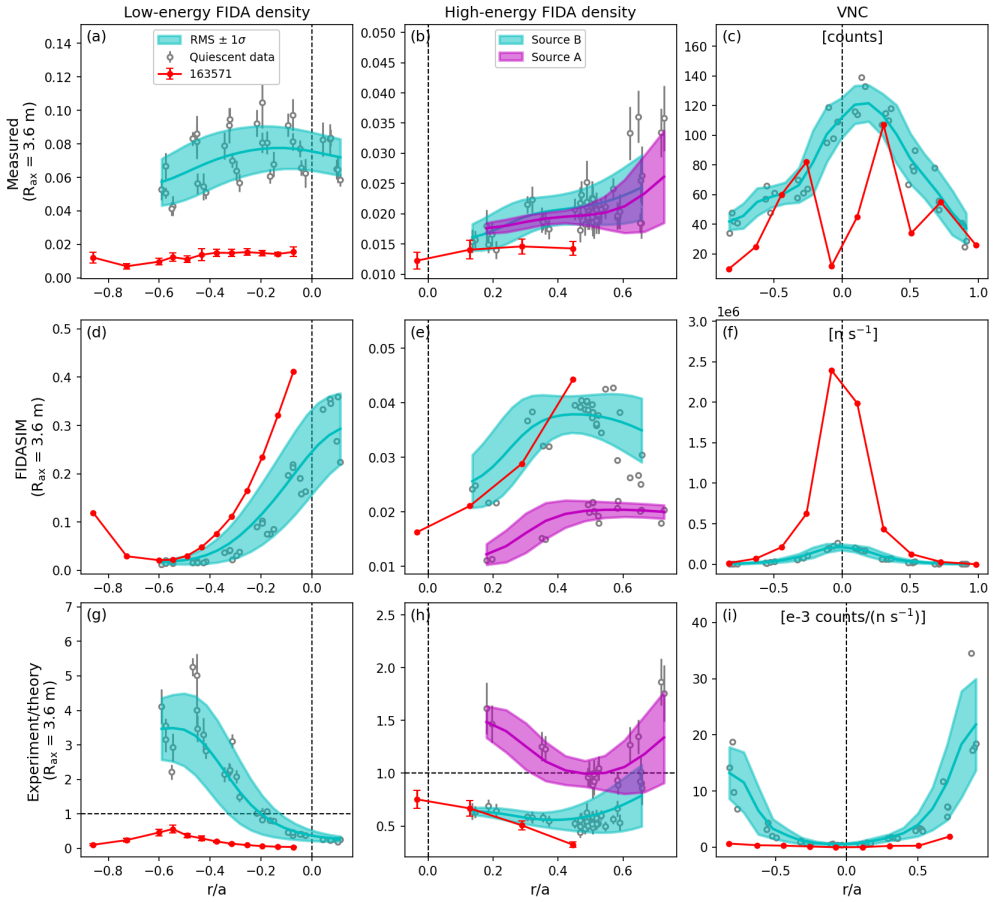

Figure 6.23: (left column) Low-energy FIDA density, high-energy FIDA density (middle column), and (right column) VNC values for (top row) measurements, (middle row) FIDASIM, and (bottom row) measured/FIDASIM. Profiles for 163571 are shown in red. Low-energy FIDA density values are integrated over the red-shifted region (659.49 - 660.89 nm). High-energy FIDA density for the quiescent study are shown for both source A (magenta) and source B (cyan). Open gray circle markers indicate the profile values for the quiescent cases. Error bars indicate one standard deviation. The cyan shaded region indicates one standard deviation around the root-mean-square (RMS) of the quiescent cases.

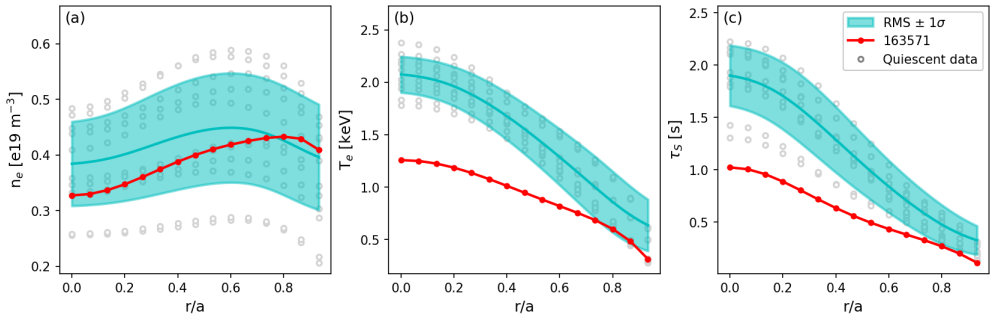

Figure 6.24: (a) Electron density, (b) temperature, and (c) slowing-down time profiles for the high-field cases compared to the $R_{ax} = 3.6$ m quiescent cases. Profiles for 163571 are shown in red. Open gray circle markers indicate the profile values for the quiescent cases. The cyan shaded region indicates one standard deviation around the root-mean-square (RMS) of the quiescent cases.

However, FIDASIM predicts FIDA density to be virtually identical to the quiescent cases (Fig. 6.23(d)). This results in a considerable decrease in experiment/theory (Fig. 6.23(g)). Since the Goldston model does not include AE-induced transport and neoclassical drifts that decreases the fast ion measurements, the observed decrease in experiment/theory is expected. Conversely, the high-energy FIDA density values are not very different from the quiescent source B cases. It should be noted that the low-field case uses both sources for NB3. Measured values are slightly lower than quiescent measurements while FIDASIM values are similar to source B values and higher than source A values. Experiment/theory values for high-energy FIDA density are just below source B values and considerably decreased from source A values. A decrease in experiment/theory for VNC values is also observed due to a decrease in measured values. The low-field cases are heated by 3 NBI sources which is 3x more heating power than the quiescent cases. This should correspond to an increase in VNC, as predicted by FIDASIM (Fig. 6.23(e)). However, the measured VNC values are similar to the quiescent values (Fig. 6.23(b)) which are significantly lower than measured VNC in the high-field case which also uses 3 NBI sources (Fig. 6.12(c)). Similar to FIDA density, the experiment/theory values are decreased from the quiescent cases. Overall, a decrease in fast ion confinement is observed in the experiment despite a significant increase in heating

power. The decrease is attributed to (a) transport due to AE activity and (b) neoclassical transport due to larger drift orbits.

Chapter 7

Conclusion and future work

7.1 Summary

Fast ion behavior is measured using fast ion diagnostics to interrogate the phase-space distribution. A novel cold Dα filter method is installed on a prototype spectrometer and tested to confirm a full-width half-maximum of 1 nm for the filter notch. Fast ion measurements are collected from multiple experiments conducted at the Large Helical Device. A new sightline is confirmed to isolate signals of fast ions near the neutral beam injection energy. Parametric studies are conducted of fast ion measurements to evaluate dependencies on beam and plasma parameters along with changes in neoclassical confinement due to the inward-shifted configuration. Instability measurements are analyzed to identify Alfvén eigenmodes and study their interaction with fast ions.

Experimental results confirm the predictions that FIDA sightlines nearly tangential to the active beamline can be used to measure high-energy fast ions. The study in [43] used an ideal geometry for the high-energy view with a 180 keV NNBI heated plasma. This results in a predicted FIDA peak corresponding to 662.5 nm or fast ions with energies of 90 keV along

the sightline. The difference in energy between the prediction in [43] and the experimental results can be attributed to using a lower injection energy of 166 keV and a deviation of the installed sightline from the ideal geometry. Despite this, the high-energy view on LHD can still isolate signals from fast ions with over 10 keV higher energies than the low-energy view. Based on this method, FIDA emission can be measured for fast ions above 100 keV in neutral beam heated plasmas using higher injection energies.

Fast ions in LHD have been measured using FICXS and VNC with analysis informed by FIDASIM and a reduced model distribution function. Low-energy FIDA density, which measures fast ions around the critical energy (20-60 keV), are seen to increase with heating power, increase with temperature, and decrease with bulk plasma density as expected by a local approximation. However, the dependency on these parameters is weaker than the local model. Additionally, the temperature dependence is weaker with ECH heating. High-energy FIDA density, which measures fast ions near the injection energy (100 - 120 keV) are consistent except for a negative temperature dependence which disagrees with the local model. The regression model $A_0 P_{\mathrm{HNB}}^{a_1} T_e^{a_2} n_e^{a_3}$ is insufficient in providing a full description of measured data. Investigation into additional parameters, including the large 7-O LOS intersection with the diagnostic beamline, should be considered in future analysis of measured FIDA density. It should be noted that the parameter scan only includes measurements of co-passing fast ions produced by NB1 and NB3 that are traveling in the same direction as the toroidal field. This is due to the NB2-heated cases, which would have counter-passing fast ions, consistently surpassing the MHD-quiescent threshold. Inclusion of counter-passing fast ion orbits in a future study could provide additional insight if it can be achieved without strong MHD activity.

Measurements and FIDASIM simulations do not show a significant improvement in confinement of fast ions with an inward-shifted magnetic axis. Conversely, an increase in neutron counts with an inward-shifted axis suggests that improved confinement of trapped fast ions is

visible by VNC while FICXS only observes passing fast ions that are marginally affected by the shifted axis. Finite-pressure VMEC calculations of the $R_{ax} = 3.55$ m case matches previous results that used vacuum-field VMEC to identify the similarities between the $R_{ax} = 3.6$ m case and the σ-optimized configuration described by Mynick [47]. DELTA5D simulations indicate that fast ions in the regions of velocity-space that are visible to FICXS maintain passing orbits, confirming the failure to observe improvement in confinement. Simulations of low-pitch orbits show fast ions becoming deeply trapped with moderate radial drift in the inward-shifted configuration while fast ions in the outward-shifted configuration continue to be weakly trapped with much larger radial drift. Similar to the parameter scan, counter-passing fast ions are not included in the comparison of R_{ax} and valuable insight could be gained by inclusion in a future study.

It should be noted that radial electric field effects are not considered in the present study. Changing the magnetic configuration changes the radial electric field structure [70] which can affect fast ion confinement. Radial electric field effects on fast ions are discussed in a separate study using the gyrokinetic toroidal code GTC [71]. Additional experiments have recently been conducted using fast ion loss measurements as part of the GTC study and inclusion of radial electric field in shifted axis effects is left for future work.

Magnetohydrodynamic instabilities are observed in both high- and low-field discharges due to counter-B_t neutral beam injection. Alfvén continuum calculations show TAE gaps with radial extent due to poloidal mode coupling. These gaps appear for $n = 1$ and 2 toroidal mode numbers. Fast ion transport due to observed Alfvén eigenmodes (AE) is not observed in the high-field discharges. Deviation between fast ion measurements and simulations in the low-field discharge suggests fast ion transport due to AEs. However, reduced confinement of fast ions is also attributed to decreased neoclassical confinement at low field.

7.2 Future work

The prototype fast ion spectrometer prototype is designed for the JT-60SA tokamak. A final version of the instrument has been delivered and is scheduled to be installed. Once installed, the spectrometer will provide measurements of fast ions born from the 500 keV negative-ion neutral beam injection system [72]. The diagnostic will require verification and validation in order to provide reliable measurements of fast ions in the advanced tokamak.

An analytical model is used for the reduced model fast ion distribution input to FIDASIM but other codes may provide more robust physics while being relatively inexpensive. The physics required to sufficiently describe fast ions born from neutral beam injection in toroidal devices should include charge-exchange and recombination of neutrals, collisional slowing-down effects such as energy diffusion, pitch-angle scattering, and electron and ion friction, and neoclassical transport of fast ions to a steady state distribution. FIDASIM is capable of calculating the ionization of injected neutrals, this is part of the Goldston distribution workflow. However, collisional slowing down and neoclassical transport in full 5D phase space can be challenging. Recent work by *Kulla, et al.* validated fast ion distribution calculations using BEAMS3D [73] for the ASDEX-Upgrade tokamak. BEAMS3D is a collisional guiding center code in cylindrical coordinates that tracks fast ions born by neutral beam injection in non-axisymmetric geometries [74]. This should provide reasonable calculations of slowing-down effects and neoclassical transport to evolve the fast ion birth profile to a steady-state distribution. Another option is FIRM3D, a collisionless guiding center code for tracking fast ions in Boozer coordinates [75]. While slowing-down effects are not currently implemented in FIRM3D, the description of equations of motion in Boozer coordinates simplifies calculations for non-axisymmetric geometries. FIRM3D is also capable of particle tracking in the presence of an AE [76] which would allow for a birth profile to evolve to a perturbed distribution. Validation of BEAMS3D and FIRM3D using fast ion measurements in a stellarator would

allow for computationally inexpensive modeling of the fast ion distribution in steady-state plasmas and plasmas with AE activity.

The study in the present work on magnetohydrodynamic activity is limited to three cases which are a subset of a larger number of discharges. With an improved fast ion distribution model, comparisons of fast ion measurements and simulations should be carried out for a full database study. In addition to TAEs other MHD activity is observed but unclassified in the larger dataset. Changes in fast ion measurements due to helicity-induced modes (HAE) would provide valuable insight into the complex wave-particle interactions in 3D geometries. Energetic-particle-driven resistive interchange modes (EIC) are also observed in LHD. These modes can improve bulk plasma performance [77] but also incur fast ion losses [78]. Comparison of AE activity in LHD with other stellarators should also be considered. Fast ion losses due to AEs have been observed in TJ-II with radial structures measured using a heavy ion beam probe diagnostic [79]. These AEs appear more commonly with a flattened temperature profile while the AEs observed in LHD consistently appear with a peaked profile. LHD is also equipped with a heavy ion beam probe. While radial structure measurements were previously unavailable for the current dataset, heavy ion beam probe measurements were made during some of the experiments. Reproducing the method used on TJ-II to recover the AE structure is worth further investigation. AEs are also observed in W7-X with different driving mechanisms. While AEs in LHD are driven by beam ions, W7-X mode activity is observed even when beam ions are not present which suggests excitation due to turbulence [80]. W7-X is also a numerically-optimized stellarator that was designed to be a quasi-isodynamic device. Comparison of "traditional" AEs in LHD to the turbulence-driven AEs in W7-X will provide insight into (a) expanded driving mechanisms for AEs and (b) differences in AE behavior between numerically-optimized and drift-optimized stellarators. Here, drift-optimized refers to the reduced drift orbits in the inward-shifted LHD configuration.

Bibliography

[1] Mitsuru Kikuchi and Internationale Atomenergie-Organisation, editors. *Fusion physics*. Number 1562 in Publication / Division of Scientific and Technical Information, International Atomic Energy Agency. International Atomic Energy Agency, Vienna, 2012.

[2] H.-S. Bosch and G. M. Hale. Improved formulas for fusion cross-sections and thermal reactivities. *Nuclear Fusion*, 32(4):611, April 1992.

[3] Jeffrey P. Freidberg. *Ideal MHD*. Cambridge University Press, Cambridge, 2014.

[4] John Wesson. *Tokamaks*. Number 149 in International series of monographs on physics. Oxford Univ. Press, Oxford, 4. ed edition, 2011.

[5] Allen H. Boozer. Stellarators as a fast path to fusion. *Nuclear Fusion*, 61(9):096024, August 2021. Publisher: IOP Publishing.

[6] Masahiro Wakatani and Masahiro Wakatani. *Stellarator and heliotron devices*. Number 95 in International series of monographs on physics. Oxford University Press, New York, 1998.

[7] Lise-Marie Imbert-Gérard, Elizabeth J. Paul, and Adelle M. Wright. *An introduction to stellarators: from magnetic fields to symmetries and optimization*. Number 202 in Other titles in applied mathematics. Society for Industrial and Applied Mathematics, Philadelphia, 2024.

[8] Allen H. Boozer. Plasma equilibrium with rational magnetic surfaces. *The Physics of Fluids*, 24(11):1999–2003, November 1981.

[9] A Iiyoshi, A Komori, A Ejiri, M Emoto, H Funaba, M Goto, K Ida, H Idei, S Inagaki, S Kado, O Kaneko, K Kawahata, T Kobuchi, S Kubo, R Kumazawa, S Masuzaki, T Minami, J Miyazawa, T Morisaki, S Morita, S Murakami, S Muto, T Mutoh, Y Nagayama, Y Nakamura, H Nakanishi, K Narihara, K Nishimura, N Noda, S Ohdachi, N Ohyabu, Y Oka, M Osakabe, T Ozaki, B.J Peterson, A Sagara, S Sakakibara, R Sakamoto, H Sasao, M Sasao, K Sato, M Sato, T Seki, T Shimozuma, M Shoji, H Suzuki, Y Takeiri, K Tanaka, K Toi, T Tokuzawa, K Tsumori, K Tsuzuki, K.Y Watanabe, T Watari, H Yamada, I Yamada, S Yamaguchi, M Yokoyama, R Akiyama, H Chikaraishi, K Haba, S Hamaguchi, M Iima, S Imagawa, N Inoue, K Iwamoto, S Kitagawa, J Kodaira,

Y Kubota, R Maekawa, T Mito, T Nagasaka, A Nishimura, C Takahashi, K Takahata, Y Takita, H Tamura, T Tsuzuki, S Yamada, K Yamauchi, N Yanagi, H Yonezu, Y Hamada, K Matsuoka, K Murai, K Ohkubo, I Ohtake, M Okamoto, S Satoh, T Satow, S Sudo, S Tanahashi, K Yamazaki, M Fujiwara, and O Motojima. Overview of the Large Helical Device project. *Nuclear Fusion*, 39(9Y):1245–1256, September 1999.

[10] Y. Takeiri, O. Kaneko, K. Tsumori, M. Osakabe, K. Ikeda, K. Nagaoka, H. Nakano, E. Asano, T. Kondo, M. Sato, M. Shibuya, S. Komada, and LHD Experiment Group. High Performance of Neutral Beam Injectors for Extension of LHD Operational Regime. *Fusion Science and Technology*, 58(1):482–488, August 2010.

[11] T. Shimozuma, H. Takahashi, S. Kubo, Y. Yoshimura, H. Igami, Y. Takita, S. Kobayashi, S. Ito, Y. Mizuno, H. Idei, T. Notake, M. Sato, K. Ohkubo, T. Watari, T. Mutoh, R. Minami, T. Kariya, T. Imai, and LHD Experiment Group. ECRH-Related Technologies for High-Power and Steady-State Operation in LHD. *Fusion Science and Technology*, 58(1):530–538, August 2010.

[12] H. Kasahara, T. Seki, K. Saito, R. Kumazawa, S. Kubo, T. Shimozuma, Y. Yoshimura, H. Igami, T. Notake, Y. Nakamura, J. Miyazawa, K. Tanaka, T. Tokuzawa, F. Shimpo, G. Nomura, M. Yokota, C. Takahashi, A. Komori, O. Motojima, and T. Mutoh. Control of a steady-state operation using ICRF heating in the large helical device. *Fusion Engineering and Design*, 83(2-3):253–255, April 2008.

[13] S. P Hirshman and O Betancourt. Preconditioned descent algorithm for rapid calculations of magnetohydrodynamic equilibria. *Journal of Computational Physics*, 96(1):99–109, September 1991.

[14] I. Yamada, H. Funaba, R. Yasuhara, H. Hayashi, N. Kenmochi, T. Minami, M. Yoshikawa, K. Ohta, J. H. Lee, and S. H. Lee. Calibrations of the LHD Thomson scattering system. *Review of Scientific Instruments*, 87(11):11E531, November 2016.

[15] M. Yoshinuma, K. Ida, M. Yokoyama, M. Osakabe, and K. Nagaoka. Charge-Exchange Spectroscopy with Pitch-Controlled Double-Slit Fiber Bundle on LHD. *Fusion Science and Technology*, 58(1):375–382, August 2010.

[16] W. W. Heidbrink and G. J. Sadler. The behaviour of fast ions in tokamak experiments. *Nuclear Fusion*, 34(4):535, April 1994.

[17] E.J. Paul, A. Bhattacharjee, M. Landreman, D. Alex, J.L. Velasco, and R. Nies. Energetic particle loss mechanisms in reactor-scale equilibria close to quasisymmetry. *Nuclear Fusion*, 62(12):126054, November 2022. Publisher: IOP Publishing.

[18] Dmitry Moseev and Mirko Salewski. Bi-Maxwellian, slowing-down, and ring velocity distributions of fast ions in magnetized plasmas. *Physics of Plasmas*, 26(2):020901, February 2019.

[19] M. Isobe, M. Sasao, S. Iiduka, A. V. Krasilnikov, S. Murakami, T. Mutoh, M. Osakabe, S. Sudo, K. Kawahata, N. Ohyabu, O. Motojima, and LHD experiment group. Charge

exchange neutral particle analysis with natural diamond detectors on LHD heliotron. *Review of Scientific Instruments*, 72(1):611–614, January 2001.

[20] W. W. Heidbrink. Fast-ion Dα measurements of the fast-ion distribution. *Review of Scientific Instruments*, 81(10):10D727, October 2010.

[21] Masaki Osakabe, Sadayoshi Murakami, Mikirou Yoshinuma, Katsumi Ida, Allan Whiteford, Motoshi Goto, Daiji Kato, Takako Kato, Kenichi Nagaoka, Tokihiko Tokuzawa, Yasuhiko Takeiri, and Osamu Kaneko. Fast ion charge exchange spectroscopy measurement using a radially injected neutral beam on the large helical device. *Review of Scientific Instruments*, 79(10):10E519, October 2008.

[22] Mitsutaka Isobe, Kunihiro Ogawa, Takeo Nishitani, Hitoshi Miyake, Takashi Kobuchi, Neng Pu, Hoiroki Kawase, Eiji Takada, Tomoyo Tanaka, Siyuan Li, Sachiko Yoshihashi, Akira Uritani, Jungmin Jo, Sadayoshi Murakami, and Masaki Osakabe. Neutron Diagnostics in the Large Helical Device. *IEEE Transactions on Plasma Science*, 46(6):2050–2058, June 2018.

[23] H. Nuga, R. Seki, S. Kamio, K. Ogawa, M. Isobe, M. Osakabe, M. Yokoyama, and LHD Experiment Group. Analysis of beam slowing-down process in large helical device based on Fokker–Planck operator including beam–beam Coulomb collision effect. *Nuclear Fusion*, 59(1):016007, November 2018.

[24] Hideo Nuga, Ryosuke Seki, Kunihiro Ogawa, Shuji Kamio, Yutaka Fujiwara, Masaki Osakabe, Mitsutaka Isobe, Takeo Nishitani, Masayuki Yokoyama, and LHD Experiment Group. Analysis of Energetic Particle Confinement in LHD Using Neutron Measurement and Simulation Codes. *Plasma and Fusion Research*, 14:3402075–3402075, 2019.

[25] H. Nuga, R. Seki, K. Ogawa, S. Kamio, Y. Fujiwara, M. Osakabe, M. Isobe, T. Nishitani, M. Yokoyama, and LHD Experiment Group. Studies of the fast ion confinement in the Large Helical Device by using neutron measurement and integrated codes. *Journal of Plasma Physics*, 86(3):815860306, June 2020.

[26] J.D. Strachan, P.L. Colestock, S.L. Davis, D. Eames, P.C. Efthimion, H.P. Eubank, R.J. Goldston, L.R. Grisham, R.J. Hawryluk, J.C. Hosea, J. Hovey, D.L. Jassby, D.W. Johnson, A.A. Mirin, G. Schilling, R. Stooksberry, L.D. Stewart, and H.H. Towner. Fusion neutron production during deuterium neutral-beam injection into the PLT tokamak. *Nuclear Fusion*, 21(1):67–81, January 1981.

[27] W. W. Heidbrink. Basic physics of Alfvén instabilities driven by energetic particles in toroidally confined plasmas. *Physics of Plasmas*, 15(5):055501, February 2008.

[28] D. A. Spong, R. Sanchez, and A. Weller. Shear Alfvén continua in stellarators. *Physics of Plasmas*, 10(8):3217–3224, August 2003.

[29] S Yamamoto, K Toi, S Ohdachi, N Nakajima, S Sakakibara, C Nührenberg, K.Y Watanabe, S Murakami, M Osakabe, M Goto, K Kawahata, S Masuzaki, S Morita, K Narihara, Y Narushima, N Ohyabu, Y Takeiri, K Tanaka, T Tokuzawa, H Yamada, I Yamada,

K Yamazaki, and Lhd Experimental Group. Experimental studies of energetic-ion-driven MHD instabilities in Large Helical Device plasmas. *Nuclear Fusion*, 45(5):326–336, May 2005.

[30] S. Yamamoto, K. Toi, N. Nakajima, S. Ohdachi, S. Sakakibara, K. Y. Watanabe, M. Goto, K. Ikeda, O. Kaneko, K. Kawahata, S. Masuzaki, T. Morisaki, S. Morita, S. Murakami, K. Narihara, Y. Oka, M. Osakabe, Y. Takeiri, K. Tanaka, T. Tokuzawa, K. Tsumori, H. Yamada, I. Yamada, and K. Yamazaki. Observation of Helicity-Induced Alfvén Eigenmodes in Large-Helical-Device Plasmas Heated by Neutral-Beam Injection. *Physical Review Letters*, 91(24):245001, December 2003.

[31] W.H.J. Hayashi, W.W. Heidbrink, C.M. Muscatello, D.J. Lin, M. Osakabe, K. Ogawa, Y. Kawamoto, H. Yamaguchi, R. Seki, H. Nuga, M. Isobe, Y. Fujiwara, and S. Kamio. Charge-exchange measurements of high-energy fast ions in LHD using negative-ion neutral beam injection. *Journal of Instrumentation*, 19(12):P12006, December 2024. Publisher: IOP Publishing.

[32] Y. Luo, W. W. Heidbrink, and K. H. Burrell. Design of a D-alpha beam-ion profile diagnostic. *Review of Scientific Instruments*, 75(10):3468–3470, October 2004.

[33] D. J. Lin, C. M. Muscatello, and W. W. Heidbrink. Development of a narrow stopband filter for spectroscopic fast ion deuterium-alpha measurements. *Review of Scientific Instruments*, 92(3):033107, March 2021.

[34] B. Geiger, L. Stagner, W.W. Heidbrink, R. Dux, R. Fischer, Y. Fujiwara, A.V. Garcia, A. S. Jacobsen, A. Jansen van Vuuren, A. N. Karpushov, D. Liu, P. A. Schneider, I. Sfiligoi, P. Zs. Poloskei, and M. Weiland. Progress in modelling fast-ion D-alpha spectra and neutral particle analyzer fluxes using FIDASIM. *Plasma Physics and Controlled Fusion*, 62(10):105008, August 2020. Publisher: IOP Publishing.

[35] Y. Fujiwara, S. Kamio, H. Yamaguchi, A. V. Garcia, L. Stagner, H. Nuga, R. Seki, K. Ogawa, M. Isobe, M. Yokoyama, W. W. Heidbrink, M. Osakabe, and LHD Experiment Group. Fast-ion D alpha diagnostic with 3D-supporting FIDASIM in the Large Helical Device. *Nuclear Fusion*, 60(11):112014, September 2020.

[36] Joshua Breslau, Marina Gorelenkova, Francesca Poli, Jai Sachdev, Alexei Pankin, Gopan Perumpilly, Xingqiu Yuan, and Laszlo Glant. TRANSP, 2018. Language: en.

[37] O. Sauter and S.Yu. Medvedev. Tokamak coordinate conventions:. *Computer Physics Communications*, 184(2):293–302, February 2013.

[38] S. Murakami, H. Yamada, M. Sasao, M. Isobe, T. Ozaki, T. Saida, P. Goncharov, J.F. Lyon, M. Osakabe, T. Seki, Y. Takeiri, Y. Oka, K. Tumori, K. Ikeda, T. Mutoh, R. Kumazawa, K. Saito, Y. Torii, T. Watari, A. Wakasa, K.Y. Watanabe, H. Funaba, and M. Yokoyama. Effect of Neoclassical Transport Optimization on Energetic Ion Confinement in LHD. *Fusion Science and Technology*, 46(2):241–247, September 2004.

[39] S Murakami, U Gasparino, H Idei, S Kubo, H Maassberg, N Marushchenko, N Nakajima, M Romé, and M Okamoto. 5-D simulation study of suprathermal electron transport in non-axisymmetric plasmas. *Nuclear Fusion*, 40(3Y):693–700, March 2000.

[40] P Vincenzi, T Bolzonella, S Murakami, M Osakabe, R Seki, and M Yokoyama. Upgrades and application of FIT3D NBI–plasma interaction code in view of LHD deuterium campaigns. *Plasma Physics and Controlled Fusion*, 58(12):125008, December 2016.

[41] S Murakami, A Fukuyama, T Akutsu, N Nakajima, V Chan, M Choi, S.C Chiu, L Lao, V Kasilov, T Mutoh, R Kumazawa, T Seki, K Saito, T Watari, M Isobe, T Saida, M Osakabe, M Sasao, and Lhd Experimental Group. A global simulation study of ICRF heating in the LHD. *Nuclear Fusion*, 46(7):S425–S432, July 2006.

[42] R.J. Goldston. Charge-exchange spectra near the injection energy in tokamaks equipped with tangential neutral beams – experiment and theory. *Nuclear Fusion*, 15(4):651, August 1975.

[43] C. M. Muscatello, W. W. Heidbrink, R. L. Boivin, C. Chrystal, C. S. Collins, Y. Fujiwara, and H. Yamaguchi. Diagnosis of fast ions produced by negative-ion neutral-beam injection with fast-ion deuterium-alpha spectroscopy. *Review of Scientific Instruments*, 90(7):073504, July 2019.

[44] Y. Luo, W. W. Heidbrink, K. H. Burrell, E. Ruskov, and W. M. Solomon. Fast-ion Dα measurements and simulations in quiet plasmas. *Physics of Plasmas*, 14(11):112503, November 2007.

[45] A. Komori, N. Ohyabu, H. Yamada, O. Kaneko, K. Kawahata, N. Ashikawa, P. deVaries, M. Emoto, H. Funaba, M. Goto, K. Ida, H. Idei, K. Ikeda, S. Inagaki, N. Inoue, M. Isobe, S. Kado, K. Khlopenkov, T. Kobuchi, S. Kubo, R. Kumazawa, Y. Liang, S. Masuzaki, Y. Matsumoto, T. Minami, J. Miyazawa, T. Morisaki, S. Morita, S. Murakami, S. Muto, T. Mutoh, Y. Nagayama, Y. Nakamura, H. Nakanishi, K. Narihara, Y. Narushima, K. Nishimura, N. Noda, T. Notake, S. Ohdachi, Y. Oka, M. Okamoto, M. Osakabe, T. Ozaki, R. O. Pavlichenko, B. J. Peterson, A. Sagara, K. Saito, S. Sakakibara, R. Sakamoto, H. Sasao, M. Sasao, K. Sato, M. Sato, T. Seki, T. Shimozuma, M. Shoji, H. Suzuki, M. Takechi, Y. Takeiri, N. Tamura, K. Tanaka, K. Toi, T. Tokuzawa, Y. Torii, K. Tsumori, I. Yamada, S. Yamaguchi, S. Yamamoto, M. Yokoyama, Y. Yoshimura, K. Y. Watanabe, T. Watanabe, T. Watari, Y. Hamada, K. Itoh, K. Matsuoka, K. Ohkubo, T. Satow, S. Sudo, K. Yamazaki, O. Motojima, and M. Fujiwara. Improved plasma performance on Large Helical Device. *Physics of Plasmas*, 8(5):2002–2008, May 2001.

[46] Arimitsu Wakasa, Sadayoshi Murakami, Noriyoshir Nakajima, Shun-ichi Oikawa, and Masafumi Itagaki. Monte Carlo Simulations Study of Neoclassical Transport in lnward Shifted LHD Configurations. *Journal of Plasma and Fusion Research*, 4:408–412, 2001.

[47] H. E. Mynick, T. K. Chu, and A. H. Boozer. Class of Model Stellarator Fields with Enhanced Confinement. *Physical Review Letters*, 48(5):322–326, February 1982.

[48] S. Murakami, A. Wakasa, H. Maaßberg, C. D. Beidler, H. Yamada, K. Y. Watanabe, and LHD Experimental Group. Neoclassical transport optimization of LHD. *Nuclear Fusion*, 42(11):L19, September 2002.

[49] T. Watanabe, Y. Matsumoto, M. Hishiki, S. Oikawa, H. Hojo, M. Shoji, S. Masuzaki, R. Kumazawa, K. Saito, T. Seki, T. Mutoh, A. Komori, and LHD Experimental Group. Magnetic field structure and confinement of energetic particles in the LHD. *Nuclear Fusion*, 46(2):291, January 2006.

[50] K. Ogawa, M. Isobe, T. Nishitani, S. Murakami, R. Seki, H. Nuga, S. Kamio, Y. Fujiwara, H. Yamaguchi, Y. Saito, S. Maeta, M. Osakabe, and LHD Experiment Group. Energetic ion confinement studies using comprehensive neutron diagnostics in the Large Helical Device. *Nuclear Fusion*, 59(7):076017, June 2019.

[51] A. Bader, D.T. Anderson, M. Drevlak, B.J. Faber, C.C. Hegna, S. Henneberg, M. Landreman, J.C. Schmitt, Y. Suzuki, and A. Ware. Modeling of energetic particle transport in optimized stellarators. *Nuclear Fusion*, 61(11):116060, October 2021. Publisher: IOP Publishing.

[52] M. Landreman, S. Buller, and M. Drevlak. Optimization of quasi-symmetric stellarators with self-consistent bootstrap current and energetic particle confinement. *Physics of Plasmas*, 29(8):082501, August 2022.

[53] Kenji Tanaka, Clive Michael, Masayuki Yokoyama, Osamu Yamagishi, Kazuo Kawahata, Tokihiko Tokuzawa, Mamoru Shohji, Hiroshi Yamada, Jyunichi Miyazawa, Shigeru Morita, Katsumi Ida, Mikiro Yoshinuma, Kazumichi Narihara, Ichihiro Yamada, Shigeru Inagaki, LHD Experimental Group, Leonid Vyacheslavov, Andrei Sanin, Sadayoshi Murakami, and Arimitsu Wakasa. Effect of Magnetic Configuration on Particle Transport and Density Fluctuation in LHD. *Fusion Science and Technology*, 51(1):97–111, January 2007.

[54] S. Sakakibara, H. Yamada, and LHD Experiment Group. Magnetic Measurements in LHD. *Fusion Science and Technology*, 58(1):471–481, August 2010.

[55] C Suzuki, K Ida, Y Suzuki, M Yoshida, M Emoto, and M Yokoyama. Development and application of real-time magnetic coordinate mapping system in the Large Helical Device. *Plasma Physics and Controlled Fusion*, 55(1):014016, December 2012. Publisher: IOP Publishing.

[56] S. P. Hirshman and J. C. Whitson. Steepest descent moment method for three-dimensional magnetohydrodynamic equilibria. Technical Report ORNL/TM-8861, Oak Ridge National Lab., TN (USA), October 1983.

[57] Proxima Fusion GmbH, Munich, Germany, Jonathan Schilling, Enrico Guiraud, and Veronika Siska. VMEC++, February 2025.

[58] W Ott, E Speth, and A Stäbler. Slowing-down of fast ions in a plasma: Energy transfer, charge exchange losses and wall sputtering. *Max-Planck-Institut für Plasmaphysik*, 1977.

[59] L. C. Johnson. Validation of spatial profile measurements of neutron emission in TFTR plasmas (invited). *Review of Scientific Instruments*, 63(10):4517–4522, October 1992.

[60] W. W. Heidbrink, Cris W. Barnes, G. W. Hammett, Y. Kusama, S. D. Scott, M. C. Zarnstorff, L. C. Johnson, D. McCune, S. S. Medley, H. K. Park, A. L. Roquemore, J. D. Strachan, and G. Taylor. The diffusion of fast ions in Ohmic TFTR discharges. *Physics of Fluids B: Plasma Physics*, 3(11):3167–3170, November 1991.

[61] A. L. Roquemore, R. C. Chouinard, M. Diesso, R. Palladino, J. D. Strachan, and G. D. Tait. TFTR multichannel neutron collimator. *Review of Scientific Instruments*, 61(10):3163–3165, October 1990.

[62] R. Sanchez, S. P. Hirshman, A. S. Ware, L. A. Berry, and D. A. Spong. Ballooning stability optimization of low-aspect-ratio stellarators*. *Plasma Physics and Controlled Fusion*, 42(6):641, June 2000.

[63] D. A. Spong. Three-dimensional effects on energetic particle confinement and stability. *Physics of Plasmas*, 18(5):056109, May 2011.

[64] Matt Landreman, Bharat Medasani, Florian Wechsung, Andrew Giuliani, Rogerio Jorge, and Caoxiang Zhu. SIMSOPT: A flexible framework for stellarator optimization. *Journal of Open Source Software*, 6(65):3525, September 2021.

[65] K Toi, K Ogawa, M Isobe, M Osakabe, D A Spong, and Y Todo. Energetic-ion-driven global instabilities in stellarator/helical plasmas and comparison with tokamak plasmas. *Plasma Physics and Controlled Fusion*, 53(2):024008, January 2011.

[66] M. Osakabe, S. Yamamoto, K. Toi, Y. Takeiri, S. Sakakibara, K. Nagaoka, K. Tanaka, K. Narihara, and the LHD Experimental Group. Experimental observations of enhanced radial transport of energetic particles with Alfvén eigenmode on the LHD. *Nuclear Fusion*, 46(10):S911, September 2006.

[67] K. Ogawa, M. Isobe, S. Kamio, H. Nuga, R. Seki, S. Sangaroon, H. Yamaguchi, Y. Fujiwara, E. Takada, S. Murakami, J. Jo, Y. Takemura, H. Sakai, K. Tanaka, T. Tokuzawa, R. Yasuhara, and M. Osakabe. Studies of energetic particle transport induced by multiple Alfvén eigenmodes using neutron and escaping energetic particle diagnostics in Large Helical Device deuterium plasmas. *Nuclear Fusion*, 62(11):112001, November 2022.

[68] M. Osakabe, M. Isobe, S. Murakami, S. Kobayashi, K. Saito, R. Kumazawa, T. Mutoh, T. Ozaki, M. Nishiura, E. Veshchev, T. Seki, Y. Takeiri, O. Kaneko, K. Nagaoka, T. Tokuzawa, K. Ogawa, K. Toi, S. Yamamoto, M. Sasao, and T. Watanabe. Fast-Ion Confinement Studies on LHD. *Fusion Science and Technology*, 58(1):131–140, August 2010. Publisher: American Nuclear Society _eprint: https://doi.org/10.13182/FST10-A10800.

[69] D. A. Spong, E. D'Azevedo, and Y. Todo. Clustered frequency analysis of shear Alfvén modes in stellarators. *Physics of Plasmas*, 17(2):022106, February 2010.

[70] K Ida, M Yoshinuma, M Yokoyama, S Inagaki, N Tamura, B.J Peterson, T Morisaki, S Masuzaki, A Komori, Y Nagayama, K Tanaka, K Narihara, K.Y Watanabe, C.D Beidler, and Lhd Experimental Group. Control of the radial electric field shear by modification of the magnetic field configuration in LHD. *Nuclear Fusion*, 45(5):391–398, May 2005.

[71] E. Green, W.H.J. Hayashi, X. Wei, W.W. Heidbrink, Z. Lin, and H. Yamaguchi. Energetic particle transport under the effects of the radial electric field in LHD. *Planned*, 2026.

[72] M. Hanada, A. Kojima, Y. Tanaka, T. Inoue, K. Watanabe, M. Taniguchi, M. Kashiwagi, H. Tobari, N. Umeda, N. Akino, M. Kazawa, K. Oasa, M. Komata, K. Usui, K. Mogaki, S. Sasaki, K. Kikuchi, S. Nemoto, K. Oshima, Y. Endo, T. Simizu, N. Kubo, M. Kawai, and L.R. Grisham. Progress in development and design of the neutral beam injector for JT-60SA. *Fusion Engineering and Design*, 86(6-8):835–838, October 2011.

[73] D. Kulla, S. Lazerson, A. Kappatou, M. Weiland, R.C. Wolf, and the ASDEX Upgrade Team. Validation of BEAMS3D against fast-ion D-alpha measurements at ASDEX-Upgrade using FIDASIM. *Nuclear Fusion*, 65(8):086032, August 2025.

[74] Matthew McMillan and Samuel A Lazerson. BEAMS3D Neutral Beam Injection Model. *Plasma Physics and Controlled Fusion*, 56(9):095019, September 2014.

[75] FIRM3D Contributors. FIRM3D: Fast ion reduced models in 3d. `https://github.com/ColumbiaStellaratorTheory/firm3d`, 2024. Documentation: `https://firm3d.readthedocs.io`.

[76] Elizabeth J. Paul, Harry E. Mynick, and Amitava Bhattacharjee. Fast-ion transport in quasisymmetric equilibria in the presence of a resonant alfvénic perturbation. *Journal of Plasma Physics*, 89(5):905890515, 2023.

[77] X. D. Du, K. Toi, M. Osakabe, S. Ohdachi, T. Ido, K. Tanaka, M. Yokoyama, M. Yoshinuma, K. Ogawa, K. Y. Watanabe, M. Isobe, K. Nagaoka, T. Ozaki, S. Sakakibara, R. Seki, A. Shimizu, Y. Suzuki, H. Tsuchiya, and LHD Experiment Group. Resistive Interchange Modes Destabilized by Helically Trapped Energetic Ions in a Helical Plasma. *Phys. Rev. Lett.*, 114(15):155003, April 2015.

[78] K. Ogawa, M. Isobe, S. Sugiyama, H. Matsuura, D.A. Spong, H. Nuga, R. Seki, S. Kamio, Y. Fujiwara, H. Yamaguchi, M. Osakabe, and LHD Experiment group. Energetic particle transport and loss induced by helically-trapped energetic-ion-driven resistive interchange modes in the Large Helical Device. *Nuclear Fusion*, 60(11):112011, November 2020.

[79] R. Jiménez-Gómez, A. Könies, E. Ascasíbar, F. Castejón, T. Estrada, L. G. Eliseev, A. V. Melnikov, J.A. Jiménez, D. G. Pretty, D. Jiménez-Rey, M.A. Pedrosa, A. De Bustos, and S. Yamamoto. Alfvén eigenmodes measured in the TJ-II stellarator. *Nuclear Fusion*, 51(3):033001, March 2011.

[80] S. Vaz Mendes, K. Rahbarnia, C. Slaby, H. Thomsen, J. Schilling, M. Borchardt, R. Kleiber, A. Könies, J.-P. Bähner, A. Von Stechow, T. Sunn Pedersen, and T. Klinger. Broadband Alfvénic excitation correlated to turbulence level in the Wendelstein 7-X stellarator plasmas. *Nuclear Fusion*, 63(9):096008, September 2023.

[81] L. Stagner, B. Geiger, and W.W. Heidbrink. FIDASIM: A Neutral Beam and Fast-ion Diagnostic Modeling Suite.

[82] LHD experiment data repository. https://doi.org/10.57451/lhd.analyzed-data.

Appendix A

Adaptive grid cells

The implementation of adaptive grid cells described in section 3.2.1 is listed in this appendix. Adaptive grid cells are implemented in the `track` and `track_cylindrical` subroutines in the FORTRAN source code for FIDASIM [81].

```
subroutine track(rin, vin, tracks, ntrack, los_intersect)
    !+ Computes the path of a neutral through the [[libfida:beam_grid]]
    real(Float64), dimension(3), intent(in)          :: rin
        !+ Initial position of particle
    real(Float64), dimension(3), intent(in)          :: vin
        !+ Initial velocity of particle
    type(ParticleTrack), dimension(:), intent(inout) :: tracks
        !+ Array of [[ParticleTrack]] type
    integer(Int32), intent(out)                      :: ntrack
        !+ Number of cells that a particle crosses
    logical, intent(out), optional                   :: los_intersect
        !+ Indicator whether particle intersects a LOS in [[libfida:
   spec_chords]]

    integer :: cc, i, j, ii, mind, ncross, id, k, adaptive,
   max_cell_splits
    integer, dimension(3) :: ind
    logical :: in_plasma1, in_plasma2, in_plasma_tmp, los_inter
    real(Float64) :: dT, dt1, inv_50, dt2, n_cells, split_tol, inv_param,
   inv_tol, inv_N, inv_dl, param_sum, param1, param2
    real(Float64), dimension(3) :: dt_arr, dr
    real(Float64), dimension(3) :: vn, inv_vn, vp
    real(Float64), dimension(3) :: ri, ri_tmp, ri_cell
    type(LocalEMFields) :: fields
    type(LocalProfiles) :: plasma1, plasma2
    type(LOSInters) :: inter
    real(Float64), dimension(n_stark) :: lambda
    integer, dimension(3) :: sgn
```

```
    integer, dimension(3) :: gdims

    vn = vin ; ri = rin ; sgn = 0 ; ntrack = 0
    adaptive = 0; max_cell_splits = 1; split_tol = 0.0

    los_inter=.False.
    if(.not.present(los_intersect)) then
        los_inter = .True. !avoids computation if not needed
    endif

    if(dot_product(vin,vin).eq.0.0) then
        return
    endif

    gdims(1) = beam_grid%nx
    gdims(2) = beam_grid%ny
    gdims(3) = beam_grid%nz

    !! define actual cell
    call get_indices(ri,ind)
    ri_cell = [beam_grid%xc(ind(1)), &
               beam_grid%yc(ind(2)), &
               beam_grid%zc(ind(3))]

    do i=1,3
        if (vn(i).gt.0.0) sgn(i) = 1
        if (vn(i).lt.0.0) sgn(i) =-1
        if (vn(i).eq.0.0) vn(i)  = 1.0d-3
    enddo

    !! Check adaptive switch, adaptive > 0 activates splitting
    adaptive = inputs%adaptive
    max_cell_splits = inputs%max_cell_splits
    if(adaptive.gt.0) then
        split_tol = inputs%split_tol
        if(split_tol.eq.0.0) then
            adaptive = 0
        else
            inv_tol = 1.0/split_tol
        endif
    endif

    dr = beam_grid%dr*sgn
    inv_vn = 1/vn
    inv_50 = 1.0/50.0
    cc=1
    tracks%time = 0.d0
    tracks%flux = 0.d0
    ncross = 0
    call in_plasma(ri,in_plasma1)
    track_loop: do i=1,beam_grid%ntrack
        if(cc.gt.beam_grid%ntrack) exit track_loop
        dt_arr = abs(( (ri_cell + 0.5*dr) - ri)*inv_vn)
        mind = minloc(dt_arr,1)
        dT = dt_arr(mind)
        ri_tmp = ri + dT*vn

```

```
83          !! Check if velocity intersects LOS and produces wavelength in the
    right region
84          inter = spec_chords%inter(ind(1),ind(2),ind(3))
85          if((.not.los_inter).and.(inter%nchan.ne.0))then
86              call get_fields(fields, pos=ri_tmp)
87              chan_loop: do j=1,inter%nchan
88                  id = inter%los_elem(j)%id
89                  vp = ri_tmp - spec_chords%los(id)%lens
90                  call doppler_stark(vp, vn, fields, beam_lambda0, lambda)
91                  los_inter = any((lambda.ge.inputs%lambdamin).and.(lambda.
    le.inputs%lambdamax))
92                  if(los_inter) exit chan_loop
93              enddo chan_loop
94          endif
95
96          call in_plasma(ri_tmp,in_plasma2)
97          if(in_plasma1.neqv.in_plasma2) then
98              dt1 = 0.0
99              track_fine: do ii=1,50
100                 dt1 = dt1 + dT*inv_50
101                 ri_tmp = ri + vn*dt1
102                 call in_plasma(ri_tmp,in_plasma_tmp)
103                 if(in_plasma2.eqv.in_plasma_tmp) exit track_fine
104             enddo track_fine
105             tracks(cc)%pos = ri + 0.5*dt1*vn
106             tracks(cc+1)%pos = ri + 0.5*(dt1 + dT)*vn
107             tracks(cc)%time = dt1
108             tracks(cc+1)%time = dT - dt1
109             tracks(cc)%ind = ind
110             tracks(cc+1)%ind = ind
111             cc = cc + 2
112             ncross = ncross + 1
113         elseif(adaptive.eq.0) then
114             tracks(cc)%pos = ri + 0.5*dT*vn
115             tracks(cc)%time = dT
116             tracks(cc)%ind = ind
117             cc = cc + 1
118         elseif(adaptive.gt.0) then !! If splitting is activated, calculate
    n_cells based on gradient between entrance and exit points
119             dt2 = 0.0
120             call get_plasma(plasma1, ri)
121             call get_plasma(plasma2, ri_tmp)
122
123             !! Split cell according to gradient of parameter, parameter is
    selected according to value of adaptive
124             select case (adaptive)
125                 case(1)
126                     param1 = plasma1%dene
127                     param2 = plasma2%dene
128                 case(2)
129                     param1 = sum(plasma1%denn(1,:))/size(plasma1%denn(1,:)
    )
130                     param2 = sum(plasma2%denn(1,:))/size(plasma2%denn(1,:)
    )
131                 case(3)
132                     param1 = plasma1%denf
133                     param2 = plasma2%denf
134                 case(4)
```

```
                    param1 = sum(plasma1%deni(:))/size(plasma1%deni(:))
                    param2 = sum(plasma2%deni(:))/size(plasma2%deni(:))
                case(5)
                    param1 = plasma1%denimp
                    param2 = plasma2%denimp
                case(6)
                    param1 = plasma1%te
                    param2 = plasma2%te
                case(7)
                    param1 = plasma1%ti
                    param2 = plasma2%ti
                case default
                    param1 = plasma1%dene
                    param2 = plasma2%dene
            end select

            param_sum = param1 + param2
            if(param_sum.le.0.0) then
                inv_param = 1.0
            else
                inv_param = 2.0/param_sum
            endif
            inv_dl = 1/(dT*norm2(vn))
            n_cells = ceiling(abs(param1 - param2)*inv_param*inv_dl*
    inv_tol)
            if(n_cells.gt.max_cell_splits) then
                n_cells = max_cell_splits
            elseif(n_cells.lt.1.0) then
                n_cells = 1.0
            endif
            inv_N = 1.0/n_cells
            split_loop2: do k=1,int(n_cells) !! Split time step and
    position by n_cells
                dt2 = dt2 + dT*inv_N
                tracks(cc)%pos = ri + 0.5*dt2*vn
                tracks(cc)%time = dT*inv_N
                tracks(cc)%ind = ind
                cc = cc + 1
            enddo split_loop2
        else
            tracks(cc)%pos = ri + 0.5*dT*vn
            tracks(cc)%time = dT
            tracks(cc)%ind = ind
            cc = cc + 1
        endif
        in_plasma1 = in_plasma2

        ri = ri + dT*vn
        ind(mind) = ind(mind) + sgn(mind)
        ri_cell(mind) = ri_cell(mind) + dr(mind)

        if (ind(mind).gt.gdims(mind)) exit track_loop
        if (ind(mind).lt.1) exit track_loop
        if (ncross.ge.inputs%max_crossings) then
            cc = cc - 1 !dont include last segment
            exit track_loop
        endif
     enddo track_loop
```

```
191     ntrack = cc-1
192     if(present(los_intersect)) then
193         los_intersect = los_inter
194     endif
195 
196 end subroutine track
```

Listing A.1: Implementation of adaptive grid cells in the FIDASIM `track` subroutine. A similar implementation is used in the `track_cylindrical` subroutine.

Appendix B

COCOS coordinate system

The implementation of COCOS described in section 3.2.2 is listed in this appendix. COCOS identification and transformation is implemented in the python preprocessing subroutines for FIDASIM [81].

```
#!/bin/sh
"exec" "$FIDASIM_DIR/deps/python" "$0" "$@"
# -*- coding: utf-8 -*-

#+#FIDASIM Utilities
#+This file contains useful FIDASIM utilities
#+***
from __future__ import print_function
import os
from os.path import dirname
import subprocess
import platform
import numpy as np
import copy
import h5py
import efit
from scipy.io import netcdf
from scipy.interpolate import interp1d, RectBivariateSpline,
    NearestNDInterpolator
from scipy.spatial import Delaunay
import matplotlib.pyplot as plt

FIDASIM_default_COCOS = 5
class COCOS:
    '''
    #+COCOS
    #+COCOS class object
    #+***
```

```
    '''
    def __init__(self, index=FIDASIM_default_COCOS):
        self.cocos = index
        self.exp_Bp = 0 if index < 10 else 1
        self.sigma_Bp = 1 if index in [1,2,5,6,11,12,15,16] else -1
        self.sigma_RphZ = 1 if index%2 != 0 else -1
        self.sigma_rhothph = 1 if index in [1,2,7,8,11,12,17,18] else -1
        self.sign_q = self.sigma_rhothph
        self.sign_pprime = -1*self.sigma_Bp

...

def read_geqdsk(filename, grid, poloidal=False, ccw_phi=True, exp_Bp=0, **convert_COCOS_kw):
    """
    #+#read_geqdsk
    #+Reads an EFIT GEQDSK file
    #+***
    #+##Arguments
    #+    **filename**: GEQDSK file
    #+
    #+    **grid**: Interpolation grid
    #+
    #+##Keyword Arguments
    #+    **poloidal**: Return rho_p (sqrt(normalized poloidal flux)) instead of rho (sqrt(normalized toroidal flux))
    #+
    #+    **ccw_phi**: Argument for identify_COCOS. Toroidal direction from top view, True if counter-clockwise, False if clockwise
    #+
    #+    **exp_Bp**: Argument for identify_COCOS. 0 if poloidal flux divided by 2 pi, 1 if using effective poloidal flux
    #+
    #+    **convert_COCOS_kw**: Keyword arguments to pass to convert_COCOS via transform_COCOS_from_geqdsk
    #+
    #+##Return Value
    #+Electronmagnetic fields structure, rho, btipsign
    #+
    #+##Example Usage
    #+```python
    #+>>> fields, rho, btipsign = read_geqdsk("./g133223.00200",grid)
    #+```
    """
    dims = grid['r2d'].shape
    r_pts = grid['r2d'].flatten()/100
    z_pts = grid['z2d'].flatten()/100

    g = efit.readg(filename)
    cc = identify_COCOS_from_geqdsk(g, ccw_phi=ccw_phi, exp_Bp=exp_Bp)

    cc_factor = cc.sigma_RphZ*cc.sigma_Bp/((2*np.pi)**cc.exp_Bp)

    btipsign = np.sign(g["current"]*g["bcentr"])

    fpol = g["fpol"]
    psiaxis = g["ssimag"]
    psiwall = g["ssibry"]
```

```
    r = g["r"]
    z = g["z"]

    psi_arr = np.linspace(psiaxis, psiwall, len(fpol))
    fpol_itp = interp1d(psi_arr, fpol, 'cubic', fill_value=fpol[-1], bounds_error=False)
    psirz_itp = RectBivariateSpline(r, z, g["psirz"])

    if poloidal:
        rhogrid = np.array([psirz_itp(rr,zz) for (rr,zz) in zip(r_pts, z_pts)]).reshape(dims)
        rhogrid = np.sqrt((rhogrid - g["ssimag"])/(g["ssibry"] - g["ssimag"]))
    else:
        rhogrid=efit.rho_rz(g,r_pts,z_pts,norm=True).reshape(dims)

    br = cc_factor*np.array([psirz_itp(rr,zz,dy=1)/rr for (rr,zz) in zip(r_pts,z_pts)]).reshape(dims)
    bz = cc_factor*np.array([-psirz_itp(rr,zz,dx=1)/rr for (rr,zz) in zip(r_pts,z_pts)]).reshape(dims)
    bt = np.array([fpol_itp(psirz_itp(rr,zz))/rr for (rr,zz) in zip(r_pts, z_pts)]).reshape(dims)

    er = br*0
    ez = bz*0
    et = bt*0

    mask = np.ones(dims,dtype=np.int32)

    equil = {"time":0.0,"data_source":os.path.abspath(filename), "mask": mask,
             "br":br,"bt":bt,"bz":bz,"er":er,"et":et,"ez":ez}

    return equil, rhogrid, btipsign

def transform_COCOS_from_geqdsk(g, ccw_phi=True, exp_Bp=0, **convert_COCOS_kw):
    '''
    #+#transform_COCOS_from_geqdsk
    #+Identifies the COCOS index of a GEQDSK dictionary object and converts to fidasim COCOS
    #+Reference:
    #+    O. Sauter and S. Yu. Medvedev, Tokamak Coordinate Conventions: COCOS,
    #+    Computer Physics Communications 184, 293 (2013).
    #+***
    #+###Arguments
    #+    **g**: GEQDSK dictionary object
    #+
    #+###Keyword Arguments
    #+    **ccw_phi**: Toroidal direction from top view, True if counter-clockwise, False if clockwise
    #+
    #+    **exp_Bp**: 0 if poloidal flux divided by 2 pi, 1 if using effective poloidal flux
    #+
    #+    **conver_COCOS_kw**: Keyword arguments for convert_COCOS
    #+
```

```
    #+###Return Value
    #+geqdsk dict with converted COCOS
    #+
    #+###Example Usage
    #+```python
    #+>>> g = efit.readg(filename)
    #+>>> g = read_COCOS_from_geqdsk(g)
    #+```
    '''
    cc_out = COCOS() # cc_out = FIDASIM COCOS

    cc_in = identify_COCOS_from_geqdsk(g, ccw_phi=ccw_phi, exp_Bp=exp_Bp)

    if cc_in.cocos != cc_out.cocos:
        return convert_COCOS(g.copy(), cc_in, cc_out, **convert_COCOS_kw)
    else:
        return g.copy()

def identify_COCOS_from_geqdsk(g, ccw_phi=True, exp_Bp=0):
    '''
    #+#identify_COCOS_from_geqdsk
    #+Identifies the COCOS index of a GEQDSK dictionary object
    #+Reference:
    #+    O. Sauter and S. Yu. Medvedev, Tokamak Coordinate Conventions: COCOS,
    #+    Computer Physics Communications 184, 293 (2013).
    #+***
    #+###Arguments
    #+    **g**: GEQDSK dictionary object
    #+
    #+###Keyword Arguments
    #+    **ccw_phi**: Toroidal direction from top view, True if counter-clockwise, False if clockwise
    #+
    #+    **exp_Bp**: 0 if poloidal flux divided by 2 pi, 1 if using effective poloidal flux
    #+
    #+###Return Value
    #+COCOS object
    #+
    #+###Example Usage
    #+```python
    #+>>> g = efit.readg(filename)
    #+>>> g_cocos = identify_COCOS_from_geqdsk(g)
    #+```
    '''
    # Sauter, eq. 22
    sigma_Bp_in = -1 * np.sign(g['pprime'][0] * g['current'])
    sigma_RphZ_in = 1 if ccw_phi else -1
    sigma_rhothph_in = np.sign(g['qpsi'][0] * g['current'] * g['bcentr'])

    sigmas = [sigma_Bp_in, sigma_RphZ_in, sigma_rhothph_in]
    index = identify_COCOS_index(sigmas)

    return COCOS(index+(10*exp_Bp))

def identify_COCOS_index(sigmas):
    """
```

```
    #+#identify_COCOS_index
    #+Identifies the COCOS index from sigma_Bp, sigma_{R, phi, Z}, and
   sigma_{rho, theta, phi}
    #+Reference:
    #+    O. Sauter and S. Yu. Medvedev, Tokamak Coordinate Conventions:
   COCOS,
    #+    Computer Physics Communications 184, 293 (2013).
    #+***
    #+##Arguments
    #+    **sigmas**: List-like object with values for sigma_Bp, sigma_{R,
    phi, Z}, and sigma_{rho, theta, phi}
    #+
    #+##Return Value
    #+Index for COCOS object
    #+
    #+##Example Usage
    #+```python
    #+>>> index = identify_COCOS_index([-1, 1, -1])
    #+>>> cocos = COCOS(index)
    #+```

    """
    if sigmas == [1, 1, 1]:
        index = 1
    elif sigmas == [1, -1, 1]:
        index = 2
    elif sigmas == [-1, 1, -1]:
        index = 3
    elif sigmas == [-1, -1, -1]:
        index = 4
    elif sigmas == [1, 1, -1]:
        index = 5
    elif sigmas == [1, -1, -1]:
        index = 6
    elif sigmas == [-1, 1, 1]:
        index = 7
    elif sigmas == [-1, -1, 1]:
        index = 8
    else:
        index = FIDASIM_default_COCOS

    return index

def convert_COCOS(g, cc_in, cc_out, sigma_Ip=None, sigma_B0=None, l_d
   =[1,1], l_B=[1,1], exp_mu0=[0,0]):
    '''
    #+#convert_COCOS
    #+Converts a GEQDSK dictionary according to cc_in --> cc_out
    #+Reference:
    #+    O. Sauter and S. Yu. Medvedev, Tokamak Coordinate Conventions:
   COCOS,
    #+    Computer Physics Communications 184, 293 (2013).
    #+***
    #+##Arguments
    #+    **g**: GEQDSK dictionary object
    #+
    #+    **cc_in**: COCOS object, input
    #+
```

```
    #+    **cc_out**: COCOS object, output
    #+
    #+###Keyword Arguments
    #+    **sigma_Ip**: Tuple of current sign, (in, out)
    #+
    #+    **sigma_B0**: Tuple of toroidal field sign, (in, out)
    #+
    #+    **l_d**: Tuple of length scale, (in, out)
    #+
    #+    **l_B**: Tuple of field magnitude scale, (in, out)
    #+
    #+    **exp_mu0**: Tuple of exponents for mu0, (in, out)
    #+
    #+###Return Value
    #+GEQDSK dictionary object
    #+
    #+###Example Usage
    #+```python
    #+>>> g = efit.readg(filename)
    #+>>> cc_out = COCOS(3)
    #+>>> cc_in = COCOS(1)
    #+>>> converted_g = convert_COCOS(g, cc_in, cc_out)
    #+```
    '''
    # Sauter, Appendix C
    print(f'CONVERT_COCOS: cocos_in ({cc_in.cocos}) != cocos_out ({cc_out.
    cocos}), applying COCOS conversion.')
    mu0 = 4*np.pi*1e-7

    l_d_eff = l_d[1]/l_d[0]
    l_B_eff = l_B[1]/l_B[0]
    exp_mu0_eff = exp_mu0[1] - exp_mu0[0]

    exp_Bp_eff = cc_out.exp_Bp - cc_in.exp_Bp
    sigma_Bp_eff = cc_out.sigma_Bp * cc_in.sigma_Bp
    sigma_RphZ_eff = cc_out.sigma_RphZ * cc_in.sigma_RphZ
    sigma_rhothph_eff = cc_out.sigma_rhothph * cc_in.sigma_rhothph

    if sigma_Ip is None:
        sigma_Ip_eff = sigma_RphZ_eff
    else:
        sigma_Ip_eff = np.prod(sigma_Ip)

    if sigma_B0 is None:
        sigma_B0_eff = sigma_RphZ_eff
    else:
        sigma_B0_eff = np.prod(sigma_B0)

    for key, val in g.items():
        if key in ['r', 'rdim', 'rleft', 'rbbbs', 'rlim', 'rcentr', '
    rmaxis', 'z', 'zdim', 'zmid', 'zbbbz', 'zlim', 'zmaxis', 'nbdry', 'lim'
    ]:
            g[key] = np.array(val) * l_d_eff
        elif key == 'bcentr':
            g[key] = np.array(val) * l_B_eff * sigma_B0_eff
        elif key in ['simag', 'ssimag', 'sibry', 'ssibry', 'psi', 'psirz'
    ]:
```

```
288             g[key] = np.array(val) * sigma_Ip_eff * sigma_Bp_eff * ((2*np.
    pi)**exp_Bp_eff) * (l_d_eff**2) * (l_B_eff)
289         elif key == 'current':
290             g[key] = np.array(val) * sigma_Ip_eff * l_d_eff * l_B_eff / (
    mu0**exp_mu0_eff)
291         elif key == 'fpol':
292             g[key] = np.array(val) * sigma_B0_eff * l_d_eff * l_B_eff
293         elif key == 'pres':
294             # Sauter, end of Sec. 4
295             g[key] = np.array(val) * (l_d_eff**2) / (mu0**exp_mu0_eff)
296         elif key == 'ffprim':
297             g[key] = np.array(val) * sigma_Ip_eff * sigma_Bp_eff / ((2*np.
    pi)**exp_Bp_eff) * l_B_eff
298         elif key == 'pprime':
299             g[key] = np.array(val) * sigma_Ip_eff * sigma_Bp_eff / ((2*np.
    pi)**exp_Bp_eff) * l_B_eff / ((mu0**exp_mu0_eff) * (l_d_eff**2))
300         elif key == 'qpsi':
301             g[key] = np.array(val) * sigma_Ip_eff * sigma_B0_eff *
    sigma_rhothph_eff
302
303     return g
```

Listing B.1: Implementation of the COCOS coordinate system in FIDASIM preprocessing subroutines (`FIDASIM/lib/python/fidasim/utils.py`).

Appendix C

VMEC input support

The implementation of VMEC support described in section 3.2.3 is listed in this appendix. VMEC input and transformation is implemented in the python preprocessing subroutines for FIDASIM [81].

```
#!/bin/sh
"exe" "$FIDASIM_DIR/deps/python" "$0" "$@"
# -*- coding: utf-8 -*-

"""
fourier_transform_3D and Brzp_transform adapted from pyFIDASIM/vmec_read.py
    @author: micha
"""

import numpy as np

from scipy.interpolate import griddata

def fourier_transform_3D(wout, ntheta=16, nphi=20, thetamin=None, thetamax=None, phimin=None, phimax=None):
    """
    #+#fourier_transform_3D
    #+ Performs 3D Fourier transform on objects with key in `wout['keys']`
    #+***
    #+##Input Arguments
    #+    **wout**: VMEC dictionary
    #+
    #+##Keyword Arguments
    #+    **ntheta**: Number of theta points
    #+
    #+    **nphi**: Number of phi points
    #+
```

```
    #+    **thetamin**: Minimum theta value
    #+
    #+    **thetamax**: Maximum theta value
    #+
    #+    **phimin**: Minimum phi value
    #+
    #+    **phimax**: Maximum phi value
    #+
    #+###Output Arguments
    #+    **new_wout**: VMEC dictionary
    #+
    #+###Example Usage
    #+```python
    #+>>> wout = read_vmec(file_name)
    #+>>> new_wout = fourier_transform_3D(wout, ntheta=16, nphi=20, thetamin=0, thetamax=2*pi, phimin=0, phimax=2*pi)
    #+```
    """
    new_wout = wout.copy()
    if (thetamin is None and thetamax is None) or (thetamin < 0 and thetamax > 2*np.pi) or (thetamin > thetamax):
        thetamin = 0
        thetamax = 2*np.pi
    if thetamin is None or thetamin < 0:
        thetamin = 0
    if thetamax is None or thetamax > 2*np.pi:
        thetamax = 2*np.pi

    if (phimin is None and phimax is None) or (phimin < 0 and phimax < 2*np.pi) or (phimin > phimax):
        phimin = 0
        phimax = 2*np.pi
    if phimin is None or phimin < 0:
        phimin = 0
    if phimax is None or phimax > 2*np.pi:
        phimax = 2*np.pi

    theta = np.linspace(thetamin, thetamax, ntheta)
    phi = np.linspace(phimin, phimax, nphi)

    pol, tor = np.meshgrid(theta, phi)
    pol_xm = np.dot(new_wout['xm'].reshape(new_wout['md'], 1), pol.reshape(1, nphi * ntheta))
    tor_xn = np.dot(new_wout['xn'].reshape(new_wout['md'], 1), tor.reshape(1, nphi * ntheta))

    cos_mu_nv = np.cos(pol_xm - tor_xn)
    sin_mu_nv = np.sin(pol_xm - tor_xn)

    if new_wout['nyq_limit']:
        for key in new_wout['keys']:
            if key in new_wout['cos_nyq_keys'] or key in new_wout['sin_nyq_keys']:
                pol_nyq_xm = np.dot(new_wout['xm_nyq'].reshape(new_wout['md_nyq'], 1), pol.reshape(1, nphi * ntheta))
                tor_nyq_xn = np.dot(new_wout['xn_nyq'].reshape(new_wout['md_nyq'], 1), pol.reshape(1, nphi * ntheta))

```

```
                cos_nyq_mu_nv = np.cos(pol_nyq_xm - tor_nyq_xn)
                sin_nyq_mu_nv = np.sin(pol_nyq_xm - tor_nyq_xn)

    inverse_fourier_amps = {}
    for key in new_wout['keys']:
        if key in new_wout['cos_keys']:
            inverse_fourier_amps[key] = np.dot(new_wout['fourier_amps'][key], cos_mu_nv).reshape(new_wout['ns'], nphi, ntheta)
        elif key in new_wout['sin_keys']:
            inverse_fourier_amps[key] = np.dot(new_wout['fourier_amps'][key], sin_mu_nv).reshape(new_wout['ns'], nphi, ntheta)
        elif new_wout['nyq_limit'] and key in new_wout['cos_nyq_keys']:
            inverse_fourier_amps[key] = np.dot(new_wout['fourier_amps'][key], cos_nyq_mu_nv).reshape(new_wout['ns'], nphi, ntheta)
        elif new_wout['nyq_limit'] and key in new_wout['sin_nyq_keys']:
            inverse_fourier_amps[key] = np.dot(new_wout['fourier_amps'][key], sin_nyq_mu_nv).reshape(new_wout['ns'], nphi, ntheta)
        else:
            raise NameError(f'key = "{key}" is not available')

    new_wout.update({
        'inverse_fourier_amps':inverse_fourier_amps,
        'ntheta':ntheta, 'thetamin':thetamin, 'thetamax':thetamax,
        'nphi':nphi, 'phimin':phimin, 'phimax':phimax,
        'theta':theta, 'phi':phi
        })

    return new_wout

def Brzp_transform(wout, cc_in_out=None, nrgrid=41, nzgrid=25, convert_m=True):
    """
    #+#Brzp_transform
    #+ Converts B(s,v,u) to B(R,Z,tor)
    #+***
    #+##Input Arguments
    #+    **wout**: VMEC dictionary
    #+
    #+##Keyword Arguments
    #+    **cc_in_out**: Pair of COCOS indices for field coordinate conversion
    #+
    #+    **nrgrid**: Number of R points
    #+
    #+    **nzgrid**: Number of Z points
    #+
    #+    **convert_m**: If true, convert meters to cm
    #+##Output Arguments
    #+    **new_wout**: VMEC dictionary
    #+
    #+##Example Usage
    #+```python
    #+>>> wout = read_vmec(file_name)
    #+>>> new_wout = fourier_transform_3D(wout)
    #+>>> new_new_wout = Brzp_transform(new_wout, cc_in_out=(3,5), nrgrid=61, nzgrid=25, convert_m=True)
    #+```
    """
```

```
    new_wout = wout.copy()
    inverse_fourier_amps = new_wout['inverse_fourier_amps']

    Bs = inverse_fourier_amps['Bs']
    Bv = inverse_fourier_amps['Bv']
    Bu = inverse_fourier_amps['Bu']

    R = inverse_fourier_amps['R']
    dR_ds = inverse_fourier_amps['dR_ds']
    dR_dv = inverse_fourier_amps['dR_dv']
    dR_du = inverse_fourier_amps['dR_du']

    dZ_ds = inverse_fourier_amps['dZ_ds']
    dZ_dv = inverse_fourier_amps['dZ_dv']
    dZ_du = inverse_fourier_amps['dZ_du']

    B_norm = np.zeros_like(R)
    denom = dR_ds * dZ_du - dR_du * dZ_ds
    nz = np.where(denom != 0)
    B_norm[nz] = 1. / denom[nz]

    # Calculates Br, Bz, Btor in (s,v,u) domain
    Br_svu = (dZ_du * Bs - dZ_ds * Bu) * B_norm
    Bz_svu = (dR_ds * Bu - dR_du * Bs) * B_norm
    Bt_svu = ( ( ( Bs * (dR_du * dZ_dv - dR_dv * dZ_du) + Bu * (dR_dv *
dZ_ds - dR_ds * dZ_dv) ) * B_norm ) + Bv ) / R

    new_wout.update({
        'Br_svu':Br_svu,
        'Bz_svu':Bz_svu,
        'Bt_svu':Bt_svu
        })

    Z = inverse_fourier_amps['Z']
    ns = new_wout['ns']

    S = np.zeros([ns, new_wout['ntheta']])
    for i in range(new_wout['ntheta']):
        S[:, i] = new_wout['s_dom']

    idx = np.arange(0, ns-1)

    for key in ['Br', 'Bz', 'Bt']:
        new_wout[key] = np.zeros([nrgrid, nzgrid, new_wout['nphi']])
    rho_grid = np.zeros([nrgrid, nzgrid, new_wout['nphi']])

    rmin, rmax = R.min(), R.max()
    zmin, zmax = Z.min(), Z.max()
    rgrid, zgrid = np.mgrid[rmin:rmax:complex(nrgrid), zmin:zmax:complex(
nzgrid)]
    rarr, zarr = rgrid[:, 0], zgrid[0, :]
    for iphi in range(new_wout['nphi']):
        rzdata = np.array([R[:, iphi, :].flatten(), Z[:, iphi, :].flatten
()]).T
        rho_grid[:, :, iphi] = np.sqrt(griddata(rzdata, S.flatten(), (
rgrid, zgrid), fill_value=0))

        idx = np.arange(1, ns, 1)
```

```
        rzdata = np.array([R[idx, iphi, :].flatten(), Z[idx, iphi, :].flatten()]).T
        for bkey in ['Br', 'Bz', 'Bt']:
            new_wout[bkey][:, :, iphi] = griddata(rzdata, new_wout[bkey+'_svu'][idx, iphi, :].flatten(), (rgrid, zgrid), fill_value=0)

    if cc_in_out:
        if isinstance(cc_in_out, (tuple, list, np.ndarray)) and len(cc_in_out) == 2:
            new_wout = convert_COCOS_VMEC(new_wout, cc_in_out)
        else:
            raise ValueError(f'cc_in_out must be a list-like object of length 2\n{cc_in_out=}')

    new_wout.update({
        'rho_grid':rho_grid,
        'R':rarr * (100 if convert_m else 1),
        'Z':zarr * (100 if convert_m else 1),
        'nr':rarr.size, 'nz':zarr.size
        })

    return new_wout

def convert_COCOS_VMEC(wout, cc_in_out):
    """
    #+#convert_COCOS_VMEC
    #+ Converts wout COCOS cc_in_out[0] to COCOS cc_in_out[1]
    #+***
    #+###Input Arguments
    #+    **wout**: VMEC dictionary
    #+
    #+###Keyword Arguments
    #+    **cc_in_out**: Pair of COCOS indices for field coordinate conversion
    #+
    #+###Output Arguments
    #+    **new_wout**: VMEC dictionary
    #+
    #+###Example Usage
    #+```python
    #+>>> wout = read_vmec(file_name)
    #+>>> new_wout = fourier_transform_3D(wout)
    #+>>> new_new_wout = Brzp_transform(new_wout, cc_in_out=(3,5), nrgrid=61, nzgrid=25, convert_m=True)
    #+>>> cc_wout = convert_COCOS_VMEC(new_new_wout, cc_in_out=(3,5))
    #+```
    """
    new_wout = {key:val for key, val in wout.items() if key not in ['Br', 'Bz', 'Bt']}

    cc_in, cc_out = cc_in_out
    sigma_RphZ_out = -1 if cc_in % 2 == 0 else 1
    sigma_RphZ_in = -1 if cc_out % 2 == 0 else 1
    sigma_RphZ_eff = sigma_RphZ_out * sigma_RphZ_in

    new_wout['Br'] = wout['Br'] * sigma_RphZ_eff
    new_wout['Bz'] = wout['Bz'] * sigma_RphZ_eff
    new_wout['Bt'] = wout['Bt'] * sigma_RphZ_eff
```

```
233
234     return new_wout
235
236 def fields_from_wout(wout, time=0.0, er=None, ez=None, et=None):
237     """
238     #+#fields_from_wout
239     #+ Extracts field components from ‘wout‘ into FIDASIM-readable fields
    object
240     #+***
241     #+##Input Arguments
242     #+    **wout**: VMEC dictionary
243     #+
244     #+##Keyword Arguments
245     #+    **time**: Experiment time
246     #+
247     #+    **er**: E-field radial component
248     #+
249     #+    **ez**: E-field vertical component
250     #+
251     #+    **et**: E-field toroidal component
252     #+
253     #+##Output Arguments
254     #+    **fields**: FIDASIM fields dictionary
255     #+
256     #+##Example Usage
257     #+‘‘‘python
258     #+>>> wout = read_vmec(file_name)
259     #+>>> new_wout = fourier_transform_3D(wout)
260     #+>>> new_new_wout = Brzp_transform(new_wout, cc_in_out=(3,5), nrgrid
    =61, nzgrid=25, convert_m=True)
261     #+>>> fields = fields_from_wout(new_new_wout, time=0.0, er=None, ez=
    None, et=None)
262     #+‘‘‘
263     """
264     if 'data_source' not in wout:
265         data_source = ''
266     else:
267         data_source = wout['data_source']
268
269     br, bz, bt = wout['Br'], wout['Bz'], wout['Bt']
270     btot =  np.sqrt(br**2 + bz**2 + bt**2)
271     ones = np.where(btot != 0)
272     bmask = np.zeros(btot.shape, dtype=int)
273     bmask[ones] = 1
274
275     if er is None:
276         er = np.zeros(btot.shape)
277     if ez is None:
278         ez = np.zeros(btot.shape)
279     if et is None:
280         et = np.zeros(btot.shape)
281
282     return {'time':time, 'mask':bmask,
283             'data_source':data_source,
284             'br':br, 'bz':bz, 'bt':bt,
285             'er':er, 'ez':ez, 'et':et}
286
287 def grid_from_wout(wout):
```

```
    """
    #+#grid_from_wout
    #+ Extracts interpolation grid from ‘wout‘ into FIDASIM-readable igrid
    object
    #++++
    #+##Input Arguments
    #+    **wout**: VMEC dictionary
    #+
    #+##Output Arguments
    #+    **igrid**: FIDASIM igrid dictionary
    #+
    #+##Example Usage
    #+‘‘‘python
    #+>>> wout = read_vmec(file_name)
    #+>>> new_wout = fourier_transform_3D(wout)
    #+>>> new_new_wout = Brzp_transform(new_wout, cc_in_out=(3,5), nrgrid
   =61, nzgrid=25, convert_m=True)
    #+>>> igrid = grid_from_wout(new_new_wout)
    #+‘‘‘
    """
    r, z, phi = wout['R'], wout['Z'], wout['phi']
    nr, nz, nphi = wout['nr'], wout['nz'], wout['nphi']
    z2d, r2d = np.meshgrid(z, r)
    return {'r':r, 'z':z, 'phi':phi,
            'nr':nr, 'nz':nz, 'nphi':nphi,
            'r2d':r2d, 'z2d':z2d}
```

Listing C.1: Implementation of VMEC input support in FIDASIM preprocessing subroutines (`FIDASIM/lib/vmec/utils.py`)

Appendix D

Goldston distribution

The subroutines for calculating a Goldston distribution (section 3.4) from a given set of plasma parameters are listed in this appendix. Calculations of Coulomb logarithms and physical constants are also listed. The necessary inputs for calculating a 3D (2 velocity, 1 position) Goldston distribution are: energy grid, pitch grid, fast ion source distributed in pitch, electron density in cm^{-3}, electron temperature in keV, thermal ion densities, thermal ion mass numbers, thermal ion charge numbers, thermal ion temperature, fast ion birth energy, fast ion atomic mass number, fast ion charge number, number of Legendre coefficients, and fast ion loss rate due to charge exchange with thermal neutrals (optional).

```
r"""
Solutions to the Fokker-Planck equation described by
Goldston [1]_.

References
----------
.. [1] Goldston, R.L., Charge-exchange spectra near the injection energy
    in tokamaks equipped with tangential neutral beams - experiment and
    theory, Nuclear Fusion **15** (1975) 651
"""

import numpy as np
import os
import sys

from scipy.special import legendre
from scipy.integrate import simpson
```

```
18
19 from physics import conv_kinetic_energy_to_speed, calc_Coulomb_ie,
       calc_Coulomb_ii, J_PER_EV, HYDR_MASS_KG
20
21 def calc_gaussian(x, x0, e0):
22     r"""
23     Calculate a Gaussian function. The initial fast ion birth
24     distribution in pitch space is assumed to be a Gaussian.
25
26     Parameters
27     ----------
28     x : np.ndarray of shape (n_x,), dtype float64
29         Dependent variable grid.
30     x0 : float
31         Center value of Gaussian distribution.
32     e0 : float
33         Spread of Gaussian distribution.
34
35     Returns
36     -------
37     gauss : np.ndarray of shape (n_x,), dtype float64
38         1-D (n_x,) Gaussian distribution.
39     """
40     if e0 == 0:
41         ix0 = np.abs(x - x0).argmin()
42         gauss = np.zeros_like(x)
43         gauss[ix0] = x0
44         return gauss
45     arg = (x - x0)/e0
46     coeff = 1/(e0*np.sqrt(2*np.pi))
47     gauss = coeff * np.exp(-0.5 * arg**2)
48
49     # Renormalize Gaussian so that integral(gauss) within the boundaries
50     # of x still goes to unity.
51     return gauss / simpson(gauss, x=x)
52
53 def calc_s_ell_from_pitch( ell, pitch, source_v_p):
54     r"""
55     Calculate Legendre coefficients for an expansion of a source
56     function in pitch space.
57
58     Parameters
59     ----------
60     ell : int
61         Legendre index.
62     pitch : np.ndarray of shape (n_pitch,), dtype float64
63         Pitch grid.
64     source_v_p : np.ndarray of shape (n_pitch,), dtype float64
65         Source grid vs pitch.
66
67     Returns
68     -------
69     s_ell : float
70         Legendre coefficient.
71
72     Notes
73     -----
74     Suppose a function $f(x)$ is defined over the domain [-1, 1] by a
```

```
    series of Legendre polynomials :math`:P_\ell`:
    .. math::
        f(x) = \sum_\ell f_\ell P_\ell
    The solution to :math:`f_\ell` is then:
    .. math::
        f_\ell = (\ell + \frac{1}{2})\int_{-1}^1 f(x) P_\ell(x) dx
    """
    pitch = np.where(np.abs(pitch) > 1, 0, pitch)
    P_ell = legendre(ell)(pitch)
    return (ell+0.5) * simpson(source_v_p*P_ell, x=pitch)

def calc_Gamma(n_e, T_e, A_f, Z_f):
    r"""
    Calclate :math:`\Gamma`.

    Parameters
    ----------
    n_e : np.ndarray of shape (n_rho,), dtype float64
        Thermal electron density profile in inverse cubic centimeters
        (cm-3).
    T_e : np.ndarray of shape (n_rho,), dtype float64
        Thermal electron temperature profile in kiloelectronvolts (keV).
    A_f : int
        Fast ion atomic mass number.
    Z_f : int
        Fast ion nuclear charge number.

    Returns
    -------
    Gamma : np.ndarray of shape (n_rho,), dtype float64
        :math:`\Gamma` factor profile.
    """
    return 2.39e11 * (Z_f/A_f)**2 * calc_Coulomb_ie(n_e, T_e)

def calc_A_bar(n_i, A_i):
    r"""
    Calculate :math:`\overline{A}_i`.

    Parameters
    ----------
    n_i : np.ndarray of shape (n_species, n_rho), dtype float64
        Thermal ion densities in inverse cubic centimeters (cm-3).
    A_i : np.ndarray of shape (n_species,), dtype int32
        Thermal ion mass numbers.

    Returns
    -------
    A_bar : np.ndarray of shape (n_rho,), dtype float64
        Density-weighted average ion mass number profile.
    """
    if n_i.shape[0] != A_i.size:
        raise Exception(
            f'Shape mismatch between '
            f'ni_s ({n_i.shape}) and Ai_s ({A_i.shape})')

    n_i_sum = n_i.sum(0)
    A_bar = np.divide(
        np.dot(A_i, n_i).sum(), n_i_sum, out=np.zeros(n_i.shape[1]),
```

```
        where=n_i_sum != 0 )
    return A_bar

def calc_Z_box( n_e, T_e, n_i, A_i, Z_i, v_f, A_f, Z_f, A_bar=None:
    r"""
    Calculate collisional effective nuclear charge.

    Parameters
    ----------
    n_e : np.ndarray of shape (n_rho,), dtype float64
        Thermal electron density profile in inverse cubic centimeters
        (cm-3).
    T_e : np.ndarray of shape (n_rho,), dtype float64
        Thermal electron temperature profile in kiloelectronvolts (keV).
    n_i : np.ndarray of shape (n_species, n_rho), dtype float64
        Thermal ion densities in inverse cubic centimeters (cm-3).
    A_i : np.ndarray of shape (n_species,), dtype int32
        Thermal ion mass numbers.
    Z_i : np.ndarray of shape (n_species,), dtype int32
        Thermal ion charge numbers.
    v_f : float
        Fast ion speed in centimeters per second (cm/s).
    A_f : int
        Fast ion atomic mass number.
    Z_f : int
        Fast ion nuclear charge number.
    A_bar : np.ndarray of shape (n_rho,), dtype float64
        Density-weighted average ion mass number profile. If `None`,
        then `A_bar` is calculated using `calc_A_bar(n_i, A_i)`. Default
        is `None`.

    Returns
    -------
    Z_box : np.ndarray of shape (n_rho,), dtype float64
        Collisional effective nuclear charge profile.
    """
    if A_bar is None: A_bar = calc_A_bar(n_i, A_i) # (n_rho,)
    log_lambda_ie = calc_Coulomb_ie(n_e, T_e) # (n_rho,)
    log_lambda_ii = calc_Coulomb_ii(
        n_e, T_e, A_i, Z_i, v_f, A_f, Z_f) # (n_rho,)

    coeff = np.divide(
        A_bar, n_e*log_lambda_ie, out=np.zeros_like(A_bar),
        where=n_e*log_lambda_ie != 0 ) # (n_rho,)

    Z_i_2 = Z_i**2
    Z_i_2_over_A_i = np.divide(
        Z_i_2, A_i, out=np.zeros(Z_i.size, dtype=float),
        where=A_i != 0 ) # (n_species,)
    arg = np.dot(Z_i_2_over_A_i, n_i*log_lambda_ii) # (n_rho,)
    return coeff * arg

def calc_Z_avg(n_e, T_e, n_i, A_i, Z_i, v_f, A_f, Z_f):
    r"""
    Calculate collisional average nuclear charge.

    Parameters
    ----------
```

```
    n_e : np.ndarray of shape (n_rho,), dtype float64
        Thermal electron density profile in inverse cubic centimeters
        (cm-3).
    T_e : np.ndarray of shape (n_rho,), dtype float64
        Thermal electron temperature profile in kiloelectronvolts (keV).
    n_i : np.ndarray of shape (n_species, n_rho), dtype float64
        Thermal ion densities in inverse cubic centimeters (cm-3).
    A_i : np.ndarray of shape (n_species,), dtype int32
        Thermal ion mass numbers.
    Z_i : np.ndarray of shape (n_species,), dtype int32
        Thermal ion charge numbers.
    v_f : float
        Fast ion speed in centimeters per second (cm/s).
    A_f : int
        Fast ion atomic mass number.
    Z_f : int
        Fast ion nuclear charge number.

    Returns
    -------
    Z_avg : np.ndarray of shape (n_rho,), dtype float64
        Collisional average nuclear charge profile.
    """
    log_lambda_ie = calc_Coulomb_ie(n_e, T_e)
    log_lambda_ii = calc_Coulomb_ii(n_e, T_e, A_i, Z_i, v_f, A_f, Z_f)
    coeff = np.divide(
        1, log_lambda_ie*n_e, out=np.zeros_like(n_e),
        where=log_lambda_ie*n_e != 0)
    Z_i_2 = Z_i**2
    arg = np.dot(Z_i_2, n_i*log_lambda_ii)
    return coeff * arg

def calc_Z_eff(n_e, n_i, Z_i):
    r"""
    Calculate effective nuclear charge.

    Parameters
    ----------
    n_e : np.ndarray of shape (n_rho,), dtype float64
        Thermal electron density profile in inverse cubic centimeters
        (cm-3).
    n_i : np.ndarray of shape (n_species, n_rho), dtype float64
        Thermal ion densities in inverse cubic centimeters (cm-3).
    Z_i : np.ndarray of shape (n_species,), dtype int32
        Thermal ion charge numbers.

    Returns
    -------
    Z_eff : np.ndarray of shape (n_rho,), dtype float64
        Effective nuclear charge profile.
    """
    nZ_i_2 = np.dot(Z_i**2, n_i)
    Z_eff = np.divide(
        nZ_i_2, n_e, out=np.zeros_like(n_e), where=n_e != 0 )
    return Z_eff

def calc_alpha_ell(ell, n_e, T_e, v_f, A_f, Gamma, Z_eff, tau_cx=None):
    r"""
```

```
    Calculate $\alpha_\ell$.

    Parameters
    ----------
    ell : int
        Legendre index.
    n_e : np.ndarray of shape (n_rho,), dtype float64
        Thermal electron density profile in inverse cubic centimeters
        (cm-3).
    T_e : np.ndarray of shape (n_rho,), dtype float64
        Thermal electron temperature profile in kiloelectronvolts (keV).
    v_f : float
        Fast ion speed in centimeters per second (cm/s).
    A_f : int
        Fast ion atomic mass number.
    Z_f : int
        Fast ion nuclear charge number.
    Gamma : np.ndarray of shape (n_rho,), dtype float64
        :math:`\Gamma` factor profile.
    Z_eff : np.ndarray of shape (n_rho,), dtype float64
        Effective nuclear charge profile. Calculated using
        `calc_Z_eff(n_e, n_i, Z_i)` or
        `calc_Z_avg(n_e, T_e, n_i, A_i, Z_i, v_f, A_f, Z_f)`.
    tau_cx : np.ndarray of shape (n_rho,), dtype float64
        Charge-exchange loss rate of fast ions. Default is None.

    Returns
    -------
    alpha_ell : np.ndarray of shape (n_rho,), dtype float64
        Velocity-space decay/growth profile.
    """
    inv_tau_cx = 0 if ((tau_cx is None) or (tau_cx == 0)) else 1/tau_cx

    v_f_3 = v_f**3
    pitch_angle_scattering = ell*(ell+1)*Z_eff*Gamma * np.divide(
        n_e, 2*v_f_3, out=np.zeros_like(n_e), where=v_f_3 != 0 )

    T_e_eV = T_e * 1e3 # keV -> eV
    T_e_1_5 = T_e_eV**1.5
    velocity_compression = -1.99e-20*Gamma*A_f * np.divide(
        n_e, T_e_1_5, np.zeros_like(n_e), where=T_e_1_5 != 0 )

    return inv_tau_cx + pitch_angle_scattering + velocity_compression

def calc_beta(n_e, T_e, v_f, A_f, A_bar, Gamma, Z_box):
    r"""
    Calculate :math:`\beta`.

    Parameters
    ----------
    n_e : np.ndarray of shape (n_rho,), dtype float64
        Thermal electron density profile in inverse cubic centimeters
        (cm-3).
    T_e : np.ndarray of shape (n_rho,), dtype float64
        Thermal electron temperature profile in kiloelectronvolts (keV).
    v_f : float
        Fast ion speed in centimeters per second (cm/s).
    A_f : int
```

```
        Fast ion atomic mass number.
    A_bar : np.ndarray of shape (n_rho,), dtype float64
        Density-weighted average ion mass number profile. Calculated
        using `calc_A_bar(n_i, A_i)`.
    Gamma : np.ndarray of shape (n_rho,), dtype float64
        :math:`\Gamma` factor profile.
    Z_box : np.ndarray of shape (n_rho,), dtype float64
        Collisional effective nuclear charge profile.
        Calculated using `calc_Z_box(n_e, T_e, n_i, A_i, Z_i, v_f, A_f,
        Z_f, A_bar=A_bar)`.

    Returns
    -------
    beta : np.ndarray of shape (n_rho,), dtype float64
        Thermal friction profile.
    """
    coeff = n_e * A_f * Gamma

    T_e_eV = T_e * 1e3 # keV -> eV
    T_e_1_5 = T_e_eV**1.5
    electron_friction = 6.62e-21 * np.divide(
        v_f, T_e_1_5, out=np.zeros_like(T_e), where=T_e_1_5 != 0 )

    v_f_2 = v_f**2
    ion_friction = np.divide(
        Z_box, A_bar*v_f_2, out=np.zeros_like(Z_box), where=A_bar*v_f_2 !=
    0 )

    return coeff * (electron_friction + ion_friction)

def calc_gamma(n_e, T_e, T_i, v_f, Gamma, Z_box):
    r"""
    Calculate :math:`\gamma`.

    Parameters
    ----------
    n_e : np.ndarray of shape (n_rho,), dtype float64
        Thermal electron density profile in inverse cubic centimeters
        (cm-3).
    T_e : np.ndarray of shape (n_rho,), dtype float64
        Thermal electron temperature profile in kiloelectronvolts (keV).
    T_i : np.ndarray of shape (n_rho,), dtype float64
        Thermal ion temperature profile in kiloelectronvolts (keV).
    v_f : float
        Fast ion speed in centimeters per second (cm/s).
    A_f : int
        Fast ion atomic mass number.
    A_bar : np.ndarray of shape (n_rho,), dtype float64
        Density-weighted average ion mass number profile. Calculated
        using `calc_A_bar(n_i, A_i)`.
    Gamma : np.ndarray of shape (n_rho,), dtype float64
        :math:`\Gamma` factor profile.
    Z_box : np.ndarray of shape (n_rho,), dtype float64
        Collisional effective nuclear charge profile.
        Calculated using `calc_Z_box(n_e, T_e, n_i, A_i, Z_i, v_f, A_f,
        Z_f, A_bar=A_bar)`.

    Returns
```

```
    -------
    gamma : np.ndarray of shape (n_rho,), dtype float64
        Thermal diffusion profile.
    """
    coeff = n_e * Gamma

    T_e_eV = T_e * 1e3 # keV -> eV
    sqrt_T_e = np.sqrt(T_e_eV, out=np.zeros_like(T_e), where=T_e_eV >= 0)
    electron_diffusion = np.divide(
        6.34e-9, sqrt_T_e, out=np.zeros_like(T_e), where=sqrt_T_e != 0)

    v_f_3 = v_f**3
    T_i_eV = T_i * 1e3 # keV -> eV
    ion_diffusion = 9.58e11 * T_i_eV * np.divide(
        Z_box, A_bar*v_f_3, out=np.zeros_like(Z_box), where=A_bar*v_f_3 !=
    0 )

    return coeff * (electron_diffusion + ion_diffusion)

def calc_steady_state_a_ell(velocity, v_f, beta, gamma, s_ell):
    r"""
    Calculate :math:`a_\ell` term for Goldston's steady-state solution
    to the Fokker-Planck equation.

    Parameters
    ----------
    velocity : np.ndarray of shape (n_velocity,), dtype float64
        Velocity grid in centimeters per second (cm/s).
    v_f : float
        Fast ion speed in centimeters per second (cm/s).
    alpha_ell : np.ndarray of shape (n_rho,), dtype float64
        Velocity-space decay/growth profile.
    beta : np.ndarray of shape (n_rho,), dtype float64
        Thermal friction profile.
    gamma : np.ndarray of shape (n_rho,), dtype float64
        Thermal diffusion profile.
    s_ell : float
        Legendre coefficient.

    Returns
    -------
    a_ell : np.ndarray of shape (n_velocity, n_rho), dtype float64
        Legendre coefficient for the steady-state solution in velocity
        space of the Fokker-Planck equation.
    """
    beta_2 = beta**2
    Delta_ell_arg = 1 + 4*alpha_ell*np.divide(
        gamma, beta_2, out=np.zeros_like(gamma), where=beta_2 != 0 ) # (
   n_rho,)
    Delta_ell = np.sqrt(
        Delta_ell_arg, out=np.zeros_like(Delta_ell_arg),
        where=Delta_ell_arg >= 0 ) # (n_rho,)
    n_rho = alpha_ell.size
    Delta_v = np.repeat((velocity - v_f)[:, np.newaxis], n_rho, axis=1) #
   (n_velocity, n_rho) cm/s

    n_velocity = velocity.size
    v_f_2 = v_f**2
```

```
    coeff_arg = 4 * np.pi * v_f_2 * beta * Delta_ell # (n_rho,)
    coeff = np.divide(
        1, coeff_arg, out=np.zeros_like(coeff_arg), where=coeff_arg != 0 )
    # (n_rho,)
    coeff_grid = np.repeat(coeff[np.newaxis, :], n_velocity, axis=0) # (
    n_velocity, n_rho)

    Delta_ell_grid = np.repeat(Delta_ell[np.newaxis, :], n_velocity, axis
    =0) # (n_velocity, n_rho)
    beta_grid = np.repeat(beta[np.newaxis, :], n_velocity, axis=0) # (
    n_velocity, n_rho)
    gamma_grid = np.repeat(gamma[np.newaxis, :], n_velocity, axis=0) # (
    n_velocity, n_rho)
    arg = -(1 + np.sign(Delta_v)*Delta_ell_grid) * beta_grid * np.divide(
        Delta_v, 2*gamma_grid, out=np.zeros_like(Delta_v),
        where=gamma_grid != 0 ) # (n_velocity, n_rho)

    return s_ell * coeff_grid * np.exp(arg)

def calc_steady_state(pitch, a_ell_grid):
    r"""
    Calculate Goldston's steady-state fast-ion distribution due to the
    Fokker-Planck equation.

    Parameters
    ----------
    pitch : np.ndarray of shape (n_pitch,), dtype float64
        Pitch grid.
    a_ell_grid : np.ndarray of shape (n_ell, n_velocity, n_rho), dtype
    float64
        Grid of Legendre coefficients for the steady-state solution in
        velocity space of the Fokker-Planck equation.

    Returns
    -------
    f_fastion : np.ndarray of shape (n_velocity, n_pitch, n_rho), dtype
    float64
        Fast-ion distribution.
    """
    n_ell = a_ell_grid.shape[0]

    leg_grid = np.array([
        legendre(ell)(pitch) for ell in range(n_ell) ]) # (n_ell, n_pitch)

    f_fastion = np.dot(leg_grid.T, a_ell_grid.swapaxes(0, 1)).swapaxes(0,
    1)
    return f_fastion

def calc_f_fastion_vP(velocity, pitch, source_v_p, n_e, T_e, n_i, A_i, Z_i
    , T_i, v_f, A_f, Z_f, n_ell=61, tau_cx:=None):
    r"""
    Calculate Goldston's steady-state fast-ion distribution due to the
    Fokker-Planck equation in velocity-pitch space.

    Parameters
    ----------
    velocity : np.ndarray of shape (n_velocity,), dtype float64
        Velocity grid in centimeters per second (cm/s).
```

```
    pitch : np.ndarray of shape (n_pitch,), dtype float64
        Pitch grid.
    source_v_p : np.ndarray of shape (n_pitch,), dtype float64
        Source grid vs pitch.
    n_e : np.ndarray of shape (n_rho,), dtype float64
        Thermal electron density profile in inverse cubic centimeters
        (cm-3).
    T_e : np.ndarray of shape (n_rho,), dtype float64
        Thermal electron temperature profile in kiloelectronvolts (keV).
    n_i : np.ndarray of shape (n_species, n_rho), dtype float64
        Thermal ion densities in inverse cubic centimeters (cm-3).
    A_i : np.ndarray of shape (n_species,), dtype int32
        Thermal ion mass numbers.
    Z_i : np.ndarray of shape (n_species,), dtype int32
        Thermal ion charge numbers.
    T_i : np.ndarray of shape (n_rho,), dtype float64
        Thermal ion temperature profile in kiloelectronvolts (keV).
    v_f : float
        Fast ion speed in centimeters per second (cm/s).
    A_f : int
        Fast ion atomic mass number.
    Z_f : int
        Fast ion nuclear charge number.
    n_ell : int, optional
        Number of Legendre coefficients. Default is 61.
    tau_cx : np.ndarray of shape (n_rho,), dtype float64
        Charge-exchange loss rate of fast ions. Default is None.

    Returns
    -------
    f_fastion_vP : np.ndarray of shape (n_velocity, n_pitch, n_rho), dtype
    float64
        Fast ion distribution as a function of velocity, pitch, and rho.
    """
    n_velocity = velocity.size
    n_rho = n_e.size

    Gamma = calc_Gamma(n_e, T_e, A_f, Z_f)
    Z_eff = calc_Z_avg(n_e, T_e, n_i, A_i, Z_i, v_f, A_f, Z_f)
    A_bar = calc_A_bar(n_i, A_i)
    Z_box = calc_Z_box(n_e, T_e, n_i, A_i, Z_i, v_f, A_f, Z_f, A_bar=A_bar
)
    beta = calc_beta(n_e, T_e, v_f, A_f, A_bar, Gamma, Z_box)
    gamma = calc_gamma(n_e, T_e, T_i, v_f, A_bar, Gamma, Z_box)

    a_ell_grid = np.zeros((n_ell, n_velocity, n_rho))
    for ell in range(n_ell):
        s_ell = calc_s_ell_from_pitch(ell, pitch, source_v_p)
        alpha_ell = calc_alpha_ell(
            ell, n_e, T_e, v_f, A_f, Gamma, Z_eff, tau_cx=tau_cx)
        a_ell_grid[ell] = calc_steady_state_a_ell(
            velocity, v_f, alpha_ell, beta, gamma, s_ell)

    f_fastion_vP = calc_steady_state(pitch, a_ell_grid)
    f_fastion_vP[np.isnan(f_fastion_vP)] = 0.0
    return f_fastion_vP

```

```python
def calc_f_fastion_EP(energy, pitch, source_v_p, n_e, T_e, n_i, A_i, Z_i, T_i, E_f, A_f, Z_f, n_ell=61, tau_cx=None):
    r"""
    Calculate Goldston's steady-state fast-ion distribution due to the Fokker-Planck equation in velocity-pitch space.

    Parameters
    ----------
    energy : np.ndarray of shape (n_energy,), dtype float64
        Energy grid in kiloelectronvolts (keV).
    pitch : np.ndarray of shape (n_pitch,), dtype float64
        Pitch grid.
    source_v_p : np.ndarray of shape (n_pitch,), dtype float64
        Source grid vs pitch.
    n_e : np.ndarray of shape (n_rho,), dtype float64
        Thermal electron density profile in inverse cubic centimeters (cm-3).
    T_e : np.ndarray of shape (n_rho,), dtype float64
        Thermal electron temperature profile in kiloelectronvolts (keV).
    n_i : np.ndarray of shape (n_species, n_rho), dtype float64
        Thermal ion densities in inverse cubic centimeters (cm-3).
    A_i : np.ndarray of shape (n_species,), dtype int32
        Thermal ion mass numbers.
    Z_i : np.ndarray of shape (n_species,), dtype int32
        Thermal ion charge numbers.
    T_i : np.ndarray of shape (n_rho,), dtype float64
        Thermal ion temperature profile in kiloelectronvolts (keV).
    E_f : float
        Fast ion energy in kiloelectronvolts (keV).
    A_f : int
        Fast ion atomic mass number.
    Z_f : int
        Fast ion nuclear charge number.
    n_ell : int, optional
        Number of Legendre coefficients. Default is 61.
    tau_cx : np.ndarray of shape (n_rho,), dtype float64
        Charge-exchange loss rate of fast ions. Default is None.

    Returns
    -------
    f_fastion_vP : np.ndarray of shape (n_velocity, n_pitch, n_rho), dtype float64
        Fast ion distribution as a function of velocity, pitch, and rho.
    """
    velocity = conv_kinetic_energy_to_speed(
        energy*1e3*J_PER_EV, A_f*HYDR_MASS_KG) * 100 # m/s -> cm/s
    v_f = conv_kinetic_energy_to_speed(
        E_f*1e3*J_PER_EV, A_f*HYDR_MASS_KG ) * 100 # m/s -> cm/s

    f_fastion_vP = calc_f_fastion_vP(
        velocity, pitch, source_v_p, n_e, T_e, n_i, A_i, Z_i, T_i, v_f,
        A_f, Z_f, n_ell=n_ell, tau_cx=tau_cx)
    f_fastion_EP = velocity[:, np.newaxis, np.newaxis] * f_fastion_vP
    return f_fastion_EP
```

Listing D.1: Implementation of the 3D Goldston distribution in python.

```python
import numpy as np
```

```
2
3  ZEFF_0 = 3.0
4
5  D_ALPHA = 656.104 # nm
6  H_ALPHA = 656.279 # nm
7
8  HBAR_SI = 1.054571817e-34 # J s
9  SPEED_OF_LIGHT = 299792458 # m/s
10 MU_NAUGHT_SI = 4*np.pi*1e-7 # N A-2
11 EPS_NAUGHT_SI = 1/(MU_NAUGHT_SI*SPEED_OF_LIGHT**2) # C^2 J-1 m-1
12
13 ELEMENTARY_CHARGE = 1.602176634e-19 # C
14 J_PER_EV = ELEMENTARY_CHARGE # J/eV
15
16 HYDR_MASS_KG  = 1.6726219260e-27
17
18 def conv_kinetic_energy_to_speed(energy, mass):
19     r"""
20     Convert kinetic energy to speed. Uses SI units.
21
22     Parameters
23     ----------
24     energy : float or np.ndarray of shape (n_energy,), dtype float64
25         Energy in Joules (J).
26     mass : float
27         Mass in kilograms (kg).
28
29     Returns
30     -------
31     speed : float or np.ndarray of shape (n_energy,), dtype float64
32         Speed calculated from particle kinetic energy.
33     """
34     if mass == 0: return 0
35     if np.isscalar(energy):
36         if energy/mass < 0: return 0
37         speed = np.sqrt(2*energy/mass)
38     else:
39         speed = np.sqrt(
40             2*energy/mass, out=np.zeros_like(energy), where=energy >= 0)
41     return speed
42
43 def _calc_Coulomb_ii(n_e, T_e, A_i, Z_i, v_f, A_f, Z_f):
44     r"""
45     Calculate the fast ion-thermal ion Coulomb logarithm for one thermal
46     ion species.
47
48     Parameters
49     ----------
50     n_e : np.ndarray of shape (n_rho,), dtype float64
51         Thermal electron density profile in inverse cubic centimeters
52         (cm-3).
53     T_e : np.ndarray of shape (n_rho,), dtype float64
54         Thermal electron temperature profile in kiloelectronvolts (keV).
55     A_i : int
56         Atomic mass number for a thermal ion species.
57     Z_i : int
58         Nuclear charge number for a thermal ion species.
59     v_f : float
```

```
        Fast ion speed in centimeters per second (cm/s).
    A_f : int
        Fast ion atomic mass number.
    Z_f : int
        Fast ion nuclear charge number.

    Returns
    -------
    log_lambda_ii : np.ndarray of shape (n_rho,), dtype float64
        Ion-ion Coulomb logarithm for fast ion collisions with a thermal
        ion species.
    """
    bmin, bmax = impact_parameter(n_e, T_e, A_i, Z_i, v_f, A_f, Z_f)
    if bmin == 0: return 0
    return np.log(
        bmax / bmin, out=np.zeros_like(bmax), where=(bmax / bmin) > 0)

def calc_Coulomb_ii(n_e, T_e, A_i, Z_i, v_f, A_f, Z_f):
    r"""
    Calculate the fast ion-thermal ion Coulomb logarithm for all thermal
    ion species.

    Parameters
    ----------
    n_e : np.ndarray of shape (n_rho,), dtype float64
        Thermal electron density profile in inverse cubic centimeters
        (cm-3).
    T_e : np.ndarray of shape (n_rho,), dtype float64
        Thermal electron temperature profile in kiloelectronvolts (keV).
    A_i : np.ndarray of shape (n_species,), dtype int32
        Atomic mass numbers for all thermal ion species.
    Z_i : np.ndarray of shape (n_species,), dtype int32
        Nuclear charge number for all thermal ion species.
    v_f : float
        Fast ion speed in centimeters per second (cm/s).
    A_f : int
        Fast ion atomic mass number.
    Z_f : int
        Fast ion nuclear charge number.

    Returns
    -------
    log_lambda_ii : np.ndarray of shape (n_rho,), dtype float64
        Ion-ion Coulomb logarithm for fast ion collisions with all
        thermal ion species.
    """
    return np.array([
        _calc_Coulomb_ii(n_e, T_e, A, Z, v_f, A_f, Z_f)
        for A, Z in zip(A_i, Z_i)])

def calc_Coulomb_ie(n_e, T_e):
    r"""
    Calculate the ion-electron Coulomb logarithm.

    Parameters
    ----------
    n_e : np.ndarray of shape (n_rho,), dtype float64
        Thermal electron density profile in inverse cubic centimeters
```

```
        (cm-3).
    T_e : np.ndarray of shape (n_rho,), dtype float64
        Thermal electron temperature profile in kiloelectronvolts (keV).

    Returns
    -------
    log_lambda_ie : np.ndarray of shape (n_rho,), dtype float64
        Ion-electron Coulomb logarithm.
    """
    n_e = np.array(n_e)
    n_rho = n_e.size
    sqrt_n_e = np.sqrt(n_e, out=np.full(n_rho, np.nan), where=n_e >= 0)

    T_e_eV = np.array(T_e) * 1e3 # keV -> eV
    above10 = T_e_eV > 10
    below10 = T_e_eV < 10
    cbrt_T_e = np.cbrt(
        T_e_eV, out=np.full(n_rho, np.nan), where=T_e_eV >= 0 )

    log_lambda_ie = np.zeros(n_rho)
    if above10.sum():
        above10_frac = np.divide(
            sqrt_n_e[above10],
            T_e_eV[above10],
            out=np.full(above10.sum(), np.nan),
            where=T_e_eV[above10] != 0 )
        log_lambda_ie[above10] = 24 - np.log(
            above10_frac,
            out=np.full(above10.sum(), np.nan),
            where=above10_frac > 0)
    if below10.sum():
        below10_frac = np.divide(
            sqrt_n_e[below10],
            cbrt_T_e[below10],
            out=np.full(below10.sum(), np.nan),
            where=cbrt_T_e[below10] != 0 )
        log_lambda_ie[below10] = 23 - np.log(
            below10_frac,
            out=np.full(below10.sum(), np.nan),
            where=below10_frac > 0)
    return log_lambda_ie
```

Listing D.2: Physical constants and subroutines for calculating Coulomb logarithms used in the Goldston distribution calculations.

Appendix E

Data for MHD-quiescent study

The data used in ch. 5 is listed in this appendix. Experiment conditions are single-source NBI heating with NB1 or NB3, counter-clockwise B_t at high field (> 2.5 T). A subset of $R_{ax} = 3.6$ m cases are also heated with ECH. Measurements for all cases are available on the LHD data repository [82].

Table E.1: List of discharges used in ch. 5 including shot number, R_{ax}, B_t, FICXS sightline port, time stamp, line-averaged electron density, and central electron temperature.

shot	R_{ax} [m]	B_t[T]	LOS	time [ms]	$\bar{n}_e$ [e19 m^{-3}]	T_{e0} [keV]
146702	3.6	2.75	6	3880	1.558	1.615
				4080	1.656	1.554
				5880	2.154	1.878
				6080	2.149	1.928
146703	3.6	2.75	6	3880	1.362	1.622
				4080	1.445	1.522
163458	3.6	2.75	6	4460	0.376	2.134
				4660	0.390	2.095
				4860	0.410	2.145

Table E.1: List of discharges used in ch. 5 including shot number, R_{ax}, B_t, FICXS sightline port, time stamp, line-averaged electron density, and central electron temperature.

shot	R_{ax} [m]	B_t[T]	LOS	time [ms]	$\bar{n}_e$ [e19 m^{-3}]	T_{e0} [keV]
				5060	0.419	2.257
				6260	0.449	2.278
				6460	0.454	2.280
				6660	0.444	2.208
				6860	0.449	2.275
				7060	0.454	2.307
163459	3.6	2.75	6	4460	0.501	2.012
				4660	0.515	2.035
				4860	0.535	1.995
				5060	0.554	2.014
				6260	0.510	2.276
				6460	0.510	2.433
				6660	0.505	2.413
				6860	0.505	2.320
				7060	0.505	2.221
163460	3.6	2.75	6	6260	0.636	2.285
				6460	0.612	2.279
				6660	0.612	2.400
				6860	0.602	2.343
				7060	0.597	2.238
163461	3.6	2.75	6	4460	0.475	2.292
				4660	0.480	2.242
				4860	0.490	2.262
				5060	0.500	2.382

Table E.1: List of discharges used in ch. 5 including shot number, R_{ax}, B_t, FICXS sightline port, time stamp, line-averaged electron density, and central electron temperature.

shot	R_{ax} [m]	B_t[T]	LOS	time [ms]	$\bar{n}_e$ [e19 m^{-3}]	T_{e0} [keV]
				6260	0.670	2.035
				6660	0.719	2.061
				6860	0.729	2.114
				7060	0.739	2.057
163468	3.6	2.75	6	6260	0.487	2.325
				6460	0.492	2.348
				6660	0.502	2.330
				6860	0.502	2.376
				7060	0.502	2.362
163474	3.6	2.75	6	6860	0.614	2.155
				7060	0.653	2.258
163483	3.6	2.75	7	4480	0.232	1.761
				4690	0.232	1.870
				4890	0.232	1.785
				5090	0.242	1.735
163491	3.6	2.75	7	4480	1.142	1.671
				4680	1.157	1.597
				4890	1.172	1.579
				5090	1.167	1.755
172332	3.6	2.75	7	4500	1.899	1.797
				4700	1.953	1.681
				4900	1.977	1.595
			6	4620	1.953	1.560
				5020	1.982	1.346

Table E.1: List of discharges used in ch. 5 including shot number, R_{ax}, B_t, FICXS sightline port, time stamp, line-averaged electron density, and central electron temperature.

shot	R_{ax} [m]	B_t[T]	LOS	time [ms]	$\bar{n}_e$ [e19 m^{-3}]	T_{e0} [keV]
172339	3.6	2.75	7	4100	1.046	2.069
				4300	1.100	3.276
				4500	1.129	2.043
			6	4220	1.066	1.925
				4620	1.134	2.050
172342	3.6	2.75	7	4300	0.320	4.003
				4500	0.335	2.097
				4700	0.345	2.200
				4900	0.355	2.260
			6	4220	0.311	2.084
				4420	0.311	2.131
				4620	0.325	2.208
				4820	0.345	2.119
				5020	0.359	1.882
183677	3.55	2.7887	7	4450	0.445	2.292
				4650	0.450	2.698
				4850	0.455	2.760
				5050	0.461	2.417
			6	4500	0.445	2.603
				4700	0.450	2.485
				4900	0.461	2.504
				5100	0.466	2.280
				5300	0.477	2.431
183678	3.55	2.7887	7	4250	0.496	2.513

Table E.1: List of discharges used in ch. 5 including shot number, R_{ax}, B_t, FICXS sightline port, time stamp, line-averaged electron density, and central electron temperature.

shot	R_{ax} [m]	B_t[T]	LOS	time [ms]	$\bar{n}_e$ [e19 m^{-3}]	T_{e0} [keV]
				4450	0.496	2.545
				4650	0.501	2.563
			6	4300	0.496	2.437
				4500	0.496	2.535
				4700	0.512	2.317
				4900	0.523	2.491
183679	3.55	2.7887	6	6500	0.807	2.378
				6700	0.845	2.323
				6900	0.855	2.433
				7100	0.866	2.325
				7300	0.861	2.400
183684	3.55	2.7887	7	4450	1.060	2.020
				4650	1.093	2.043
			6	4500	1.071	2.061
				4700	1.098	2.064
				4900	1.103	2.098
183685	3.55	2.7887	7	4450	1.069	1.957
				4650	1.080	1.984
				4850	1.101	1.995
				5050	1.107	1.969
			6	4300	1.015	1.909
				4500	1.091	1.952
				4700	1.091	2.011
				4900	1.107	1.980

Table E.1: List of discharges used in ch. 5 including shot number, R_{ax}, B_t, FICXS sightline port, time stamp, line-averaged electron density, and central electron temperature.

shot	R_{ax} [m]	B_t[T]	LOS	time [ms]	$\bar{n}_e$ [e19 m^{-3}]	T_{e0} [keV]
				5100	1.112	2.042
183688	3.55	2.7887	7	4450	0.833	2.161
				4650	0.833	2.119
				4850	0.849	2.146
				5050	0.855	2.138
			6	4500	0.833	2.124
				4700	0.833	2.149
				4900	0.855	2.122
				5100	0.860	2.189
				5300	0.866	2.065
183689	3.55	2.7887	7	4450	0.845	2.016
				4650	0.839	1.989
				4850	0.839	2.111
				5050	0.861	2.030
			6	4500	0.845	2.050
				4700	0.839	2.042
				4900	0.855	2.023
				5100	0.866	2.034
				5300	0.871	2.128
183690	3.55	2.7887	7	4450	0.758	2.143
				4650	0.774	2.144
				4850	0.795	2.269
				5050	0.812	2.186
			6	4500	0.768	2.053

Table E.1: List of discharges used in ch. 5 including shot number, R_{ax}, B_t, FICXS sightline port, time stamp, line-averaged electron density, and central electron temperature.

shot	R_{ax} [m]	B_t[T]	LOS	time [ms]	$\bar{n}_e$ [e19 m^{-3}]	T_{e0} [keV]
				4900	0.795	2.283
				5300	0.838	2.229
183691	3.55	2.7887	7	4450	0.780	2.145
				4650	0.785	2.100
				4850	0.807	2.149
				5050	0.828	2.192
			6	4500	0.780	2.037
				4900	0.807	2.113
				5300	0.839	2.154
183692	3.55	2.7887	7	4450	0.690	2.177
				4650	0.695	2.140
				4850	0.706	2.220
				5050	0.722	2.213
			6	4500	0.685	2.194
				4700	0.701	2.149
				4900	0.717	2.251
				5100	0.728	2.179
				5300	0.738	2.222
183693	3.55	2.7887	7	4450	0.718	2.120
				4650	0.729	2.139
				4850	0.750	2.159
				5050	0.772	2.174
			6	4500	0.729	2.103
				4700	0.740	2.130

Table E.1: List of discharges used in ch. 5 including shot number, R_{ax}, B_t, FICXS sightline port, time stamp, line-averaged electron density, and central electron temperature.

shot	R_{ax} [m]	B_t[T]	LOS	time [ms]	$\bar{n}_e$ [e19 m^{-3}]	T_{e0} [keV]
				4900	0.750	1.976
				5100	0.767	2.117
				5300	0.788	2.143
183694	3.55	2.7887	6	6500	0.973	2.227
				6700	0.967	2.249
				6900	0.973	2.303
				7100	0.973	2.241
				7300	0.978	2.251
183695	3.55	2.7887	7	8650	0.805	1.990
				8850	0.794	2.034
				9050	0.762	2.012
			6	6500	0.826	2.377
				6700	0.810	2.325
				6900	0.805	2.295
				7100	0.794	2.429
				7300	0.794	2.357
183696	3.55	2.7887	7	4450	0.740	2.198
				4650	0.767	2.226
				4850	0.783	2.254
				5050	0.805	2.257
			6	4500	0.756	2.169
				4700	0.772	2.136
				4900	0.789	2.130
				5100	0.816	2.192

Table E.1: List of discharges used in ch. 5 including shot number, R_{ax}, B_t, FICXS sightline port, time stamp, line-averaged electron density, and central electron temperature.

shot	R_{ax} [m]	B_t[T]	LOS	time [ms]	$\bar{n}_e$ [e19 m^{-3}]	T_{e0} [keV]
				5300	0.826	2.160
183698	3.7	2.6757	7	4250	1.366	1.362
				4450	1.082	1.516
				4720	1.382	1.701
				4850	1.398	1.739
			6	4300	1.287	1.372
				4500	1.130	1.614
				4700	1.351	1.742
				4900	1.445	1.697
				5100	1.456	1.683
183699	3.7	2.6757	7	4450	1.331	1.819
				4650	1.442	1.754
				4850	1.458	1.760
				5050	1.447	1.752
			6	4500	1.395	1.756
				4700	1.463	1.709
				4900	1.463	1.710
				5100	1.474	1.843
				5300	1.468	1.816
183700	3.7	2.6757	7	4450	1.240	1.674
				4650	1.372	1.715
				4850	1.435	1.710
				5050	1.451	1.731
			6	4500	1.298	1.730

Table E.1: List of discharges used in ch. 5 including shot number, R_{ax}, B_t, FICXS sightline port, time stamp, line-averaged electron density, and central electron temperature.

shot	R_{ax} [m]	B_t[T]	LOS	time [ms]	$\bar{n}_e$ [e19 m^{-3}]	T_{e0} [keV]
				4700	1.419	1.707
				4900	1.445	1.692
				5100	1.456	1.640
				5300	1.466	1.677
183701	3.7	2.6757	7	4320	1.244	1.728
				4450	1.338	1.804
				4650	1.417	1.688
				4850	1.444	1.705
			6	4300	1.201	1.759
				4500	1.386	1.730
				4700	1.428	1.768
				4900	1.454	1.708
				5100	1.475	1.792
183704	3.7	2.6757	7	4450	1.176	1.744
				4650	1.213	1.767
				4850	1.218	1.774
				5050	1.218	1.756
			6	4500	1.197	1.688
				4700	1.228	1.722
				4900	1.223	1.685
				5100	1.223	1.758
				5300	1.228	1.725
183705	3.7	2.6757	7	4250	1.159	1.680
				4450	1.191	1.745

Table E.1: List of discharges used in ch. 5 including shot number, R_{ax}, B_t, FICXS sightline port, time stamp, line-averaged electron density, and central electron temperature.

shot	R_{ax} [m]	B_t[T]	LOS	time [ms]	$\bar{n}_e$ [e19 m^{-3}]	T_{e0} [keV]
				4650	1.201	1.842
				4850	1.222	1.723
			6	4300	1.185	1.697
				4500	1.201	1.729
				4700	1.212	1.742
				4900	1.228	1.783
				5100	1.212	1.792
183706	3.7	2.6757	7	4250	1.179	1.606
				4450	1.210	1.641
				4650	1.210	1.721
				4850	1.221	1.766
			6	4500	1.221	1.575
				4700	1.221	1.621
				4900	1.226	1.844
				5100	1.231	1.682
183707	3.7	2.6757	7	4250	1.192	1.740
				4450	1.219	1.685
				4650	1.235	1.763
				4850	1.224	1.792
			6	4500	1.229	1.660
				4700	1.240	1.704
				4900	1.235	1.787
				5100	1.240	1.776
183709	3.7	2.6757	7	4450	1.001	1.832

Table E.1: List of discharges used in ch. 5 including shot number, R_{ax}, B_t, FICXS sightline port, time stamp, line-averaged electron density, and central electron temperature.

shot	R_{ax} [m]	B_t[T]	LOS	time [ms]	$\bar{n}_e$ [e19 m^{-3}]	T_{e0} [keV]
				4650	1.154	1.929
				4850	1.201	1.799
				5050	1.227	1.722
183712	3.7	2.6757	7	4450	0.985	1.669
				4650	0.996	1.740
				4850	0.990	1.722
				5050	1.001	1.783
			6	4500	1.001	1.691
				4700	1.006	1.737
				4900	1.001	1.778
				5100	1.006	1.757
				5300	1.012	1.759
183714	3.7	2.6757	7	4450	0.976	1.696
				4650	1.002	1.692
				4850	1.002	1.738
				5050	1.007	1.784
			6	4500	0.991	1.732
				4700	1.007	1.727
				4900	1.012	1.706
				5100	1.012	1.777
				5300	1.012	1.763
183715	3.7	2.6757	7	4450	0.618	1.820
				4650	0.665	1.770
				4850	0.786	1.859

Table E.1: List of discharges used in ch. 5 including shot number, R_{ax}, B_t, FICXS sightline port, time stamp, line-averaged electron density, and central electron temperature.

shot	R_{ax} [m]	B_t[T]	LOS	time [ms]	$\bar{n}_e$ [e19 m^{-3}]	T_{e0} [keV]
				5050	0.776	1.815
			6	4500	0.618	1.857
				4700	0.744	1.805
				4900	0.797	1.795
				5100	0.765	1.870
				5300	0.760	1.877
183716	3.7	2.6757	7	4450	0.600	1.764
				4650	0.600	1.882
				4850	0.757	1.712
				5050	0.763	1.714
			6	4500	0.605	1.749
				4700	0.626	1.722
				4900	0.773	1.785
				5100	0.752	1.821
				5300	0.752	1.795
183717	3.7	2.6757	7	4450	0.728	1.747
				4650	0.760	1.800
				4850	0.770	1.848
				5050	0.770	1.814
			6	4500	0.749	1.773
				4700	0.754	1.765
				4900	0.770	1.853
				5100	0.786	1.826
				5300	0.781	1.921